BIELEFELD UNIVERSITY

FACULTY OF PHYSICS

DISSERTATION

Higher order cumulants of net conserved charge distributions in lattice QCD

Dennis Bollweg

Supervisor and first referee:
Prof. Dr. Frithjof Karsch
Second referee:
PD. Dr. Christian Schmidt-Sonntag

October 13, 2021

Contents

Chapter 1

Introduction

For centuries, philosophers and scientists alike have been trying to identify the fundamental, indivisible constituents that make up matter. While the idea that matter consists of such indivisible constituents dates as far back as the ancient Greeks, it took scientists until the nineteenth century to find reliable evidence for the existence of atoms. With the advent of modern physics in the twentieth century, scientists were able to quantitatively study the behavior of atoms and eventually discovered that the atom is yet another compound object, consisting of electrons and a nucleus, the latter of which revealed itself to be a bound state of protons and neutrons.

Ultimately, this search for the fundamental building blocks of nature culminated in the formulation of the standard model of particle physics. It describes three of the four fundamental forces of nature, electromagnetism, the weak interaction, responsible for the β decay, and the strong interaction, responsible for e.g. nuclear forces, together in the framework of quantum field theory. Gravity, the weakest force in nature, still refuses to be formulated in terms of a consistent quantum field theory and is not part of the standard model.

The fundamental constituents of the standard model, the elementary particles, are listed in Table 1.1 below. The fermionic sector can be divided into two segments, strongly interacting quarks (up, down, strange, charm, top and bottom) and leptons (electrons, muons, taus and their respective neutrinos) that only interact electroweakly. In the bosonic sector, the photon γ mediates electromagnetic forces, while the gluons g mediate strong forces and the $W^{\pm}$ and Z bosons weak forces. Finally, interactions with the scalar Higgs boson H^0 provide the fermions and massive bosons with their mass terms. Although it faces an ever growing list of short comings, the standard model is one of the best tested theories ever put forth by scientists and its predictions have been confirmed to incredible precision.

The strongly interacting sector of the standard model is described by the theory of quantum chromodynamics (QCD) which exhibits many unique features

Fermions			Bosons
u	c	t	g
d	s	b	γ
e	μ	τ	H
ν_e	ν_μ	ν_τ	$W^\pm, Z$

Table 1.1: Particle content of the standard model.

absent in the electroweak sector. QCD is a non-abelian gauge theory with $SU(3)$ as the symmetry group. Quarks are described as spin $\frac{1}{2}$ fermions in the fundamental representation of $SU(3)$. As such, they come in three so-called color charges corresponding to the three generators of the fundamental representation. Gluons on the other hand are described as massless spin 1 bosons in the adjoint representation of $SU(3)$ and thus come in eight different color charge variants. Color charges, however, do not exist freely in nature and are instead only encountered inside color charge neutral objects such as hadrons. This is a result of QCDs *confinement* property: The static quark-antiquark potential is found to rise linearly for large separation distances r [1]. Furthermore, QCD is *asymptotically free*: The coupling strength g_s decreases with increasing energy scale which enables perturbative calculations for highly energetic processes [2]. Conversely, however, a large part of QCDs phenomena cannot be addressed with perturbative methods, rendering the study of them incredibly challenging.

1.1 The phase diagram of QCD

Due to these unique features, strong interaction matter shows a variety of interesting properties when subjected to extreme conditions of temperature and density such as those present in the early universe or in heavy ion collision experiments. When heated up sufficiently, QCD matter transitions into a new state, the Quark Gluon Plasma (QGP) phase, where quarks and gluons are deconfined and can move quasi-freely within the plasma rather than being confined into hadrons. This new state of strong interaction matter is studied intensively in heavy ion collision experiments. Measurements at the Relativistic Heavy Ion Collider (RHIC) at Brookhaven National Laboratory and the Large Hadron Collider (LHC) at CERN revealed that the medium created in these heavy ion collisions is able to quench highly energetic particle jets with an efficiency that can only be attributed to a plasma of quarks and gluons [3][4]. Furthermore, the medium shows large elliptic flow and a shear viscosity to entropy density ratio η/s very close to that of a perfect fluid.

While the existence of the QGP phase has been firmly established [5], a precise determination of the phase diagram of QCD has not been possible so far as a multitude of challenges complicate its study. The two principle features of QCD that dictate the structure of the phase diagram are the above mentioned confinement as well as chiral symmetry. In the limit of infinitely heavy quark masses, QCD is reduced to a pure $SU(3)$ gauge theory with its dynamics entirely governed by gluons. The corresponding Lagrangian possesses an exact $Z(3)$ center symmetry that is spontaneously broken above a critical temperature T_c. This is signaled by the behavior of the so-called Polyakov loop expectation value $|\langle P\rangle|$, which is non-zero in the symmetry broken phase and vanishes in the $Z(3)$ symmetric phase [6]. It therefore functions as the order parameter for this phase transition. The Polyakov loop is furthermore related to the heavy quark free energy F_q via

$$|\,\langle P\rangle\,| \sim e^{-F_q/T}. \tag{1.1.1}$$

Therefore, $|\langle P\rangle| = 0$ signals confinement, as the free energy associated with having a free heavy quark in the system diverges. $|\langle P\rangle| \neq 0$, on the other hand, implies deconfinement. The transition between the two phases has been found to be of first order. Moving away from the purely gluonic case, however, the $Z(3)$ center symmetry is explicitly broken and the Polyakov loop no longer functions as an order parameter which complicates the study of confinement in full QCD significantly.

In the opposite quark mass limit, where the masses (m_f) of N_f quarks vanish, the QCD Lagrangian possesses a $U(N_f)_L \times U(N_f)_R$ chiral symmetry which can equivalently be expressed as $SU(N_f)_L \times SU(N_f)_R \times U(1)_A \times U(1)_V$. The axial symmetry $U(1)_A$, although a symmetry of the Lagrangian, is broken in the quantized theory. The $U(1)_V$ symmetrry is responsible for baryon number conservation whereas the chiral symmetry $SU(N_F)_L \times SU(N_F)_R$ is broken spontaneously below a critical temperature T_c^0. This is signaled by a non-zero chiral condensate

$$\langle \bar{\psi}_f \psi_f \rangle = \frac{T}{V} \frac{\partial \ln Z}{\partial m_f}, \tag{1.1.2}$$

which is the order parameter of this phase transition. Furthermore, this spontaneous symmetry breaking gives rise to massless Goldstone bosons. While non-zero quark masses explicitly break chiral symmetry, it can still be considered a good approximate symmetry for the light up and down quarks and serves as an explanation for the smaller then otherwise expected pion masses found in nature. The nature of the chiral phase transition is still under investigation and recent studies are aiming to determine the universality class that the transition belongs to [7]. The current estimate for the critical temperature of QCD with two massless light quarks and a massive strange quark calculated by the HotQCD collaboration is $T_c^0 = 132^{+3}_{-6}$ MeV [8].

Lattice QCD calculations have been able to show that an imprint of the chiral phase transition is still visible at finite quark masses. The chiral condensate changes considerably with increasing temperature and its associated susceptibility shows a clear peak that diverges as two light quark masses (m_l) approach zero, i.e. $m_l \to 0$. It is therefore referred to as an analytic crossover transition rather then a true phase transition and the peak of the corresponding susceptibility is often used to define a pseudo-critical transition temperature T_{pc}. Recent lattice QCD calculations from the HotQCD collaboration yielded $T_{pc} = 156.5 \pm 1.5$ MeV [9] while Borsanyi et al. found $T_{pc} = 158 \pm 0.6$ MeV [10].

The phase diagram can be extended by a further axis, the baryon chemical potential μ_B, which controls the net-baryon density of the system. Unfortunately, direct lattice QCD simulations at non-zero chemical potential are rendered impossible by the infamous sign problem. The lattice QCD action becomes complex and can no longer be used as a weight factor in Monte Carlo simulation algorithms. While promising methods to solve this problem are being developed [11][12][13], none of them is in a state where it can provide precise, continuum extrapolated predictions. Thus indirect methods have to be used instead. By using extrapolations from imaginary chemical potentials [14], where simulations are possible, or by using Taylor expansions around $\mu_B = 0$ [15], the $\mu_B > 0$ region can be accessed and the pseudo-critical transition line $T_{pc}(\mu_B)$ has been calculated up to about $\mu_B = 300$ MeV in recent studies. It was found that the pseudo-critical transition temperature slightly decreases with increasing baryon chemical potential but within the region explored so far, the crossover nature did not change. Beyond $\mu_B \sim 300$ MeV, first principle lattice QCD calculations are no longer available and model calculations are used to explore the QCD phase diagram. These predict that the crossover line delineated by $T_{pc}(\mu_B)$ ends in a second order critical endpoint (CEP) beyond which the transition turns into a genuine first order phase transition. However, predictions for the specific location vary strongly depending on the model used. A sketch of a possible QCD phase diagram is shown in Fig. 1.1.

1.2 The search for the critical endpoint

Searching for the elusive critical endpoint in the QCD phase diagram has become one of the mayor goals in heavy ion research with both theorists and experimentalists devoting significant resources towards finding it. Apart from the chiral condensate and its susceptibility, conserved charge[1] fluctuations also show critical behavior if they couple to the order parameter. Furthermore, they are accessible

[1] Such as baryon number (B), electric charge (Q) or strangeness (S).

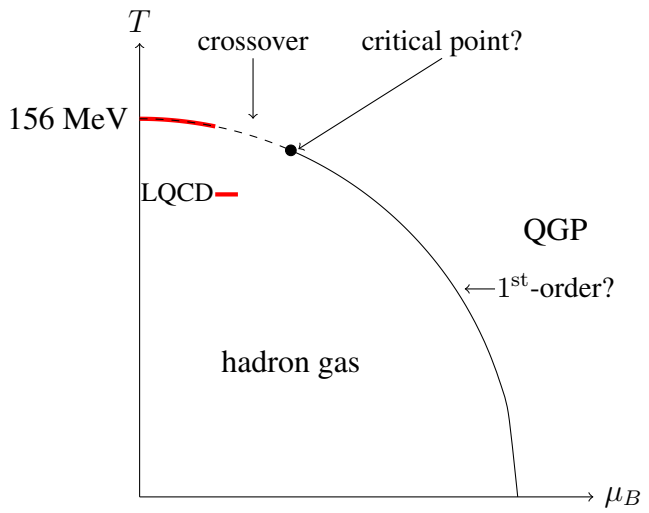

Figure 1.1: A sketch of a possible QCD phase diagram as a function of temperature T and baryon chemical potential μ_B. The red line denotes the small strip of the pseudo-critical transition line $T_{\rm pc}(\mu_B)$ that we are able to address with lattice QCD calculations. The black dashed line corresponds to the pseudo-critical transition line $T_{\rm pc}(\mu_B)$ which ends in a critical endpoint denoted by the black dot. The solid black line denotes a possible first order transition line. The nuclear liquid-gas transition and a possible color superconducting phase are not shown.

in heavy ion collision experiments such that a comparison between theoretical predictions and measurements are in principle possible. When relativistic nuclei collide in such experiments, they create a hot and dense "fireball" of strongly interacting matter that rapidly expands and cools down, traversing different regions of the QCD phase diagram [16]. After the early stages of the collision, the fireball thermalizes quickly and finds itself in the QGP phase. As it cools, quarks and gluons eventually confine into hadrons, either smoothly via the crossover transition, or possibly abruptly via a first order transition depending on the baryon chemical potential of the system. Soon after, the fireballs expansion and cooling causes inelastic scattering to cease and the particle content to become fixed. This is known as the chemical freeze-out and is characterized by the freeze-out temperature T_f and chemical potentials $\mu_{B,f}, \mu_{Q,f}, \mu_{S,f}$. Finally, elastic scatterings also stop as the so-called kinetic freeze-out is reached. From here on, particle momenta are fixed and particles "stream" freely until they reach the detector.

Due to global charge conservation, the system created in a heavy ion collision experiment should be described by a canonical ensemble, whereas theoretical calculations that study the QCD phase diagram use a grand canonical formulation. To emulate such a grand canonical ensemble in the experiments, measurements

are performed in sub-volumes of the fireball which is realized by introducing appropriate rapidity cuts. Charge fluctuations are then measured by counting the particle multiplicities in this sub-volume in each collision event which then yields an event-by-event charge distribution.

Since the particle multiplicities are fixed at chemical freeze-out, one expects to see remnants of the critical behavior in event-by-event fluctuations if freeze-out occurs close enough to the critical endpoint. As the critical point is approached, the correlation length ξ increases until it eventually diverges at the CEP. Seminal work by Stephanov based on universality arguments has shown that higher order fluctuations such as the kurtosis are particularly sensitive to this divergence [17]. For instance, the kurtosis scales with ξ^7 in the vicinity of the CEP and is expected to turn slightly negative when the freeze-out curve passes below the CEP [18]. The freeze-out conditions found in heavy ion collisions can be controlled

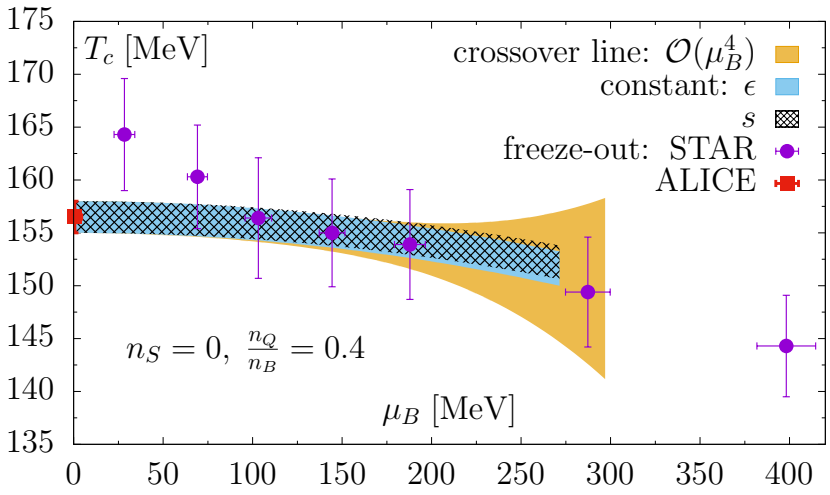

Figure 1.2: A comparison between the pseudo-critical transition line $T_{pc}(\mu_B)$ and freeze-out parameters determined from fitting particle yield measurements to statistical hadronization models. Taken from [9].

by varying the energy $\sqrt{s}_{NN}$ of the colliding nuclei. High beam energies, such as those realized in the ALICE experiment at LHC, correspond to small freeze-out chemical potentials while lower beam energies result in higher freeze-out chemical potentials. The Beam Energy Scan (BES) program performed at RHIC studies collisions with energies $\sqrt{s}_{NN}$ ranging from 200 GeV down to 7.7 GeV and the freeze-out curve that results from these different beam energies seems to be in close agreement with the pseudo-critical transition line of the chiral crossover as shown in Fig. 1.2. Therefore, higher order cumulants of conserved charge fluctu-

ations are promising observables for finding evidence for the critical endpoint in the QCD phase diagram.

1.3 Aim of this thesis

In this thesis, we want to provide first principle QCD predictions of cumulants of net charge fluctuations using lattice QCD methods and confront them, to the extent that it is possible, with available experimental results as well as models such as the hadron resonance gas. In the first half of this thesis, comprised of the first four sections, we will lay out the theoretical basis for these calculations. Section 2 will detail the formulation of QCD on a discretized lattice and explain the specifics of the Highly Improved Staggered Quark (HISQ) action that we use for the numerical simulations presented in this work. The third section summarizes the numerical methods and algorithms used and provides details on the employed simulation parameters as well as the scale setting procedure. The Taylor expansion method that is used to access susceptibilities in the small baryon density region is described in the fourth section. The second half of this thesis then presents a detailed discussion of the results obtained from numerical computations performed throughout the last three years. We will start with comparing precise lattice QCD determinations of second order cumulants to different hadron resonance gas models in the fifth section. This is followed by a comparison of up to sixth order cumulant ratios of net baryon number fluctuations along the pseudo-critical transition line $T_{pc}(\mu_B)$ to corresponding measurements taken by the STAR collaboration during the BES program. Lastly, we present results on higher order cumulant ratios of net electric charge and net strangeness fluctuations along $T_{pc}(\mu_B)$ and discuss to what extent they can be helpful in constraining freeze-out parameters in a model independent approach.

Chapter 2

Formulating QCD on the lattice

Obtaining QCD predictions from first principle calculations poses a formidable challenge as the theory is inherently strongly coupled such that the usual perturbative methods employed in particle physics are only applicable at very small distances or, equivalently, at very high energies. In order to obtain predictions at intermediate and smaller energy scales, non-perturbative methods such as lattice QCD need to be applied. The fundamental idea behind the lattice approach is to formulate the theory on a discrete space-time grid in order to render the QCD path integral finite dimensional, making it amenable to numerical treatments on powerful computers. Solving the discretized theory at different resolutions, quantified by the lattice space a, then allows to compute the limit $a \to 0$ in which the continuum theory is recovered. As the discretization procedure itself is not unique, many different variants have been proposed throughout the years, each coming with its own set of advantages and short-comings that lattice QCD practitioners get to choose from. In this section, we will describe our particular choice of discretization schemes.

2.1 Lattice discretization

The fundamental mathematical object from which physical observables are derived in finite temperature QCD is the partition function

$$Z(V,T,\mu) = \int \mathcal{D}A\mathcal{D}\psi\mathcal{D}\bar{\psi}\exp\left\{-S_E\right\}, \tag{2.1.1}$$

which integrates gauge- and fermion field configurations weighted by a Boltzmann factor $\exp\left\{-S_E\right\}$ given by the Euclidean QCD action S_E. Here, A represents the gluon field and ψ and $\bar{\psi}$ the Grassmann-valued quark fields. The temperature and volume dependencies enter the partition function through the integration

limits of the Euclidean action while the chemical potential μ is introduced through the conserved current $\bar{\psi}\gamma_0\psi$

$$\begin{aligned} S_E &= \int_0^{\frac{1}{T}} \mathrm{d}x_0 \int_V \mathrm{d}^3x \mathcal{L}_E(A, \psi, \bar{\psi}, \mu) \\ &= \int_0^{\frac{1}{T}} \mathrm{d}x_0 \int_V \mathrm{d}^3x \left[-\frac{1}{2}\mathrm{Tr} F_{\mu\nu}F_{\mu\nu} + \bar{\psi}_{f,a} \left(\gamma_\nu \left(\partial_\nu - igA_\nu - \mu\delta_{0,\nu}\right) + m_f\right)_{a,b} \psi_{f,b} \right]. \end{aligned} \tag{2.1.2}$$

Color-space is indexed through a and b ranging from 0 to N_c with N_c being the number of colors and flavor-space is indexed via $f = 0, \ldots, n_f$ where n_f is the number of quark-flavors. Greek indices label (Euclidean) space-time directions and Einsteins summation convention for equal indices is used. The field strength tensor $F_{\mu\nu}$ is defined as

$$F_{\mu\nu}(x) = \sum_{i=0}^{N_c^2-1} \frac{\lambda_i}{2} F^i_{\mu\nu}(x), \tag{2.1.3}$$

$$F^i_{\mu\nu}(x) = \partial_\mu A^i_\nu(x) - \partial_\nu A^i_\mu(x) + g f^{ijk} A^j_\mu(x) A^k_\nu(x), \tag{2.1.4}$$

with f^{ijk} being the structure constants of $SU(N_c)$ and λ_i the Gell-Mann matrices. Similarly, the gauge field $A_\mu(x)$ is defined via

$$A_\mu(x) = \sum_{i=0}^{N_c^2-1} \frac{\lambda_i}{2} A^i_\mu(x). \tag{2.1.5}$$

The discretization of (2.1.1) proceeds by introducing a finite space-time grid with N_τ lattice sites in temporal direction and N_σ lattice sites in spatial directions. Neighboring sites are separated by a lattice spacing a such that the physical 3-volume V is given by $V = a^3 N_\sigma^3$ and the temperature T is related to the inverse of the temporal lattice extent $T = \frac{1}{aN_\tau}$. The quark fields $\psi(x)$ are placed on lattice sites, while gluonic degrees of freedom are introduced via matrices $U_\mu(x) \in \mathrm{SU}(N_c)$ placed on the links connecting two lattices sites. These link matrices are related to the gluon fields via $U_\mu(x) = \exp\{aA_\mu(x)\}$. Multiplying the link matrices $U_\mu(x)$ along a unit square yields the fundamental plaquette

$$U_{\mu\nu}(x) = U_\mu(x) U_\nu(x + \hat{\mu}) U^\dagger_\mu(x + \hat{\nu}) U^\dagger_\nu(x), \tag{2.1.6}$$

which is used to formulate a discrete version of the gluon action, the Wilson action

$$S_{G,\mathrm{Wilson}} = \frac{2N_c}{g^2} \sum_x \sum_{\mu<\nu} \left(1 - \frac{1}{N_c} \mathrm{Re\ Tr}\ U_{\mu\nu}(x)\right). \tag{2.1.7}$$

Using the relation between the link matrices $U_\mu(x)$ and $A_\mu(x)$, it is easy to show that this discretization reproduces the continuum formulation, i.e. the field strength tensor term, up to $\mathcal{O}(a^2)$ corrections. The convergence rate towards the continuum can be improved upon by employing what is known as Symmanzik improvement [19][20] where further terms are included in the action that explicitly cancel the $\mathcal{O}(a^2)$ corrections. The tree-level Symmanzik improvement, for example, achieves this cancellation by including link-matrices $U_\mu(x)$ multiplied along 2×1 rectangles

$$\begin{aligned} S_G = \frac{2N_c}{g^2}\sum_x\sum_{\mu<\nu} c_P\left(1-\frac{1}{N_c}\text{Re Tr } U_{\mu\nu}(x)\right) \\ + c_R\left(1-\frac{1}{N_c}\text{Re Tr } R_{\mu\nu}(x)\right), \\ \text{with } R_{\mu\nu}(x) = U_\mu(x)U_\nu(x+\hat{\mu})U_\nu(x+\hat{\mu}+\hat{\nu})U_\mu^\dagger(x+2\hat{\nu})U_\nu^\dagger(x+\hat{\nu})U_\nu^\dagger(x) \\ + U_\mu(x)U_\mu(x+\hat{\mu})U_\nu(x+2\hat{\mu})U_\mu^\dagger(x+\hat{\nu}+\hat{\mu})U_\mu^\dagger(x+\hat{\nu})U_\nu^\dagger(x). \end{aligned} \tag{2.1.8}$$

Choosing the coefficients $c_P = \frac{5}{4}$ and $c_R = -\frac{1}{6}$ then cancels the $\mathcal{O}(a^2)$ corrections. All numerical simulations carried out in this thesis make use of this improved gauge action. Schematic representations of the expressions contained in the Symmanzik improved gauge action are shown in Figure 2.1.

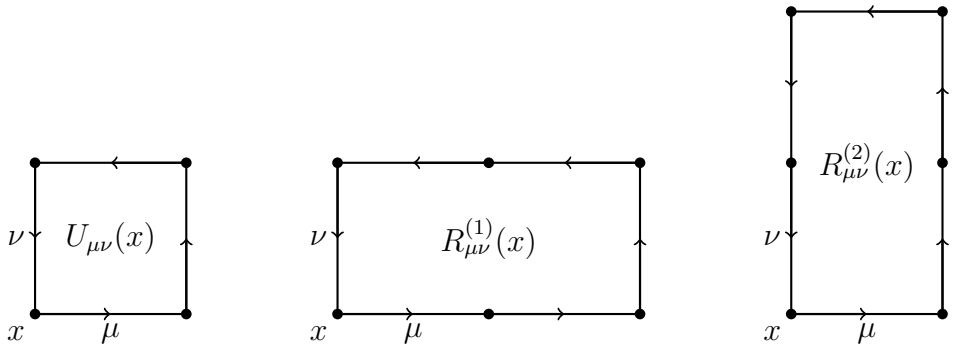

Figure 2.1: Schematic representations of the fundamental plaquette $U_{\mu\nu}(x)$ and the two terms comprising $R_{\mu\nu}(x)$. Link variables $U_\mu(x)$ are represented by an arrow going from x to $x+\hat{\mu}$.

2.2 Highly improved staggered quarks

The fermionic part of the action can be discretized by replacing the covariant derivative in (2.1.2) with symmetric finite differences. Local gauge invariance is

retained by multiplying the neighboring spinors $\psi(x \pm \hat{\mu})$ with the lattice gauge fields $U_\mu(x)$ as shown for a single quark flavor below

$$S_{F,\text{naive}} = \sum_x \bar{\psi}(x) \left(\sum_\mu \gamma_\mu \frac{U_\mu(x)\psi(x+\hat{\mu}) - U_\mu^\dagger(x-\hat{\mu})\psi(x-\hat{\mu})}{2a} + m\psi(x) \right). \tag{2.2.1}$$

This discretization approach, known as the naive fermion discretization, comes with a significant drawback that necessitates further improvements. The quark propagator, obtained by inverting the Dirac operator, contains 16 poles, 15 of which represent unphysical states known as *doublers*. In the massless and non-interacting case, the poles are located at $p = (0,0,0,0)$ and $p_{\text{doubler}} = (\pi/a,0,0,0)$, $(0,\pi/a,0,0), \ldots, (\pi/a,\pi/a,\pi/a,\pi/a)$ [21]. More refined discretization schemes are necessary to reduce or alleviate this doubling problem. One such approach, the staggered quark formulation [22], reduces the degeneracy from 16 down to 4. This is achieved by transforming the spinors locally via

$$\begin{aligned} \psi(x) &\to \gamma_1^{x_1}\gamma_2^{x_2}\gamma_3^{x_3}\gamma_0^{x_0}\psi(x) \\ \bar{\psi}(x) &\to \bar{\psi}(x)\gamma_0^{x_0}\gamma_3^{x_3}\gamma_2^{x_2}\gamma_1^{x_1}, \end{aligned} \tag{2.2.2}$$

which diagonalizes the action w.r.t Dirac space, but introduces the so-called staggered phase factor

$$\eta_1(x) = 1, \eta_2(x) = (-1)^{x_1}, \eta_3(x) = (-1)^{x_1+x_2}, \eta_0(x) = (-1)^{x_1+x_2+x_3}, \tag{2.2.3}$$

into the finite difference term of the action. Of the four identical Dirac components in the action, three are dropped and only one labeled $\chi(x)$ is kept, which yields the staggered quark discretization

$$\begin{aligned} S_{F,\text{staggered}} &= \sum_x \bar{\chi}(x) \left(\sum_\mu \eta_\mu \left(U_\mu(x)\chi(x+\hat{\mu}) - U_\mu^\dagger(x-\hat{\mu})\chi(x-\hat{\mu}) \right) \right. \\ &\quad \left. + m\chi(x) \right). \\ &= S_{F,\text{naive}}[U] + \sum_x m\bar{\chi}(x)\chi(x). \end{aligned} \tag{2.2.4}$$

For notational convenience, we also absorbed appropriate factors of a in $\chi(x)$. The remaining four degenerate quark species are referred to as tastes. At finite lattice spacing, these quark species can interact and change their taste, e.g. by exchanging a gluon with one or more momentum components close to π/a. While

those processes are suppressed by a^2, their effects at finite lattice spacing can still be sizable [23]. The Highly Improved Staggered Quark (HISQ) discretization [24], that we make use of in this work, improves upon the standard staggered quark formulation by eliminating the taste exchange interactions at tree level while also removing other discretization errors at order $\mathcal{O}(a^2)$ stemming from the finite difference term. The latter is achieved simply by extending the finite difference term to contain a three-link hopping, the so-called Naik term [25]

$$S_{F,\mathrm{Naik}}[U] = \sum_{x,\mu} \bar{\chi}(x)\eta_\mu \left(U_\mu(x)U_\mu(x+\hat{\mu})U_\mu(x+2\hat{\mu})\chi(x+3\hat{\mu})\right. \\ \left. -U_\mu^\dagger(x-\hat{\mu})U_\mu^\dagger(x-2\hat{\mu})U_\mu^\dagger(x-3\hat{\mu})\chi(x-3\hat{\mu})\right). \tag{2.2.5}$$

Taste exchange interactions are removed by modifying the quark-gluon vertex with a form factor $f_\mu(q)$ that is zero for momenta q with one or more components $q_i = \pi/a$. More specifically

$$f_\mu(q) = \begin{cases} 1, & \text{for } q \to 0 \\ 0, & \text{for } q \to \vec{\xi}\pi/a, \vec{\xi}^2 \neq 0, \xi_\mu = 0, \end{cases} \tag{2.2.6}$$

where $\vec{\xi}$ is a 4-component vector whose elements can be 0 or 1. This form factor is achieved by smearing the gaugefield $U_\mu(x)$, i.e. replacing it by a weighted sum of neighboring links. Gluons with one transverse momentum component $q_i = \pi/a$ are removed by including so-called three-link staples $U^{3-\mathrm{link}}_{\mu,\nu}(x)$ while those with two and three transverse momentum components $q_i = \pi/a$ are removed by including five-link staples $U^{5-\mathrm{link}}_{\mu,\nu,\rho}(x)$ and seven-link staples $U^{7-\mathrm{link}}_{\mu,\nu,\rho,\sigma}(x)$, respectively. A diagrammatic representation of these staples is given in Fig. 2.2. The smeared link $V_\mu(x) = \mathcal{F}^{f_7}U_\mu(x)$ reads

$$\begin{aligned} V_\mu(x) &= \mathcal{F}^{f_7}U_\mu(x) \\ &= \frac{1}{8}U_\mu(x) + \frac{1}{16}\sum_{\nu\neq\mu} U^{3-\mathrm{link}}_{\mu,\nu}(x) + \frac{1}{64}\sum_{\rho\neq\nu\neq\mu} U^{5-\mathrm{link}}_{\mu,\nu,\rho}(x) \\ &+ \frac{1}{384}\sum_{\sigma\neq\rho\neq\nu\neq\mu} U^{7-\mathrm{link}}_{\mu,\nu,\rho,\sigma}(x). \end{aligned} \tag{2.2.7}$$

Note that the summation over the directions perpendicular to μ also include backward directions. Repeated application of the smearing procedure can further reduce the taste-violation effects stemming from one-loop diagrams but re-projection to $U(3)$ or $SU(3)$ is required to avoid enhancing one-loop diagrams with two gluon vertices [23]. For the HISQ discretization, the $V_\mu(x)$ links are re-projected to $U(3)$, which we label $W_\mu(x)$

$$W_\mu(x) = \mathcal{U}_{U(3)}V_\mu(x). \tag{2.2.8}$$

Finally, a second level of smearing is applied, this time including an additional five-link term, the Lepage term, that cancels remaining $\mathcal{O}(a^2)$ errors introduced by the first level of smearing.

$$X_\mu(x) = \mathcal{F}^{f_7 L} W_\mu(x) = \frac{7}{8} W_\mu(x) + \mathcal{F}^{f_7} W_\mu(x) - \frac{1}{8} \sum_{\nu \neq \mu} W^{\text{Lepage}}_{\mu,\nu}(x). \quad (2.2.9)$$

The full HISQ action then reads

$$S_{\text{HISQ}} = \frac{1}{2} S_{F,\text{naive}}[X] - \frac{1}{48} S_{F,\text{Naik}}[W] + \sum_x m \bar{\chi}(x) \chi(x). \quad (2.2.10)$$

Note, however, that the prefactors listed here, particularly the ones for the Naik term, are specific to the number of flavors used throughout this thesis. We use two mass degenerate (up & down) light quarks and heavier strange quarks in our calculations which is often referred to as $N_f = 2 + 1$. Heavier quark flavors, such as charm quarks with masses around 1.275(25) GeV, are neglected in our calculations as they are contribute only very little to the thermodynamic behavior at the temperature scales that we are interested in.

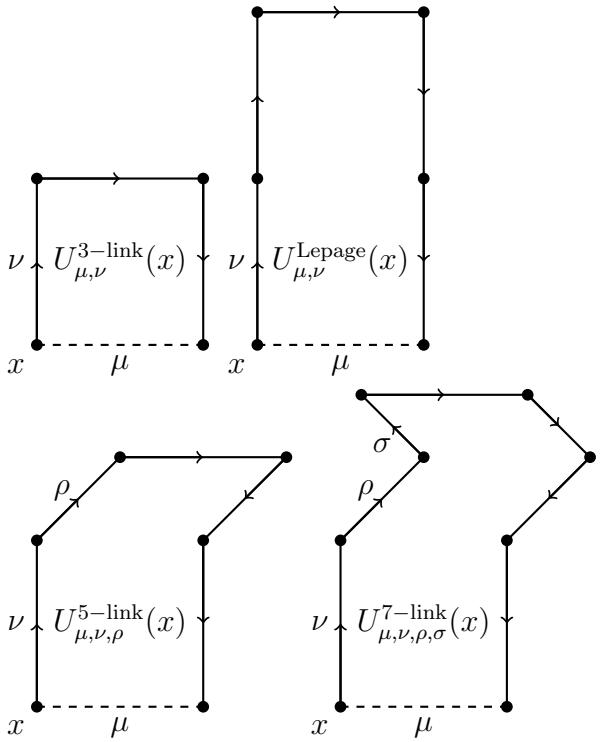

Figure 2.2: Diagrammatic representations of the terms entering the smearing operators $\mathcal{F}^{f_7}$ and $\mathcal{F}^{f_7 L}$.

The formulation that we have presented here so far successfully reduces taste exchange interactions and discretization errors of $\mathcal{O}(a^2)$ but four tastes are still present. In the continuum limit, these would correspond to four physical quark states with the same mass contributing equally to the partition function. In order to correct for this shortcoming, we employ the rooting procedure [23]. The lattice QCD partition function can be written as a (lattice-) path integral analogously to (2.1.1) in which we can integrate out fermionic d.o.f. analytically, giving rise to the determinant of the fermion matrix M_f

$$\begin{aligned} Z_{\text{lat.}} &= \int \mathcal{D}U\mathcal{D}\chi\mathcal{D}\bar{\chi}\; e^{-S_F - S_G} = \int \mathcal{D}U\mathcal{D}\chi\mathcal{D}\bar{\chi}\; e^{-\bar{\chi}M_f\chi - S_G} \\ &= \int \mathcal{D}U\;\; \det M_f e^{-S_G}. \end{aligned} \tag{2.2.11}$$

Each of the four tastes contributes equally to $\det M_f$ in the continuum limit. Using the fourth root of the determinant instead guarantees that we obtain only a single quark state in the continuum. While the procedure of rooting has been discussed controversially in the past, empirical evidence points towards the correctness of it [23]. For the $N_f = 2 + 1$ flavor setup that we are using in this thesis, (2.2.11) reads

$$\begin{aligned} Z &= \int \mathcal{D}U\;\; \det {M_u}^{1/4} \det {M_d}^{1/4} \det {M_s}^{1/4} e^{-S_G} \\ &= \int \mathcal{D}U\;\; \det {M_l}^{1/2} \det {M_s}^{1/4} e^{-S_G}. \end{aligned} \tag{2.2.12}$$

Chapter 3

Numerical Methods

The numerical workflow for calculating higher order cumulants of conserved charge fluctuations presented in this work comprises two main parts, the generation of gaugefield configurations using the rational Hybrid Monte Carlo (RHMC) algorithm and the subsequent evaluation of certain operators defined in section 4.4 on these gaugefield configurations with a combination of Krylov solvers. In this chapter, we will provide a brief overview of these methods and highlight some of the algorithmic details crucial for keeping numerical costs of these simulations under control.

3.1 RHMC algorithm

Expectation values of physical observables derived from (2.2.12) generally take the form

$$\langle \mathcal{O} \rangle = \frac{1}{Z} \int \mathcal{D}U \; \mathcal{O} \det {M_l}^{1/2} \det {M_s}^{1/4} e^{-S_G}, \tag{3.1.1}$$

which lends itself naturally to evaluation with importance sampling Monte Carlo if

$$P(U) = \frac{1}{Z} \det M_l[U]^{1/2} \det M_s[U]^{1/4} e^{-S_G[U]}, \tag{3.1.2}$$

can be interpreted as a probability weight. In the absence of a chemical potential μ, this is possible if the lattice Dirac operator - the finite difference operator in the fermion action - is γ^5 hermitian, which is the case for the staggered discretization that we are using in this thesis. With importance sampling, computing (3.1.1) then comes down to generating a sequence of N gauge configurations U_i, $i = 1, \ldots, N$

distributed according to (3.1.2) and evaluating

$$\langle \mathcal{O} \rangle \simeq \frac{1}{N} \sum_{i=1}^{N} \mathcal{O}(U_i). \tag{3.1.3}$$

The generation of such a sequence of gauge field configurations requires the use of sophisticated numerical methods, particularly due to the determinants of the fermion matrix whose dimension can easily exceed $\dim(M_f) \sim \mathcal{O}(10^6)$. In this thesis, we will make use of the rational hybrid Monte Carlo (RHMC) algorithm [26][27] to generate gauge field configurations. In it, the fermion determinant is dealt with by introducing bosonic pseudo-fermions ϕ and $\phi^\dagger$ that are placed on the lattice sites, just like their fermionic counter parts χ and $\bar{\chi}$. Unlike those, however, $\phi(x)$ and $\phi^\dagger(x)$ are not Grassmann valued but complex valued vectors which have, in the case of the staggered discretization, three color components. A single determinant factor with exponent $n_f/4$ can be re-written in terms of a Gaussian lattice path integral over these pseudo-fermions via

$$(\det M_f)^{n_f/4} = \int \mathcal{D}\phi^\dagger \mathcal{D}\phi \; e^{-\phi^\dagger \left(M_f^\dagger M_f\right)^{-n_f/4} \phi}. \tag{3.1.4}$$

To evaluate the matrix exponential $\left(M_f^\dagger M_f\right)^{-n_f/4}$, a rational approximation $r(x) \simeq x^{-n_f/8}$ is used that takes the form

$$r(M_f^\dagger M_f) = \alpha_0 + \sum_{i=1}^{k} \frac{\alpha_i}{M_f^\dagger M_f + \beta_i}, \tag{3.1.5}$$

where α_i and β_i are constants chosen to optimally approximate $x^{-n_f/8}$ given the maximum degree k. By incorporating this rational approximation and the pseudo-fermions into a new effective action S_{eff}, the lattice path integral can be expressed as

$$\begin{aligned} Z &= \int \mathcal{D}U \mathcal{D}\phi^\dagger \mathcal{D}\phi \; \exp\left\{ -S_G - \phi^\dagger r^2 \left(M_f^\dagger M_f\right) \phi \right\} \\ &= \int \mathcal{D}U \mathcal{D}\phi^\dagger \mathcal{D}\phi \; \exp\left\{ -S_{\text{eff}} \right\}. \end{aligned} \tag{3.1.6}$$

The computation of the determinant has therefore been traded in favor of calculating additional path integrals. Multiple determinants, as present in (2.2.12), are dealt with by simply introducing additional pseudo-fermions.

In order to propose a new gauge field configuration U_f from an existing configuration U_i, the RHMC algorithm uses a molecular dynamics approach. By defining fictitious conjugate momenta

$$\pi_\mu(x) = \sum_{i=1}^{8} \pi_\mu^i(x) T_i \in \mathfrak{su}(3), \quad \pi_\mu^i(x) \in \mathbb{R}, \quad T_i : \text{ Generators of } SU(3) \tag{3.1.7}$$

and a corresponding Hamiltonian

$$H[U, \pi] = \frac{1}{2} \sum_{x,\mu} \mathrm{Tr}[\pi_\mu(x)^2] + S_{\text{eff}}[U], \tag{3.1.8}$$

we can obtain the equations of motion

$$\frac{\mathrm{d}\pi_\mu(x)}{\mathrm{d}t} = -\frac{\partial H}{\partial Q_\mu(x)}, \quad \frac{\mathrm{d}Q_\mu(x)}{\mathrm{d}t} = \frac{\partial H}{\partial \pi_\mu(x)}, \tag{3.1.9}$$

in a fictitious time t, where the conjugate "position" variable $Q_\mu(x)$, an element of the $\mathfrak{su}(3)$-algebra, is related to the link variable $U_\mu(x)$ via

$$U_\mu(x) = \exp\left(i \sum_{i=1}^{8} \omega_\mu^i(x) T_i \right) = \exp\left(i Q_\mu(x) \right). \tag{3.1.10}$$

Evolving the initial gauge field configuration U_i by integrating these equations of motion from $t = 0$ to $t = t_f$ then yields a trajectory through phase space whose endpoint (Q_f, π_f) gives a new gauge field configuration U_f. Finally, a Metropolis acceptance step is performed on U_f which has a high acceptance rate due to the energy conservation of the Hamiltonian equations of motion.

To ensure that this approach correctly samples (3.1.2), two conditions need to be fulfilled: **detailed balance** and **ergodicity**.
Detailed balance is the requirement that the probability to transition from one configuration to the another is the same in the reverse direction, i.e. $P(U_i \to U_f) \overset{!}{=} P(U_f \to U_i)$. Ergodicity on the other hand requires that the algorithm is able to reach any possible configuration starting from an arbitrary one in a finite number of steps.

In the RHMC algorithm, it is achieved by refreshing the initial conjugate momenta π_i for each new trajectory. Detailed balance on the other hand is achieved by using symplectic integrators such as the 2nd order leapfrog scheme. In total, the full RHMC algorithm thus proceeds in four steps:

1. Refreshing conjugate momenta π by drawing a new π_i according to

$$P(\pi) \sim \exp\left(-\frac{1}{2} \mathrm{Tr}(\pi^2) \right). \tag{3.1.11}$$

2. Refreshing pseudo-fermions ϕ by drawing a random η with $P(\eta) \sim \exp(-\eta^*\eta)$ and computing

$$\phi = r\left(M_f^\dagger M_f\right)^{-1}\eta. \tag{3.1.12}$$

3. Integrating the equations of motion to compute U_f.

4. Performing a Metropolis step with a random, uniform $x \in [0,1]$

$$U_f = \begin{cases} U_f & \text{if } \; x \leq \min\left[1, \exp\left\{-\left(H[U_f] - H[U_i]\right)\right\}\right], \\ U_i & \text{if } \; x > \min\left[1, \exp\left\{-\left(H[U_f] - H[U_i]\right)\right\}\right]. \end{cases} \tag{3.1.13}$$

Integrating the equations of motion is by far the most computationally demanding part of this algorithm. While the specific details vary for different integrators, conjugate momenta will be updated regularly during the integration. Schematically, the kth update in the integration may be written as

$$\pi_k = \pi_{k-1} - \delta t F[U_{k-1}, \phi], \tag{3.1.14}$$

where δt is the step-size of the integration and $F[U_k, \phi]$ is a force term computed from the effective action S_{eff}

$$F[U,\phi]_\mu(x) = \frac{\partial S_{\text{eff}}}{\partial Q_\mu(x)} = \sum_{i=1}^{8} T_i \frac{\partial S_{\text{eff}}}{\partial \omega_\mu^i(x)}. \tag{3.1.15}$$

Responsible for the high computational cost of the update is the fermionic contribution to this force. It takes the form

$$\begin{aligned} \frac{\partial S_{\text{eff,F}}}{\partial \omega_\mu^i(x)} =& \frac{\partial}{\partial \omega_\mu^i(x)} \phi^\dagger \bar{r}\left(M_f^\dagger M_f\right)\phi = \frac{\partial}{\partial \omega_\mu^i(x)} \phi^\dagger \left(\bar{\alpha}_0 + \sum_{j=1}^{\bar{k}} \frac{\bar{\alpha}_j}{M_f^\dagger M_f + \bar{\beta}_j}\right)\phi \\ =& -\sum_{j=1}^{\bar{k}} \bar{\alpha}_j \left[\left(\left(M_f^\dagger M_f + \bar{\beta}_j\right)^{-1}\phi\right)^\dagger \frac{\partial\left(D^\dagger D\right)}{\partial \omega_\mu^i(x)} \left(M_f^\dagger M_f + \bar{\beta}_j\right)^{-1}\phi\right], \end{aligned} \tag{3.1.16}$$

and evaluating it involves inverting $M_f^\dagger M_f + \bar{\beta}_i$ for different $\bar{\beta}_i$. A similar calculation has to be performed in the second step of the algorithm as well. In that case, however, only a single inversion is necessary. Fortunately, these types of inversion problems can be solved efficiently by using the multi-shift Conjugate Gradient algorithm [28], which solves the equations

$$(A + \sigma_i)x_i = y \tag{3.1.17}$$

for multiple shifts σ_i at the cost of solving only the smallest shift σ_0. Furthermore, to avoid having to perform two inversions per force evaluation, a different rational approximation $\bar{r}(x) \simeq x^{n_f/4} \simeq r^2(x)$ is used here.

3.2 Analyzing gauge field configurations

Once enough gauge field configurations have been generated, we can use them to compute the expectation values of the physical observables we are interested in. The specific expectation values necessary to compute the conserved charge fluctuation observables that we want to study here, will be given in section 4. For now, it suffices to know that they generally are traces over products of the inverse fermion matrix and derivatives of it, i.e.

$$\mathcal{O} \sim \text{const.} \cdot \text{Tr}\left(M_f^{-1} \frac{\partial^n M_f}{\partial \mu^n} \cdots \right). \tag{3.2.1}$$

Not only do we have to invert the fermion matrices multiple times for these observables, we also need to trace over them. For that, we make use of stochastic estimators. We draw N random pseudofermions η that fulfill

$$\langle \eta_i \rangle = \lim_{N\to\infty} \frac{1}{N} \sum_{k=1}^{N} \eta_i^{(k)} = 0, \quad \text{and} \tag{3.2.2}$$

$$\langle \eta_i \eta_j^* \rangle = \lim_{N\to\infty} \frac{1}{N} \sum_{k=1}^{N} \eta_i^{(k)} (\eta_j^{(k)})^* = \delta_{ij}, \tag{3.2.3}$$

and use them to approximate the trace of an operator A via

$$\text{Tr}(A) = \sum_{i,j} A_{ji}\delta_{ij} \simeq \sum_{i,j} A_{ji} \frac{1}{N} \sum_{k=1}^{N} \eta_i^{(k)} (\eta_j^{(k)})^* = \frac{1}{N} \sum_{k=1}^{N} \eta^{(k)\dagger} A \eta^{(k)}. \tag{3.2.4}$$

A compound operator containing multiple factors of fermion matrix derivatives and inverses is computed step-by-step from right to left. For example, a single contribution to the trace of the simple operator $M_f^{-1} \frac{\partial M_f}{\partial \mu}$ for a given random vector η is calculated by first computing the sparse matrix-vector product $y = \frac{\partial M_f}{\partial \mu}\eta$, which will be described in more detail in section 4.4 (4.4.4), and then using the result as input to solve $M_f x = y$ for x using a Conjugate Gradient (CG) solver. To obtain precise estimates of these traces on a given gauge field configuration, we need to use between 500 to 2000 random vectors. This is quite a costly calculation and without further improvements, it would require significantly more computation time to measure the traces on a given configuration than it costs to even generate that configuration. To bring the cost of these calculations down, we employ multiple algorithmic and technical improvements with the three most impactful ones described below.

Deflation

The computation time of the CG is dominated by the low-lying eigenmodes of the matrix to invert. Therefore, calculating the lowest N_{ev} eigenvalues and eigenvectors and using them to construct an initial guess where these troublesome low-lying modes are taken care of analytically can drastically reduce the total iteration count. With the stochastic estimator approach, sparse matrix inversions are performed for hundreds of different right hand side vectors with the same matrix $M_f[U]$ on a given gauge field configuration U. Thus we can easily amortize the setup costs that comes with calculating the N_{ev} eigenvalues and eigenvectors. Given a random vector η and the N_{ev} lowest eigenvalues λ_i and eigenvectors v_i, the initial guess that we will be using is

$$x_0 = \sum_{i=1}^{N_{ev}} \frac{\langle v_i, \eta \rangle}{\lambda_i}. \tag{3.2.5}$$

To calculate these eigenvalues and -vectors, we use the so-called Thick Restart Lanczos algorithm (TRLan) [29]. In Figure 3.1, we show the effectiveness of this method for a $N_\sigma^3 \times N_\tau = 48^3 \times 12$ gauge field configuration with temperature $T = 157$ MeV. While an inversion without deflation in this particular example requires about 3500 iterations to converge, computing 256 eigenpairs reduces this number to just 280, decreasing the computational cost by a factor 12.5. In practice, we typically compute about 124-256 eigenpairs, depending on the available memory of the Graphics Processing Units (GPUs) used to perform the computations.

Spectral filtering

To decrease the setup cost of deflation, we use a spectral filtering technique. Since we are only interested in the low-lying eigenpairs of $D^\dagger D$ for deflation, we can apply a polynomial filter inside the TRLan algorithm replacing $D^\dagger D \to p(D^\dagger D)$, where $p(x)$ is chosen such that it is large near the origin while suppressing higher parts of the spectrum. A popular choice are carefully tuned Chebychev polynomials [30]. However, a simple exponential filter does a similarly good job in decreasing the computation time while also requiring only very little tuning. By using the filter

$$E_n(\alpha, \beta) = \beta^n \left(1 - \frac{\alpha D^\dagger D}{n}\right)^n, \tag{3.2.6}$$

with $n = 20$ and $\alpha = 6$ and $\beta = 1$, we are able to achieve a speedup of about $\times 5$ for the eigenpair calculation.

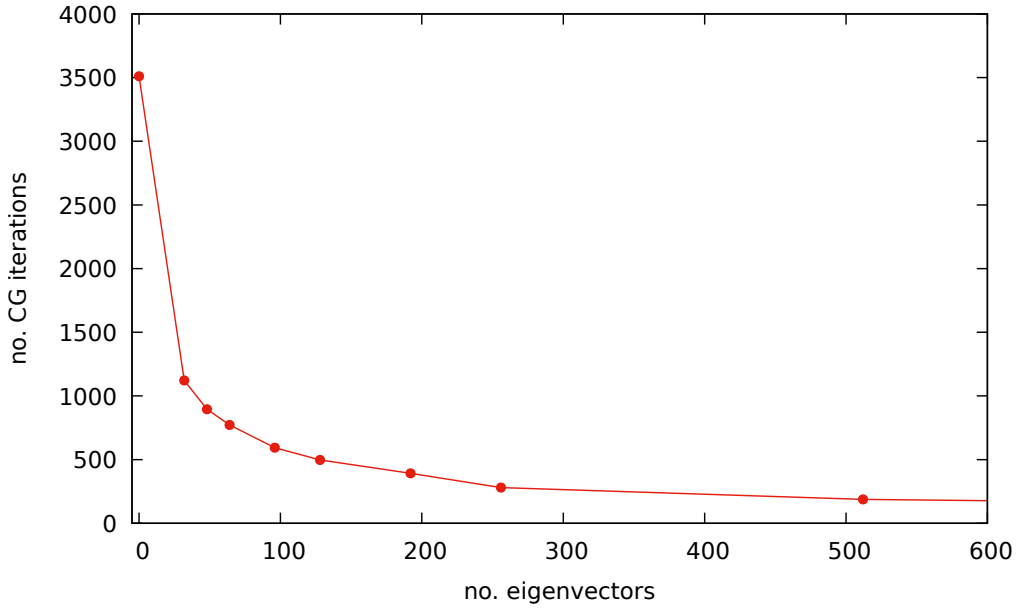

Figure 3.1: Conjugate gradient iteration count for a $48^3 \times 12$ gauge field configuration with $T = 157$ MeV and $m_l = 0.00167$.

Optimized sparse matrix vector products

On a more technical level, a further significant performance improvement is gained by using sparse matrix vector products with multiple right-hand side vectors. As we have argued, both the RHMC and the trace calculations spent most of their run-time in Conjugate Gradient algorithms. In those, the application of the $\not{D}$ operator to a pseudofermion vector ϕ is the dominant part of the computational cost. On a given lattice site x, this sparse matrix vector product is a 4 dimensional stencil operation with with nearest and third nearest neighbor terms that can be read off from the HISQ action described in section 2. It reads

$$\not{D}\phi_x = \sum_{\mu=0}^{4} \left[\left(X_{x,\mu}\phi_{x+\hat{\mu}} - X^{\dagger}_{x-\hat{\mu},\mu}\phi_{x-\hat{\mu}} \right) + \left(W_{x,\mu}\phi_{x+3\hat{\mu}} - W^{\dagger}_{x-3\hat{\mu},\mu}\phi_{x-3\hat{\mu}} \right) \right], \tag{3.2.7}$$

where X and W are the smeared gauge fields introduced earlier. In order to identify possible performance limitations of this kernel, it is helpful to compute its arithmetic intensity: the ratio between performed floating point operations (FLOP) and Bytes read from and written to memory. Comparing this to the ratio of peak FLOP/s to memory bandwidth of the compute device that the code is executing on, gives an idea on which aspects the optimization efforts should focus

on. If the arithmetic intensity of a kernel is much lower than the devices intensity, the kernels performance is limited by the memory bandwidth and the device will spend more time moving data to and from memory then it will spend performing computations. If, on the other hand, the kernels arithmetic intensity exceeds that of the device, the kernels performance will be limited by the speed at which the device can perform floating point operations.

In each of the four directions, the $\not{D}$ kernel computes four products of complex 3×3 matrices with complex 3 component vectors as well as three vector additions totaling 1146 FLOP per site x. At the same time, the kernel reads and writes 1560 Bytes per site if 32 Bit floats are used. The majority of it, 1152 Bytes, come from loading the link matrices V and X. This gives a naive arithmetic intensity of

$$\mathrm{FLOP/Byte}(\not{D}) = \frac{1146\ \mathrm{FLOP/site}}{(1152 + 384 + 96)\,\mathrm{Byte/site}} \simeq 0.7.$$

Modern GPUs, specifically the ones used for the numerical work presented in this thesis, have FLOP/Byte ratios above $\mathcal{O}(10)$ when using 32 Bit floats. Therefore, the performance of the $\not{D}$ kernel is bound by the memory bandwidth on the GPUs and implementations of (3.2.7) should aim to saturate the available bandwidth as much as possible.

As mentioned above, the calculation of traces on a single gauge field configuration requires the use of hundreds of right-hand side vectors. In this situation, the arithmetic intensity of $\not{D}$ can be increased significantly by applying it to multiple of these vectors at once. If applied to n right-hand side vectors, the arithmetic intensity becomes

$$\mathrm{FLOP/Byte}(\not{D})_{n-\mathrm{rhs}} = \frac{n \cdot 1146\ \mathrm{FLOP/site}}{(1152 + n \cdot (384 + 96))\,\mathrm{Byte/site}},$$

because the link matrices only need to be loaded once. Using for example 8 right-hand side vectors already increases the arithmetic intensity to about 1.83, about 2.6 times higher then the single right-hand side version. The performance increase obtained by this approach is demonstrated in Figure 3.2 which shows the achieved TFLOP/s of the $\not{D}$ kernel on recent GPU architectures as a function of the number of right-hand side vectors.

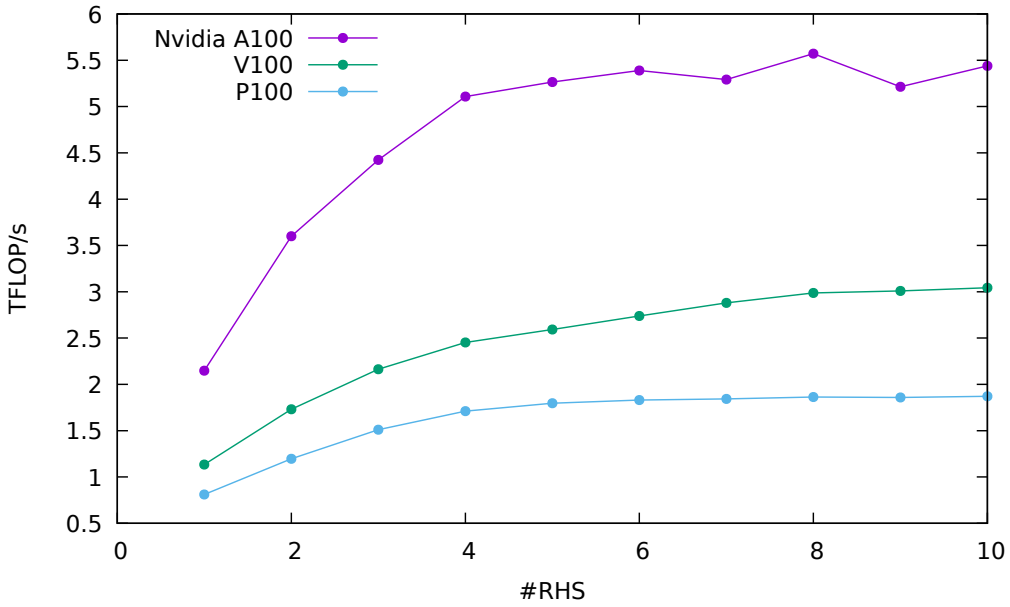

Figure 3.2: Achieved TFLOP/s of the multi-RHS $\not{D}$ kernel on recent GPU architectures.

3.3 Scale setting

The lattice spacing a introduced earlier is not a direct input parameter to our computations. In fact, with proper rescaling of the fields, it does not appear in the discrete lattice action (2.2.10) that forms the basis of our calculations. Nonetheless, the lattice spacing sets the temperature scale and the scale for all physical quantities that we wish to compute and thus needs to be determined as a function of the input parameters i.e. the gauge coupling β and the quark masses m_l and m_s. This is achieved by relating lattice computations of the Sommer parameter a/r_1, a length scale characterized by slope of the static quark potential $V_{q\bar{q}}(r)$

$$r_1^2 \left.\frac{\mathrm{d}V_{q\bar{q}}(r)}{\mathrm{d}r}\right|_{r=r_1} = 1.0, \tag{3.3.1}$$

and the kaon decay constant af_K at given values of β to experimental measurements. For r_1, we use the result published by the MILC Collaboration $r_1 = 0.3106(8)_{\text{stat.}}(14)_{\text{sys.}}(4)_{\text{exp.}}$ fm [31]. For the kaon decay constant, we use the average value $f_K = 155.7/\sqrt{2}$ MeV quoted by FLAG [32]. Both a/r_1 and af_K are

parameterized as

$$a/r_1(\beta) = \frac{c_0 f(\beta) + c_2(10/\beta) f^3(\beta)}{1 + d_2(10/\beta) f^2(\beta)}, \tag{3.3.2}$$

$$af_K(\beta) = \frac{c_0^K f(\beta) + c_2^K(10/\beta) f^3(\beta)}{1 + d_2^K(10/\beta) f^2(\beta)}, \tag{3.3.3}$$

where $f(\beta)$ is the two-loop beta function of QCD with three flavors,

$$f(\beta) = \left(\frac{10 b_0}{\beta}\right)^{-b_1/(2b_0^2)} \exp\left(-\beta/(20 b_0)\right), \tag{3.3.4}$$

with $b_0 = 9/(16\pi^2)$ and $b_1 = 1/(4\pi^4)$.
The specifics of the scale setting procedure are discussed in further detail in our publication [33]. The parameters entering the scales in (3.3.2) are summarized in Table 3.1. As we have briefly mentioned earlier, the temperature in lattice

scale	c_0	c_2	d_2
r_1	43.16(15)	339472(21133)	5452(387)
f_K	7.486(25)	41935(2247)	3273(224)

Table 3.1: Scale setting parameters for (3.3.2).

QCD calculations is given by the inverse of the physical temporal extent aN_τ of the system. Therefore, we can parameterize the temperature as a function of the gauge coupling β with the two different scale setting schemes via

$$T_{f_K} = \frac{1}{N_\tau a f_K} f_K, \tag{3.3.5}$$

$$T_{r_1} = \frac{1}{N_\tau} \frac{r_1}{a} \frac{1}{r_1}. \tag{3.3.6}$$

While both temperature scales converge as the continuum limit $a \to 0$ is approached, they differ at non-zero lattice spacing. To be consistent with earlier works, we use the temperature scale based on af_K when showing results of lattice QCD calculations at finite lattice spacing.

3.4 Setup and statistics

We use the HISQ discretization scheme described in Section 2 for $N_f = 2 + 1$-flavor lattice QCD calculations with two degenerate light quark masses m_l and

a heavier strange quark mass m_s with the ratio $m_s/m_l = 27$ tuned such that physical meson masses are obtained in the continuum limit. In order to perform continuum extrapolations, calculations with three different lattice sizes, $32^3 \times 8$, $42^3 \times 12$ and $64^3 \times 16$ have been performed. At each lattice size, calculations were performed for nine different temperatures ranging from 135 MeV to 175 MeV. For the lattice size $32^3 \times 8$, additional calculations at a temperature of 125 MeV were performed. The number of analyzed gauge field configurations for the different parameters is listed in Table 3.2 below. Successive configurations are separated by 10 unit length RHMC trajectories.

$N_\tau = 8$				$N_\tau = 12$			
β	m_l	T[MeV]	#conf.	β	m_l	T[MeV]	#conf.
6.175	0.003307	125.28	1,471,861				
6.245	0.00307	134.84	1,275,380	6.640	0.00196	135.24	330,447
6.285	0.00293	140.62	1,598,555	6.680	0.00187	140.80	441,115
6.315	0.00281	145.11	1,559,003	6.712	0.00181	145.40	416,703
6.354	0.00270	151.14	1,286,603	6.754	0.00173	151.62	323,738
6.390	0.00257	156.92	1,602,684	6.794	0.00167	157.75	299,029
6.423	0.00248	162.39	1,437,436	6.825	0.00161	162.65	214,671
6.445	0.00241	166.14	1,186,523	6.850	0.00157	166.69	156,111
6.474	0.00234	171.19	373,644	6.880	0.00153	171.65	144,633
6.500	0.00228	175.84	294,311	6.910	0.00148	176.73	131,248

$N_\tau = 16$			
β	m_l	T[MeV]	#conf.
6.935	0.00145	135.80	17671
6.973	0.00139	140.86	23855
7.010	0.00132	145.95	26122
7.054	0.00129	152.19	26965
7.095	0.00124	158.21	21656
7.130	0.00119	163.50	18173
7.156	0.00116	167.53	19926
7.188	0.00113	172.60	17163
7.220	0.00110	177.80	3282

Table 3.2: Simulation parameters and statistics collected on lattices of size $N_\sigma^3 \times N_\tau$ with $N_\sigma = 4N_\tau$ in calculations with light to strange quark mass ratio $m_l/m_s = 1/27$.

Chapter 4

Generalized Susceptibilities at $\mu > 0$

The conserved charge fluctuations that we aim to compute in this thesis are accessible in lattice QCD calculations through generalized susceptibilities that are defined as derivatives of the logarithm of the QCD partition function w.r.t chemical potentials

$$\chi^{BQS}_{ijk}(T,\vec{\mu}) = \frac{1}{VT^3}\frac{\partial^{i+j+k}\ln Z(T,\vec{\mu})}{\partial\hat{\mu}_B^i\partial\hat{\mu}_Q^j\partial\hat{\mu}_S^k}, \;\; \hat{\mu}_X \equiv \frac{\mu_X}{T}. \tag{4.0.1}$$

To simplify the notation, we drop sub- and superscripts whenever the subscripts are zero. For example, we abbreviate $\chi^{BQS}_{200}(T,\vec{\mu}) = \chi^B_2(T,\vec{\mu})$. Forming ratios of two generalized susceptibilities cancels the temperature and volume factors and yields cumulant ratios

$$R^X_{nm}(T,\vec{\mu}) = \frac{\chi^X_n(T,\vec{\mu})}{\chi^X_m(T,\vec{\mu})}, \tag{4.0.2}$$

that have, at least in principle, measurable counterparts in heavy ion collision experiments.

4.1 Taylor expansions for strangeness neutral systems

As our goal is, ultimately, to calculate these quantities at $\mu_B > 0$, we need to employ a method to circumvent the infamous lattice QCD sign problem that prevents us from performing simulations in this parameter region. For small baryon chemical potentials, typically $\mu_B/T < 2$, we can use simple Taylor expansions in μ_B. Expanding the nth order generalized susceptibility χ^X_n for conserved charge

X without introducing further constraints thus simply results in

$$\chi_n^X(T,\mu_B>0)=\sum_{m=n}^{n_{\max}}\frac{1}{m!}\chi_m^X(T,\vec{\mu}=0)\hat{\mu}_B^{m-n},\quad \text{with } X=B,Q,S. \tag{4.1.1}$$

The expansion coefficients of such calculations are then given by generalized susceptibilities $\chi_m^X(T,\vec{\mu}=0)$ of order $m>n$ that can be calculated directly with the methods described in the previous chapter. The specific operators that need to be calculated on the lattice in order to construct these susceptibilities will be discussed in a later section. In order to compute cumulants that represent thermal conditions similar to those found in Pb-Pb or Au-Au heavy ion collision experiments, we have to impose two constraints. Firstly, we impose that the net-strangeness density vanishes

$$n_S\equiv\chi_1^S(T,\vec{\mu})=0, \tag{4.1.2}$$

and secondly, that the ratio r between electric charge density and baryon density is fixed. By relating this ratio to the ratio of proton and baryon numbers N_P and $N_B=N_P+N_N$ of the incident nuclei in Pb-Pb or Au-Au collisions, we obtain

$$\frac{n_Q}{n_B}\equiv\frac{\chi_1^Q(T,\vec{\mu})}{\chi_1^B(T,\vec{\mu})}=\frac{N_P}{N_P+N_N}=r=\simeq 0.4. \tag{4.1.3}$$

We use these constraints to fix the electric charge and strangeness chemical potentials $\hat{\mu}_Q$ and $\hat{\mu}_S$ by expressing them in terms of the baryon chemical potential $\hat{\mu_B}$

$$\hat{\mu}_Q(T,\hat{\mu}_B)=\sum_{i=0}^{\infty}q_i(T)\hat{\mu}_B^i,\qquad \hat{\mu}_S(T,\hat{\mu}_B)=\sum_{i=0}^{\infty}s_i(T)\hat{\mu}_B^i. \tag{4.1.4}$$

Requiring (4.1.2) and (4.1.3) at each order in $\hat{\mu_B}$ in (4.1.4) gives us two linear equations that we can solve for the coefficients q_i and s_i. To illustrate this in more detail, we write the expansion of (4.1.2) to leading order explicitly

$$n_S=\chi_1^S(T,\vec{\mu})=\hat{\mu}_B\left(\chi_{11}^{BS}+\chi_{11}^{QS}\frac{\partial\hat{\mu}_Q}{\partial\hat{\mu}_S}+\chi_2^S\frac{\partial\hat{\mu}_S}{\hat{\mu}_B}\right)+\mathcal{O}(\hat{\mu}_B^3)\stackrel{!}{=}0 \tag{4.1.5}$$

$$\Rightarrow\chi_{11}^{BS}+\chi_{11}^{QS}q_1+\chi_2^Ss_1\stackrel{!}{=}0. \tag{4.1.6}$$

Here, we have adopted the convention $\chi_{ijk}^{BQS}\equiv\chi_{ijk}^{BQS}(T,\vec{\mu}=0)$ for notational convenience. The susceptibility $\chi_1^S(T,\hat{\mu}=0)$ and generally all odd order generalized susceptibilities at $\hat{\mu}=0$ vanish [34] and the derivatives of the chemical

potentials $\hat{\mu}_Q$ and $\hat{\mu}_S$ yield the coefficients q_1 and s_1. Solving this for either q_1 or s_1 and inserting the result into the leading order expansion of (4.1.3)

$$\frac{n_Q}{n_B} = \frac{\chi_{11}^{BQ} + \chi_2^Q q_1 + \chi_{11}^{QS} s_1}{\chi_2^B + \chi_{11}^{BQ} q_1 + \chi_{11}^{BS} s_1} \stackrel{!}{=} r, \tag{4.1.7}$$

gives the solutions

$$s_1 = -\frac{q_1 \chi_{11}^{QS} + \chi_{11}^{BS}}{\chi_2^S}, \quad q_1 = \frac{\chi_2^S \chi_{11}^{BQ} - r\chi_2^B \chi_2^S - \chi_{11}^{QS}\chi_{11}^{BS} + r\left(\chi_{11}^{BS}\right)^2}{\left(\chi_{11}^{QS}\right)^2 - \chi_2^Q \chi_2^S + r\chi_{11}^{BQ}\chi_2^S - r\chi_{11}^{BS}\chi_{11}^{QS}}. \tag{4.1.8}$$

The higher order coefficients are obtained analogously and their expression can be found in [35]. Armed with these coefficients, we can then compute the constrained expansions of n-th order cumulants

$$\chi_n^X(T, \mu_B) = \sum_{k=0}^{k_{\max}} \tilde{\chi}_n^{X,k}(T)\hat{\mu}_B^k, \quad \text{where} \quad \tilde{\chi}_n^{X,k}(T) = \left.\frac{\partial^k \chi_n^X}{\partial \hat{\mu}_B^k}\right|_{\substack{n_S=0 \\ n_Q/n_B=r}}. \tag{4.1.9}$$

The full expressions for the constrained expansions of the cumulants are listed in appendix A. Inserting these expansions into (4.0.2) finally gives us cumulant ratios that only depend on temperature T and baryon chemical potential μ_B

$$R_{nm}^X(T, \mu_B) = \frac{\sum_{k=0}^{k_{\max}} \tilde{\chi}_n^{X,k}(T)\hat{\mu}_B^k}{\sum_{l=0}^{l_{\max}} \tilde{\chi}_m^{X,l}(T)\hat{\mu}_B^l}. \tag{4.1.10}$$

4.2 Mapping χ_{ijk}^{BQS} to quark number susceptibilities

In order to calculate (4.1.10), we need to compute the susceptibilities χ_{ijk}^{BQS} for all combinations i, j, k with $i + j + k \leq N_{\max}$ as we have seen above. However, we need to discus how to relate these to operators that we can calculate in lattice QCD simulations. To derive them, we have to introduce the chemical potentials μ_B, μ_Q and μ_S into our lattice formulation. Taking derivatives of our lattice QCD partition function with respect to these will then yield operators that we can evaluate at $\vec{\mu} = 0$. As our lattice formulation includes quarks and gluons rather then hadrons, we need to first map our baryon-, charge-, and strangeness chemical potentials to chemical potentials in the quark basis. This is achieved by relating

$$\mu_B = \mu_u + 2\mu_d, \quad \mu_Q = \mu_u - \mu_d, \quad \mu_S = -\mu_s. \tag{4.2.1}$$

In turn, we can relate derivatives with respect to μ_B, μ_Q and μ_S to quark chemical potential derivatives via

$$\frac{\partial}{\partial \mu_B} = \frac{1}{3}\left(\frac{\partial}{\partial \mu_u} + \frac{\partial}{\partial \mu_d} + \frac{\partial}{\partial \mu_s}\right), \tag{4.2.2}$$

$$\frac{\partial}{\partial \mu_Q} = \frac{1}{3}\left(2\frac{\partial}{\partial \mu_u} - \frac{\partial}{\partial \mu_d} - \frac{\partial}{\partial \mu_s}\right), \tag{4.2.3}$$

$$\frac{\partial}{\partial \mu_S} = -\frac{\partial}{\partial \mu_s}. \tag{4.2.4}$$

Higher order derivatives of $\ln Z$ with respect to these can then be expressed conveniently by defining

$$\mathcal{D}^f_i = \frac{1}{4}\frac{\partial^i}{\partial \mu^i_f} \ln\det M_f, \tag{4.2.5}$$

which we use to write

$$\mathcal{A}^{uds}_{ijk} \equiv \frac{1}{Z}\frac{\partial^{i+j+k} Z}{\partial \mu^i_u \mu^j_d \mu^k_s} = \left\langle a^u_i a^d_j a^s_k \right\rangle \quad \text{with} \quad a^f_n = \exp\left\{-\mathcal{D}^f_0\right\} \frac{\partial^n \exp\left\{\mathcal{D}^u_0\right\}}{\partial \mu^n_f}. \tag{4.2.6}$$

The first μ_u derivative gives, for example, $\frac{\partial \ln Z}{\partial \mu_u} = \mathcal{A}^u_1 = \langle \mathcal{D}^u_1 \rangle$ and higher order derivatives can be computed iteratively. An additional μ_u-derivative can be expressed as

$$\frac{\partial}{\partial \mu_u}\mathcal{A}^{uds}_{ijk} = \mathcal{A}^{uds}_{i+1,j,k} - A^{uds}_{ijk} A^u_1, \tag{4.2.7}$$

and explicit expressions for the lowest four orders are

$$\mathcal{A}^u_1 = \langle \mathcal{D}^u_1 \rangle, \tag{4.2.8}$$

$$\mathcal{A}^u_2 = \langle \mathcal{D}^u_2 \rangle + \left\langle (\mathcal{D}^u_1)^2 \right\rangle, \tag{4.2.9}$$

$$\mathcal{A}^u_3 = \langle \mathcal{D}^u_3 \rangle + 3\left\langle \mathcal{D}^u_2 \mathcal{D}^u_1 \right\rangle + \left\langle (\mathcal{D}^u_1)^3 \right\rangle \tag{4.2.10}$$

$$\mathcal{A}^u_4 = \langle \mathcal{D}^u_4 \rangle + 4\left\langle \mathcal{D}^u_3 \mathcal{D}^u_1 \right\rangle + 3\left\langle (\mathcal{D}^u_2)^2 \right\rangle + +6\left\langle \mathcal{D}^u_2 (\mathcal{D}^u_1)^2 \right\rangle + \left\langle (\mathcal{D}^u_1)^4 \right\rangle. \tag{4.2.11}$$

Iterating (4.2.7) gives us for the four lowest order derivatives of $\ln Z$

$$\frac{\partial \ln Z}{\partial \mu_u} = \mathcal{A}^u_1, \tag{4.2.12}$$

$$\frac{\partial^2 \ln Z}{\partial \mu^2_u} = \mathcal{A}^u_2 - (\mathcal{A}^u_1)^2, \tag{4.2.13}$$

$$\frac{\partial^3 \ln Z}{\partial \mu^3_u} = \mathcal{A}^u_3 - 3\mathcal{A}^u_2 \mathcal{A}^u_1 + 2(\mathcal{A}^u_1)^3, \tag{4.2.14}$$

$$\frac{\partial^4 \ln Z}{\partial \mu^4_u} = \mathcal{A}^u_4 - 4\mathcal{A}^u_3 \mathcal{A}^u_1 - 3(\mathcal{A}^u_2)^2 + 12\mathcal{A}^u_2 (\mathcal{A}^u_1)^2 - 6(\mathcal{A}^u_1)^4. \tag{4.2.15}$$

The formulas for other flavors and combinations of them are of course obtained analogously. As we are evaluating these quantities at $\vec{\mu} = 0$, all odd order derivatives vanish so the expressions simplify significantly. Finally, we can use (4.2.2) together with the above results to compute the generalized susceptibilities χ_{ijk}^{BQS}. For example, the baryon number variance χ_2^B is obtained via

$$\chi_2^B = \frac{1}{9}\left(\chi_{002}^{uds} + 2\chi_{011}^{uds} + \chi_{020}^{uds} + 2\chi_{101}^{uds} + 2\chi_{110}^{uds} + \chi_{200}^{uds}\right), \tag{4.2.16}$$

where $\chi_{ijk}^{uds} = \frac{\partial^{i+j+k} \ln Z}{\partial \mu_u^i \partial \mu_d^j \partial \mu_s^k}$ are the quark number susceptibilities.

4.3 Chemical potential on the lattice

With the link between BQS susceptibilities χ_{ijk}^{BQS} and the quark number susceptibilities established, we now need to discus how to calculate $\mathcal{D}_i^f$ defined in (4.2.5). For that, we need to know how the chemical potential enters the lattice theory. In the continuum theory, a chemical potential would multiply the conserved charge

$$\hat{Q}_f = \int \mathrm{d}^3x \bar{\psi}_f(x)\gamma_0\psi_f(x), \tag{4.3.1}$$

which can be translated to the lattice theory by modifying the temporal link variables

$$\begin{aligned} U_0(x) &\to (1 + a\mu)\, U_0(x) \\ U_0^\dagger(x) &\to (1 - a\mu)\, U_0^\dagger(x). \end{aligned} \tag{4.3.2}$$

However, it was shown in [36] that this leads to a quadratic divergence in the energy density for free fermions. This can be avoided by introducing the chemical potential exponentially

$$\begin{aligned} U_0(x) &\to \exp(a\mu)\, U_0(x) \\ U_0^\dagger(x) &\to \exp(-a\mu)\, U_0^\dagger(x). \end{aligned} \tag{4.3.3}$$

4.4 Trace operators

Once the temporal gauge links have been modified with the exponential factors arising from the chemical potentials being non-zero, we can compute (4.2.5) ex-

plicitly. For the first four orders, we find

$$D_1^f = \frac{1}{4}\mathrm{Tr}\left(M_f^{-1}\frac{\partial M_f}{\partial \mu}\right), \tag{4.4.1}$$

$$\begin{aligned}
D_2^f &= \frac{1}{4}\mathrm{Tr}\left(M_f^{-1}\frac{\partial^2 M_f}{\partial \mu^2}\right) - \frac{1}{4}\mathrm{Tr}\left(M_f^{-1}\frac{\partial M_f}{\partial \mu}M_f^{-1}\frac{\partial M_f}{\partial \mu}\right), \\
D_3^f &= \frac{1}{4}\mathrm{Tr}\left(M_f^{-1}\frac{\partial^3 M_f}{\partial \mu^3}\right) - \frac{1}{4}\mathrm{Tr}\left(M_f^{-1}\frac{\partial M_f}{\partial \mu}M_f^{-1}\frac{\partial^2 M_f}{\partial \mu^2}\right) \\
&\quad + \frac{2}{4}\mathrm{Tr}\left(M_f^{-1}\frac{\partial M_f}{\partial \mu}M_f^{-1}\frac{\partial M_f}{\partial \mu}M_f^{-1}\frac{\partial M_f}{\partial \mu}\right) - \frac{2}{4}\mathrm{Tr}\left(M_f^{-1}\frac{\partial^2 M_f}{\partial \mu^2}M_f^{-1}\frac{\partial M_f}{\partial \mu}\right), \\
D_4^f &= \frac{1}{4}\mathrm{Tr}\left(M_f^{-1}\frac{\partial^4 M_f}{\partial \mu^4}\right) - \mathrm{Tr}\left(M_f^{-1}\frac{\partial M_f}{\partial \mu}M_f^{-1}\frac{\partial^3 M_f}{\partial \mu^3}\right) \\
&\quad - \frac{3}{4}\mathrm{Tr}\left(M_f^{-1}\frac{\partial^2 M_f}{\partial \mu^2}M_f^{-1}\frac{\partial^2 M_f}{\partial \mu^2}\right) \\
&\quad + 3\mathrm{Tr}\left(M_f^{-1}\frac{\partial M_f}{\partial \mu}M_f^{-1}\frac{\partial M_f}{\partial \mu}M_f^{-1}\frac{\partial^2 M_f}{\partial \mu^2}\right) \\
&\quad - \frac{3}{2}\mathrm{Tr}\left(M_f^{-1}\frac{\partial M_f}{\partial \mu}M_f^{-1}\frac{\partial M_f}{\partial \mu}M_f^{-1}\frac{\partial M_f}{\partial \mu}M_f^{-1}\frac{\partial M_f}{\partial \mu}\right).
\end{aligned} \tag{4.4.2}$$

From these first four orders, it already becomes clear that the number of operators that need to be calculated on the lattice increases rapidly with the number of μ derivatives. Fortunately, it was found in [37][38] that the divergences that plague the linear μ formulation only appear in observables with four or fewer μ derivatives and higher order observables are free from divergences. Furthermore, both formulations agree with each other at these higher orders. Therefore, we can use the linear μ formulation for calculating D_i^f with $i > 4$. In that case, the expressions simplify significantly and all we need to compute is

$$D_n^f = \frac{1}{4}(-1)^{n+1}\,(n-1)!\;\mathrm{Tr}\left(\left(M_f^{-1}\frac{\partial M_f}{\partial \mu}\right)^n\right). \tag{4.4.3}$$

The fermion matrix derivatives that appear in these expressions are given by

$$\begin{aligned}
\frac{\partial^n M_f}{\partial \mu^n}\chi &= c_1\left(U_0(x)\chi(x+\hat{0}) - (-1)^n U_0^\dagger(x-\hat{0})\chi(x-\hat{0})\right) \\
&\quad + 3^n c_3\left(N_0(x)\chi(x+3\cdot\hat{0}) - (-1)^n N_0^\dagger(x-3\cdot\hat{0})\chi(x-3\cdot\hat{0})\right),
\end{aligned} \tag{4.4.4}$$

where $N_0(x) = U_0(x)U_0(x+\hat{0})U_0(x+2\cdot\hat{0})$ denotes the temporal Naik link.

Chapter 5

Second order cumulants and the HRG

Having reviewed the theoretical foundations as well as numerical algorithms and formulas for our lattice QCD calculations of cumulants of conserved charge fluctuations, we now want to change the focus towards the results of our computations. We start this presentation of results in this chapter with a discussion of second order cumulants and a detailed comparison to different hadron resonance gas models that we describe below. This chapter is based on our publication [33].

5.1 Hadron Resonance Gas

Before the formulation of QCD itself, Hagedorn formulated the statistical boostrap model in an attempt to describe the behavior of strongly interacting matter. Within the statistical boostrap model, Hagedorn was able to derive an upper limit for the temperature, now known as the Hagedorn temperature T_H, above which the partition function diverges and hadrons can no longer be stable. This marked one of the first hints towards the existence of phases of strongly interacting matter other then the hadronic phase and his estimated Hagedorn temperature $T_H \approx 150$ MeV [39][40] is very close to the pseudo-critical transition temperature $T_{\mathrm{pc}} = 156.5 \pm 1.5$ MeV that is well established through lattice QCD calculations today [9]. Eventually, these studies culminated in the formulation of the hadron resonance gas (HRG) model which models the partition function of strongly interacting matter through non-interacting, point-like mesons and baryons following Bose-Einstein and Fermi-Dirac statistics, respectively. Concretely, the logarithm

of the HRG partition function reads

$$\ln Z_{\mathrm{HRG}}(T,V,\vec{\mu}) = \sum_{i\in\mathrm{mesons}} \ln Z_i^M(T,V,\vec{\mu}) + \sum_{j\in\mathrm{baryons}} \ln Z_j^B(T,V,\vec{\mu}), \quad (5.1.1)$$

$$\text{with} \quad \ln Z_i^{M/B} = \mp \frac{V d_i}{2\pi^2} \int_0^\infty \mathrm{d}k\; k^2 \ln(1 \mp z_i e^{-\epsilon_i/T}),$$

$$\text{and} \quad \epsilon_i^2 = k^2 + m_i^2, \quad z_i = e^{\left(B_i\mu_B + Q_i\mu_Q + S_i\mu_S\right)/T}.$$

The sums are taken over a chosen spectrum of hadrons and their resonances. m_i labels their respective masses while the factors B_i, Q_i and S_i appearing in the fugacity z_i label the states quantum numbers and d_i counts the spin degrees of freedom. By expressing the integral in (5.1.1) via modified Bessel functions of the second kind, we can write the logarithm of $Z_i^{M/B}$ as

$$\ln Z_i^{M/B} = \frac{VT^3}{2\pi^2} d_i \left(\frac{m_i}{T}\right)^2 \sum_{l=1}^{\infty} (\pm 1)^{l+1} \frac{z_i^l}{l^2} K_2(l m_i/T). \quad (5.1.2)$$

Due to the asymptotic behavior of the modified Bessel function

$$K_2(x) \sim \sqrt{\frac{\pi}{2x}} e^{-x} \quad \text{for } x \gg 1, \quad (5.1.3)$$

and the large mass of even the lightest baryon compared to the temperature scale, contributions with $l > 1$ can be neglected in the baryon term. We then obtain the formulas necessary for computing the generalized susceptibilities χ_{ijk}^{BQS} by differentiating with respect to the different chemical potentials appearing in the fugacity z_i

$$\chi_{ijk}^{BQS} = \delta_{i,0} \sum_{a\in\mathrm{mesons}} \frac{d_a m_a^2}{2\pi^2 T^2} \sum_{l=1}^{\infty} \frac{z_a^l (l Q_a)^j (l S_a)^k}{l^2} K_2(l m_a/T) \quad (5.1.4)$$

$$+ \sum_{b\in\mathrm{baryons}} \frac{d_b m_b^2}{2\pi^2 T^2} z_b B_b^i Q_b^j S_b^k K_2(m_b/T).$$

The list of hadronic states curated by the Particle Data Group (PDG) [41] is often used for the hadronic spectrum in many HRG calculations. Going forward, we will label the HRG model based on this list as the PDG-HRG model. Other popular choices are spectra based on the PDG list but extended by not yet established states predicted by the Quark Model which we will label as QM-HRG models. Further approaches that go beyond the use of non-interacting and point-like hadron resonances include the phenomenology inspired excluded volume HRG model (EV-HRG) where a hard core radius r is assigned to baryons through a

finite volume parameter $b = 16\pi r^3/3$, as well as models based on relativistic virial expansions [42]. These models generally contain free parameters that need to be determined by fitting to lattice QCD calculations of a set of thermodynamic observables.

Due to their success in describing hadron yields in heavy-ion collision experiments, HRG models are often used to determine freeze-out parameters $(T_f, \mu_{B,f}, \mu_{Q,f}, \mu_{S,f})$ characterizing the thermal conditions present at hadronization [43][44]. A similar determination of freeze-out parameters based on particle yields from first principle lattice QCD calculations is not possible as these are not observables that can be derived from the QCD partition function. Therefore, it is important to quantify the range of validity in which hadron resonance gas models provide a good description of QCD in order to understand systematic uncertainties that might arise from such model dependent determinations of $(T_f, \mu_{B,f}, \mu_{Q,f}, \mu_{S,f})$.

For this purpose, we will provide high-precision, continuum extrapolated lattice QCD calculations of second order cumulants of baryon number, electric charge and strangeness fluctuations and their cross correlations in this section. We will focus on calculations at vanishing chemical potential, as it allows us to constrain the fundamental model parameters of HRG models such as the excluded volume parameter b of EV-HRG models.

5.2 Continuum extrapolation of second order cumulants

Making use of the high statistics data set listed in Table 3.2, we present continuum extrapolations of all six second order cumulants of baryon number, electric charge and strangeness

$$\chi_{ijk}^{BQS} = \frac{1}{VT^3} \frac{\partial \ln Z(T,V,\vec{\mu})}{\partial \hat{\mu}_B^i \partial \hat{\mu}_Q^j \partial \hat{\mu}_S^k}\bigg|_{\hat{\mu}=0} \quad \text{with} \;\; i+j+k=2. \tag{5.2.1}$$

As our numerical calculations are based on the HISQ discretization scheme with (2+1)-flavors with a physical strange quark mass and two physical light quark masses, these six second order cumulants are not independent from each other. Rather, only four of them are independent while the remaining two are constrained by the isospin symmetry imposed by our choice of discretization scheme. This symmetry leads to the two constraints in the (B, Q, S) basis

$$\chi_2^S = 2\chi_{11}^{QS} - \chi_{11}^{BS}, \tag{5.2.2}$$

$$\chi_2^B = 2\chi_{11}^{BQ} - \chi_{11}^{BS}. \tag{5.2.3}$$

In the (u, d, s) basis, this simply reflects the two conditions $\chi_2^u = \chi_2^d$ and $\chi_{11}^{us} = \chi_{11}^{ds}$. Furthermore, these constraints are also fulfilled to better than 1% accuracy in HRG models based on the PDG spectrum as well as those using spectra extended by states predicted by relativistic quark models. Therefore, all second order cumulants in either of the two basis can be obtained from a set of four independent observables which we can choose freely. In this work, we focus on χ_2^Q, χ_{11}^{QS}, χ_{11}^{BQ} and χ_{11}^{BS}, the first two of which are dominated by the non-strange and strange meson spectrum while the latter two are dominated by the non-strange and strange baryon spectrum.

In order to obtain cumulants at the same temperature for each of the four lattice sizes, we use cubic spline interpolations in the temperature interval $T \in$ [134 MeV : 178 MeV]. Error bands on the interpolations have been calculated using a bootstrap analysis with 800 bootstrap samples. The interpolations have been performed for both temperature scales and the uncertainties of f_K and r_1 are included as systematic errors. Continuum extrapolations of the cumulants based on both temperature scales were then performed using linear extrapolations in $1/N_\tau^2$,

$$f_2(T, N_\tau) = f_2(T) + \frac{a}{N_\tau^2}. \tag{5.2.4}$$

The results of this procedure are shown in Figure 5.1. Continuum extrapolations including further $1/N_\tau^4$ corrections can be found in [33]. Slight discrepancies between the extrapolations based on T_{f_K} and T_{r_1} are visible at $1/N_\tau^2 = 0$. These stem from systematic errors in the parametrization of a/r_1 and af_K at finite gauge coupling. Therefore, the results of the two different linear fits are averaged to yield a final continuum extrapolation and the difference between the two fit results is taken as a systematic error that is added linearly to the statistical errors of the two extrapolations. The continuum extrapolations of the cumulants are shown in Figures 5.2 and 5.3. The systematic error arising from the uncertainty in the scale, caused by experimental uncertainties in f_π and r_1, is shown as a red band while the combined systematic and statistical error stemming from the continuum extrapolation using two different temperature scales is shown as a gray band. A comparison between these continuum extrapolations and hadron resonance gas model calculations based on the QMHRG2020 spectrum, described in [33], is shown in the insets of these figures. The full list of hadrons used in QMHRG2020 is provided in [48]. In Table 5.1 we summarize the results at temperatures between 135 MeV and 175 MeV in steps of 5 MeV and compare them to corresponding results from [45]. The agreement between both analyses is very good.

When performing the continuum extrapolations of second order cumulants, we did not assume any specific ansatz for the temperature dependence of the cumulants. To simplify comparisons to other models, it is however beneficial to have a

proper parametrization of our results. For this purpose, we provide a parametrization of the cumulants in terms of polynomial fractions,

$$\chi_{11}^{XY}(T) = \frac{\sum_{k=0}^{3} n_k^{XY} \bar{t}^k}{1 + \sum_{k=1}^{3} d_k^{XY} \bar{t}^k}, \quad \bar{t} = \left(1 - \frac{T_{pc,0}}{T}\right), \tag{5.2.5}$$

where $X, Y \in B, Q, S$, and it is understood that $\chi_{11}^{XY} = \chi_2^X$ if $X = Y$. This parametrization corresponds to the central value of the error bands shown in Figures 5.2 and 5.3 and the resulting coefficients for each of the cumulants are listed in Table 5.2.

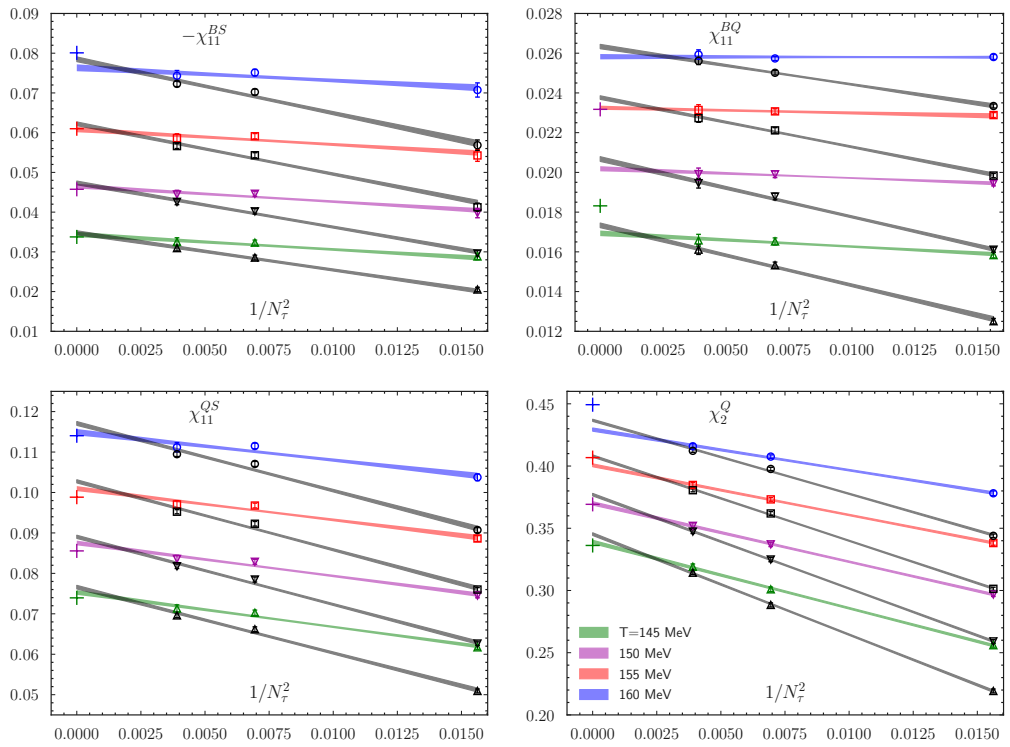

Figure 5.1: Continuum extrapolations of the four independent second order cumulants χ_{11}^{BS} (top left), χ_{11}^{BQ} (top right), χ_{11}^{QS} (bottom left) and χ_2^Q (bottom right) at temperatures ranging from 145 MeV to 160 MeV. The colored data points and lines correspond to the af_K scale, whereas the black data points and lines correspond to a/r_1. The colored crosses at $1/N_\tau^2$ display the value obtained from QM-HRG calculations based on the QMHRG2020 spectrum [33]. The QM-HRG results for χ_2^Q were obtained with finite-volume corrections for pions and kaons in a volume $LT = N_\sigma/N_\tau = 4$.

T [MeV]	χ_{11}^{QS}		$(\chi_2^Q)_{LT=4}$	χ_2^B	χ_2^S
	this work	[45]	this work	this work	this work
135	0.0576(13)(6)	0.0604(20)	0.285(4)(2)	0.0422(22)(10)	0.134(4)(2)
140	0.0655(10)(9)	0.0699(18)	0.312(4)(3)	0.0532(14)(14)	0.156(2)(2)
145	0.0760(12)(12)	0.0806(20)	0.342(4)(3)	0.0689(15)(18)	0.187(3)(3)
150	0.0883(12)(13)	0.0914(12)	0.374(5)(3)	0.0878(18)(20)	0.224(3)(4)
155	0.1018(14)(14)	0.1045(9)	0.404(5)(3)	0.1085(22)(21)	0.266(4)(4)
160	0.1160(16)(14)	0.1193(15)	0.433(5)(3)	0.1296(26)(21)	0.310(5)(4)
165	0.1300(18)(14)	0.1345(20)	0.458(5)(2)	0.1497(28)(19)	0.354(6)(4)
170	0.1434(20)(12)	0.1478(22)	0.476(4)(1)	0.1673(27)(15)	0.396(7)(4)
175	0.1553(26)(12)	0.1600(23)	0.489(4)(1)	0.1809(29)(11)	0.435(8)(4)

T [MeV]	χ_{11}^{BQ}		χ_{11}^{BS}	
	this work	[45]	this work	[45]
135	0.0114(5)(2)	0.0101(8)	-0.0197(15)(3)	-0.0167(17)
140	0.0140(4)(3)	0.0124(8)	-0.0251(7)(7)	-0.0227(13)
145	0.0172(4)(3)	0.0162(12)	-0.0345(8)(11)	-0.0332(18)
150	0.0204(4)(3)	0.0217(17)	-0.0469(10)(14)	-0.0491(28)
155	0.0235(4)(3)	0.0242(10)	-0.0616(14)(15)	-0.0676(38)
160	0.0261(4)(2)	0.0266(7)	-0.0775(20)(16)	-0.0825(27)
165	0.0280(3)(1)	0.0278(6)	-0.0938(22)(15)	-0.0981(26)
170	0.0288(2)(0)	0.0277(4)	-0.1097(24)(14)	-0.1136(23)
175	0.0281(3)(1)	0.0269(4)	-0.1244(30)(12)	-0.1296(24)

Table 5.1: Continuum extrapolated results for the six second order cumulants obtained at different temperature values. The first error corresponds to the combined statistical and systematic errors stemming from the continuum extrapolation while the second error corresponds to the uncertainty in the physical value of r_1. For χ_2^Q we include an indication that these results have been obtained on lattices with aspect ratio $LT \equiv N_\sigma/N_\tau = 4$ as they are particularly sensitive to finite volume effects. For comparison, results from Bellwied et al. [45] for off-diagonal cumulants are also shown.

	χ_{11}^{BQ}	χ_{11}^{QS}	χ_{11}^{BS}	χ_2^Q	χ_2^B	χ_2^S
n_0^{XY}	0.0243	0.106	-0.066	0.413	0.115	0.279
n_1^{XY}	0.0122	0.0629	-0.327	-0.159	0.328	-1.172
n_2^{XY}	-0.376	-0.6097	0.0290	-2.099	-0.933	-6.661
n_3^{XY}	-1.219	-3.896	3.834	-6.362	-6.522	-28.378
d_1^{XY}	-3.036	-3.572	-2.505	-2.605	-2.922	-9.135
d_2^{XY}	3.006	3.166	2.952	1.677	3.189	13.624
d_3^{XY}	-2.133	-5.080	3.0973	3.892	-0.245	-66.402

Table 5.2: Parametrization of second order cumulants corresponding to the central values of the fits shown in Figures 5.2 and 5.3 in the interval $T \in [135\ \mathrm{MeV} : 175\ \mathrm{MeV}]$.

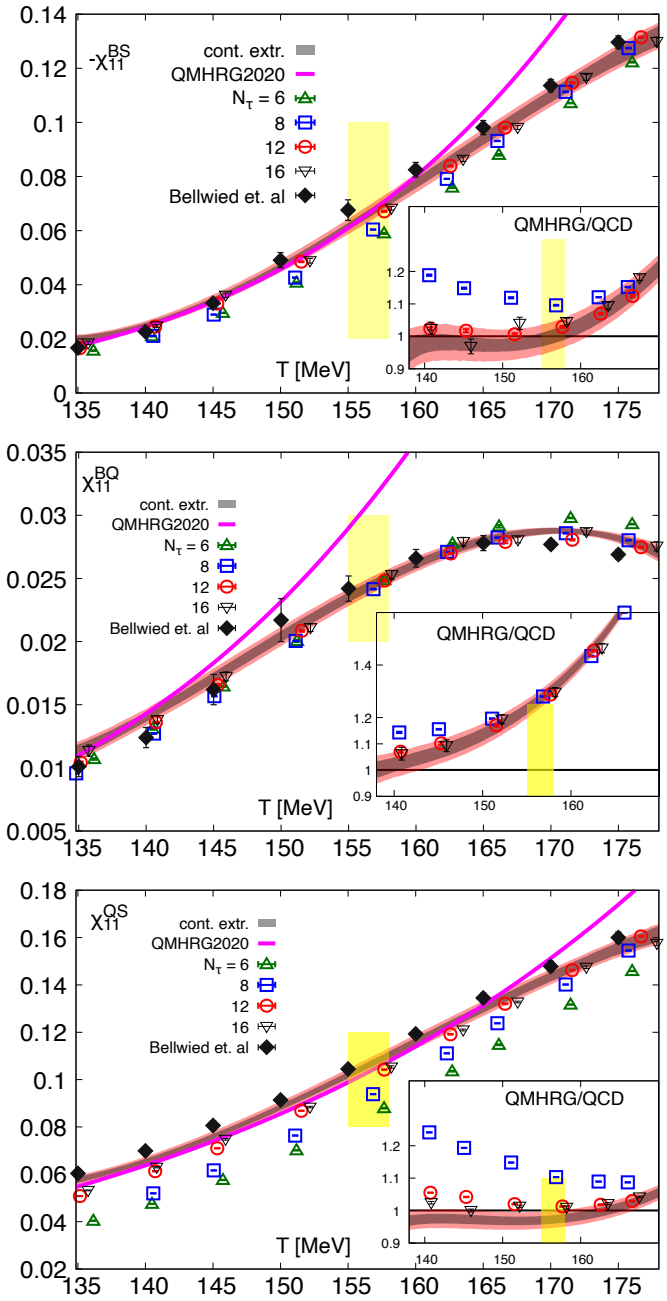

Figure 5.2: Second order off-diagonal cumulants as a function of temperature. QM-HRG model results based on the QMHRG2020 spectrum [33] are included as colored lines. The insets show the ratio of these HRG model calculations and continuum extrapolated lattice QCD results. Results from Bellwied et al [45] are also shown. The data points at finite values of N_τ are based on the af_K temperature scale and the yellow band corresponds to the crossover temperature $T_{pc,0}$.

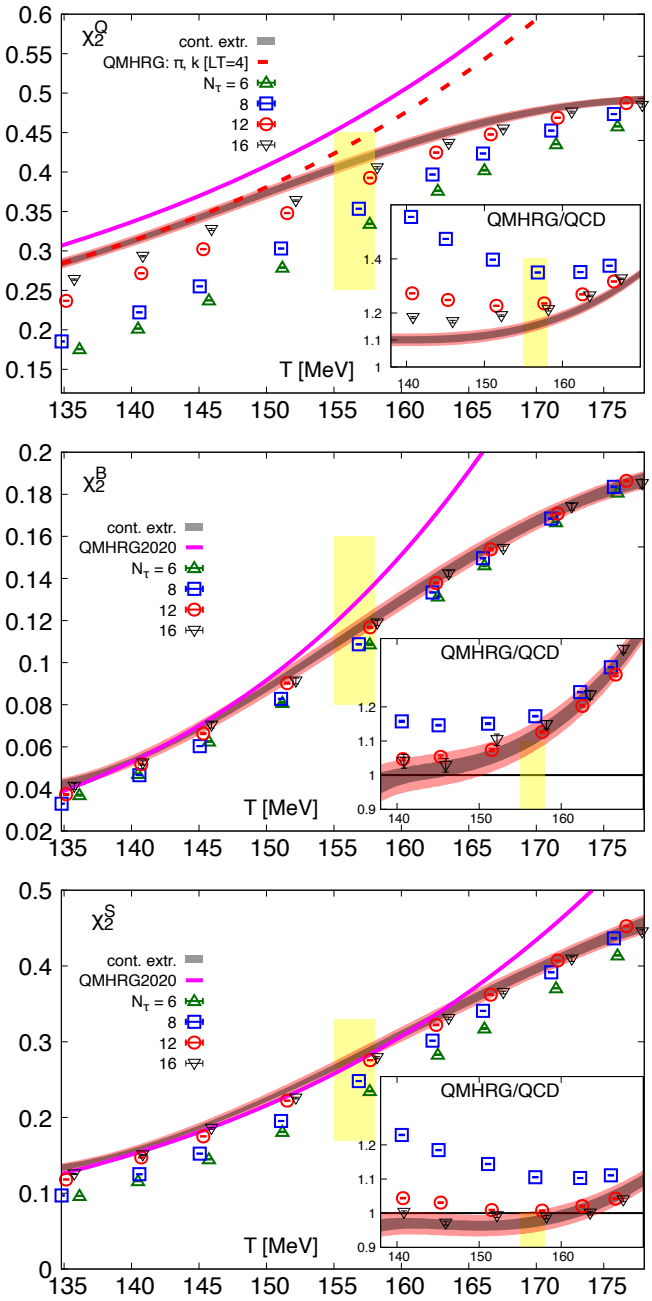

Figure 5.3: Second order diagonal cumulants as a function of temperature with QM-HRG results and insets as in Figure 5.2.

5.3 Comparison with HRG models

The chosen hadronic spectrum in HRG model calculations has a significant influence on the resulting thermodynamic quantities. While the list of experimentally confirmed hadronic states and resonances maintained by the particle data group [41] gives a lot of information on the spectrum to use in such models, it has been pointed out in [46], that this information alone is insufficient to obtain a satisfactory agreement of second order cumulants calculated within HRG models and those obtained from first principle lattice QCD calculations. In particular, strangeness fluctuations and their correlations with baryon number fluctuations and electric charge fluctuations seem to require additional strange hadron resonances in the baryonic sector of the spectrum in order to reasonably match QCD calculations. Including such additional resonances, for example by adding resonances predicted by quark model calculations is, however, not unique.

Furthermore, the description of strongly interacting matter in terms of non-interacting, point-like resonances does not account for repulsive interactions as well as the interplay between repulsive and attractive interactions. The effects of these interactions and their interplay can have significant effects on some resonances. For the strange meson $K_0^*(700)$, for example, partial wave analyses revealed that this resonance hardly contributes to the thermodynamic behavior of strong interaction matter as its contribution is strongly suppressed [47]. Therefore, $K_0^*(700)$ should not be included in HRG model calculations of point-like, non-interacting hadrons although it is a well-established resonance in the PDG lists.

In order to account for these difficulties, we use a spectrum coined *QMHRG2020* as our baseline HRG model. In addition to established mesons and 3-star and 4-star baryon resonances listed by the PDG, we include additional strange and non-strange baryon states predicted by the quark model that are not listed in the PDG tables. Furthermore, 1-star and 2-star baryon resonances as well as mesons included in the PDG data sets listed as not well established are included in the spectrum. The strange meson $K_0^*(700)$ is excluded from this list of hadron states for the reasons mentioned before. The full QMHRG2020 list can be found in [48].

We have compared our continuum extrapolations of second order cumulants with the QMHRG-2020 based calculations in the insets in Figures 5.2 and 5.3. While the agreement between both is generally quite good for low temperatures, the net baryon-number and electric charge correlation χ_{11}^{BQ} and electric charge fluctuations χ_2^Q show significant differences between QCD results and HRG calculations.

Influence of finite volumes on χ_2^Q

The inset for χ_2^Q in Figure 5.3 shows a significant difference between QCD and HRG calculations across the full temperature range that even persists down to $T = 135$ MeV. Due to Boltzmann suppression, the lightest charged hadrons, the pions, are the dominant contribution to electric charge fluctuations in this low temperature regime. These are known to be affected by finite volume effects when $m_\pi \lesssim T$ such that significant differences compared to results in the thermodynamic limit can occur [49]. Throughout all lattice QCD calculations presented in this thesis, we use lattice QCD calculations performed on lattices with fixed aspect ratio $N_\sigma/N_\tau = LT = 4$. The physical extent of our lattices is thus fixed. Therefore, it is more appropriate to compare our QCD results with HRG model calculations that reflect the restriction to a finite volume with $LT = 4$. In order to achieve this, one can investigate the behavior of pion and kaon gasses in a finite cubic volume with periodic boundary conditions as described in [50]. The deviations from results in the thermodynamic limit can then be parametrized via

$$\frac{(\chi_2^Q)_{LT=4}}{(\chi_2^Q)_{LT=\infty}} = \begin{cases} 0.997 - 0.126T/T_{pc,0}\ , & \text{pions} \\ 1.002 - 0.032T/T_{pc,0}\ , & \text{kaons.} \end{cases} \tag{5.3.1}$$

Including these finite-volume corrected contributions for pions and kaons in the QM-HRG model results in a deviation from the thermodynamic limit result according to

$$\frac{(\chi_2^Q)_{LT=4}}{(\chi_2^Q)_{LT=\infty}} = 1.324 - 1.290T/T_{pc,0} + 1.316(T/T_{pc,0})^2 - 0.411(T/T_{pc,0})^3. \tag{5.3.2}$$

Using this parametrization we can compute a finite-volume corrected second order cumulant for electric charge fluctuations $(\chi_2^Q)_{LT=4}$ that we show in Figure 5.3 as a dashed red line. As can be seen from this figure, the agreement between the finite volume corrected HRG result and the QCD result is much better. Discrepancies between the two become visible only beyond $T > 150$ MeV and at $T_{pc,0}$ the lattice QCD result are about 5% smaller then the finite volume corrected QMHRG calculation.

χ_{11}^{QS} and the role of $K_0^*(700)$

As we have discussed earlier, the kaon resonance $K_0^*(700)$, although being listed as a well-established resonance by the PDG, is not included in the QMHRG2020 spectrum as it has been suggested by S-matrix based analyses that its contribution to thermodynamics of strongly interacting matter is significantly suppressed.

In the middle plot of Figure 5.2, we show the correlation between electric charge fluctuation and strangeness χ_{11}^{QS}. As can be seen in the inset of this plot, the agreement between the QCD result and the QMHRG2020 calculation not including the $K_0^*(700)$ resonance is quite good even well beyond the pseudo-critical transition temperature $T_{pc,0}$. The dominant contribution to this correlation is given by kaons. In HRG model calculations, the ground state kaon and its P-wave excitation $K^*(892)$ contribute more then 80% to this correlation with the remaining contributions coming from heavier strange mesons and baryons. In Figure 5.4, we show the effect of adding the $K_0^*(700)$ resonance to the HRG models. Adding this resonance increases the second order cumulant χ_{11}^{QS} by about 10% and spoils the agreement between QCD results and HRG calculations across the entire temperature range considered by us. Also included in this figure are the S-matrix calculations from [47], which we combine with the contributions from the QMHRG2020 spectrum not considered in that analysis. The comparison of HRG calculations to lattice QCD results indicates, just like the S-matrix analysis has suggested, that the contribution of the $K_0^*(700)$ resonance to thermodynamics of strongly interacting matter is significantly overestimated if it is included in HRG model calculations based on point-like, non-interacting hadrons and resonances only and should therefore not be included in such.

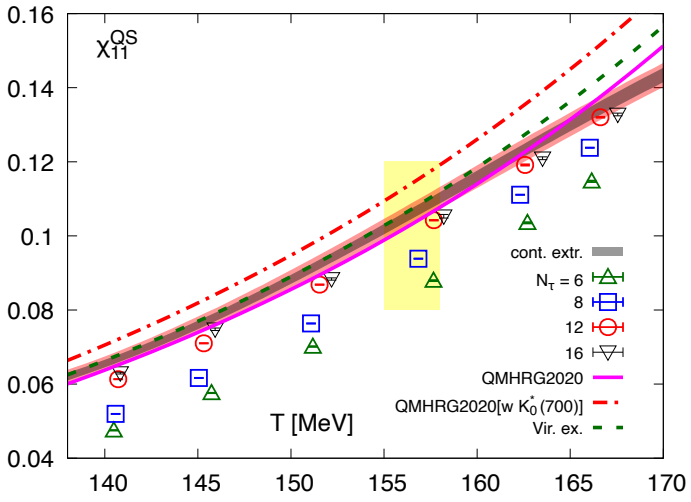

Figure 5.4: Comparison of QCD results for χ_{11}^{QS} with HRG model calculations. The red dashed-dotted line shows the effect of including the resonance $K_0^*(700)$ in the QMHRG2020 spectrum, whereas the green dotted line shows the S-matrix analysis supplemented with states present in the QMHRG2020 list that were not included in the analysis.

Fluctuations and correlations of net baryon-number

Comparing the correlations of baryon-number and strangeness, as well as baryon-number and electric charge, as shown in Figure 5.5 with HRG calculations based on different hadron lists, one can see that baryon-strangeness correlations χ_{11}^{BS} are particularly sensitive to the strange baryon content of the considered hadron spectrum while χ_{11}^{BQ} exhibits only a very mild dependece on additional baryon resonances. The inclusion of additional resonances absent in the PDGHRG model results in an increase of about 30% of $|\chi_{11}^{BS}|$. These models are consistent with lattice QCD calculations up to about $T_{pc,0}$, while the PDGHRG shows a sizable difference from lattice QCD results across the full temperature range. For the baryon-charge correlation χ_{11}^{BQ}, deviations between HRG calculations and the lattice QCD results appear already around $T \sim 145$MeV and keep growing as the temperature is increased. At the pseudo-critical transition temperature $T_{pc,0}$, the HRG results are about 20% larger and a change in the hadronic spectrum hardly affects this mismatch.

For net-baryon fluctuations χ_2^B which can be obtained from the two correlations above via equation (5.2.2), this discrepancy translates to a difference between HRG calculations and lattice QCD results at $T_{pc,0}$ of about 10%.

As changes to the hadron spectrum cannot resolve the discrepancy found in the comparison of χ_{11}^{BQ}, extensions to the HRG model with point-like, non-interacting resonances have been attempted. The inclusion of repulsive interactions by ascribing a finite volume to hadrons, resulting in the EVHRG model, has been studied in [51][52][53] and generally leads to a suppression of the magnitude of second order cumulants involving net baryon-number fluctuations. While this would be helpful for the description of the baryon-charge correlation χ_{11}^{BQ}, it would invariably harm the agreement of HRG models with point-like, non-interacting resonances and QCD for χ_{11}^{BS}. While χ_{11}^{BQ} would favor larger excluded volumes, χ_{11}^{BS} would favor the opposite.

We can quantify this fact further and compute the values of the excluded volume parameter b for which the EVHRG model results would be consistent with QCD. To do so, we note that the ratio of second order cumulants involving net baryon-number fluctuations from EVHRG and HRG models is, according to [53], given by

$$R_B^{EV} = \frac{(\chi_{11}^{BQ})_{\mathrm{EVHRG}}}{(\chi_{11}^{BQ})_{\mathrm{HRG}}} = \frac{(\chi_{11}^{BS})_{\mathrm{EVHRG}}}{(\chi_{11}^{BS})_{\mathrm{HRG}}} = \frac{(\chi_2^{B})_{\mathrm{EVHRG}}}{(\chi_2^{B})_{\mathrm{HRG}}} = 1 - 2\frac{b}{T} P_B^{\mathrm{HRG}}(T) + \mathcal{O}(b^2). \tag{5.3.3}$$

Here, $P_B^{\mathrm{HRG}}(T)$ denotes the contribution of baryons and anti-baryons to the pressure. We can rewrite this to obtain an expression for the largest (smallest) excluded

volume parameter b^+ (b^-) that leads to consistency between EVHRG model calculations and QCD results. Denoting the combined statistical and systematic error of χ_{11}^{BX} with Δ_X where $X = Q, S$ and using the relation $P_B/T^4 = \chi_2^B$, one finds

$$b^{\pm} = \frac{1}{2T^3(\chi_2^B)_{\rm HRG}} \left(1 - \frac{(\chi_{11}^{BX} \pm \Delta_X)_{\rm QCD}}{(\chi_{11}^{BX})_{\rm HRG}}\right). \tag{5.3.4}$$

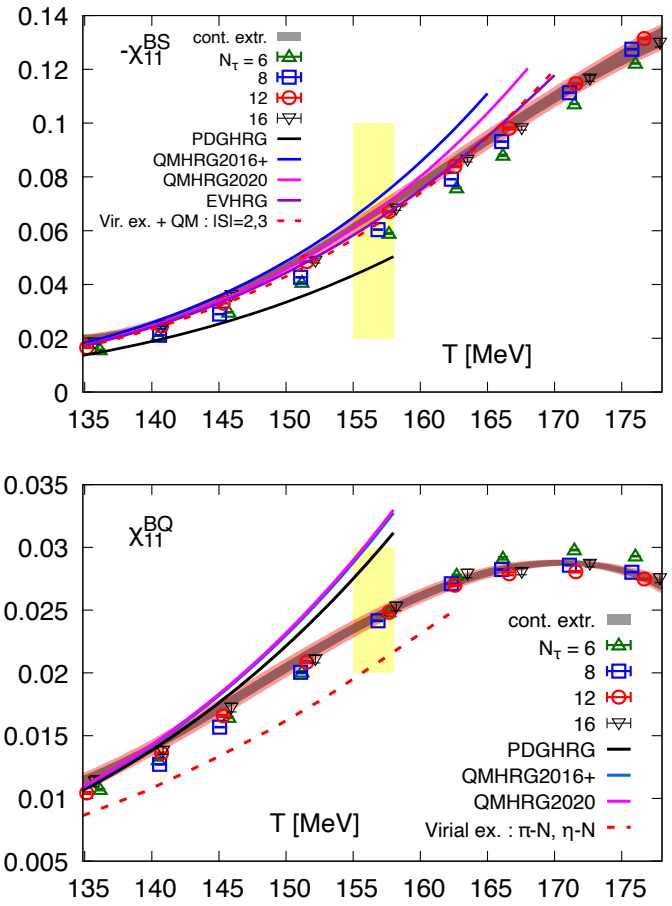

Figure 5.5: Comparison of continuum extrapolated lattice QCD results for baryon-strangeness (χ_{11}^{BS}) and baryon-charge (χ_{11}^{BQ}) correlations to different HRG models. Results from excluded volume HRG models with $b = 1$fm as well as virial expansions [47] are included as well.

At temperatures around the pseudo-critical transition line $T_{pc,0}$, specifically for $T = (150 - 155)$ MeV, we find that the excluded volume parameter b should be less or equal to 0.4 fm^3 in order to have consistency between QCD results and

EVHRG calculations of χ_{11}^{BS}. In the case of χ_{11}^{BQ}, however, we find that b should be in the interval $1\ \mathrm{fm}^3 \leq b \leq 2\mathrm{fm}^3$, significantly larger than in the case of baryon-strangeness correlations.

The temperature derivative of χ_{11}^{BQ} is shown in Figure 5.6 together with EVHRG results at various values of b. In order to obtain a good agreement between these and the QCD results, excluded volume factors larger then $2\ \mathrm{fm}^3$ would be needed.

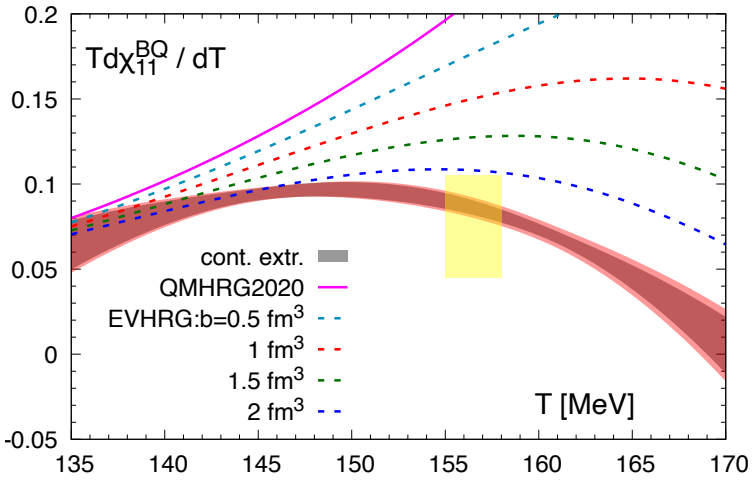

Figure 5.6: Temperature derivative of the continuum extrapolated baryon-charge fluctuation χ_{11}^{BQ} calculated in QCD (bands) and in EVHRG calculations with various excluded volume parameters b (lines).

As seen in equation (5.3.3), excluded volume corrections to the three second order cumulants involving baryon-number fluctuations are identical. In order to resolve discrepancies between QCD results and HRG calculations that cannot be explained by such corrections, one may form ratios of any two of those second order cumulants. Excluded volume corrections are canceled in such a ratio and the remaining discrepancies must have another origin. Due to (5.2.2), it suffices to investigate only one of such ratios as all the other can be obtained from this equation. Here, we focus on the ratio $\chi_{11}^{BQ}/\chi_{11}^{BS}$ which we show in Figure 5.7.

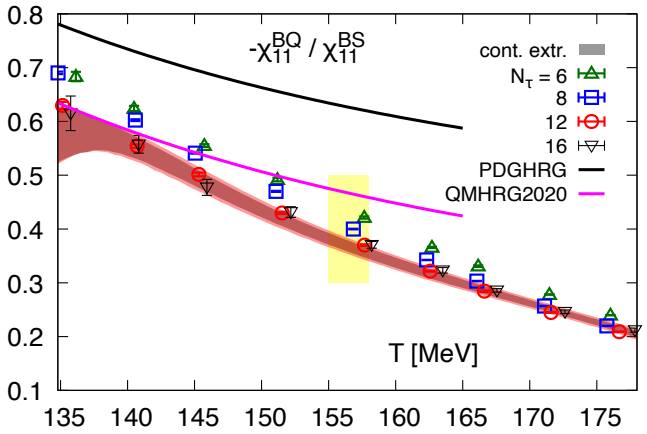

Figure 5.7: Continuum extrapolation of $\chi_{11}^{BQ}/\chi_{11}^{BS}$ compared to PDG-HRG and QM-HRG models.

Significant deviations between HRG calculations and lattice QCD results, that cannot be explained through a single excluded volume parameter b, become visible at temperature $T \sim 145$ MeV which is, of course, due to χ_{11}^{BQ} calculated from HRG models deviating from lattice QCD results while χ_{11}^{BS} does not show such a discrepancy. An analysis of the second order virial coefficient using the S-matrix approach carried out in [54] arrived at a similar conclusion. There, the authors point out that various quantum number channels contributing to the partial-wave analysis of the second virial expansion coefficient are affected differently by repulsive interactions. In EVHRG models, however, these subtleties are missed.

Figure 5.8 shows a comparison between lattice QCD results for χ_{11}^{BQ} and χ_{11}^{BS} with QMHRG calculations and results from second order virial expansions. The second virial coefficient for χ_{11}^{BS} has been calculated in [55] using a unitary, multi-channel analysis [56][57] and the result is shown in the left plot of Figure 5.8. Up until about $T = 160$ MeV, the virial expansion result agrees with lattice QCD to about 10% and behaves quite similar to the QMHRG result but does not improve over it. In the right plot, we show a comparison to an S-matrix based calculation of χ_{11}^{BQ} that includes contributions from elastic πN scatterings as well as inelastic $\pi N \to \eta N$ interactions. We can see a discrepancy between QCD results and this calculation at low temperatures that is about a factor two larger compared to the S-matrix based calculations shown for χ_{11}^{BS}. Therefore, a calculation based on the two included interactions is not sufficient to yield a satisfactory agreement with QCD calculations.

While the S-matrix approach to calculating the partition function in a virial expansion is in principle able to capture the intricate interplay between the different types of interactions occurring in strong interaction matter without relying

on specific spectra of resonances, it relies on experimental information on scattering phase shifts which is often insufficiently available. At higher densities, experimentally even less constrained multi-particle interactions have to be taken into account such that additional approximations are often needed. With currently available data, the S-matrix approach therefore does not yield an adequate description of QCD results for correlations of baryon-number and electric charge fluctuations while also not providing a significant improvement over QMHRG calculations of χ_{11}^{BS}.

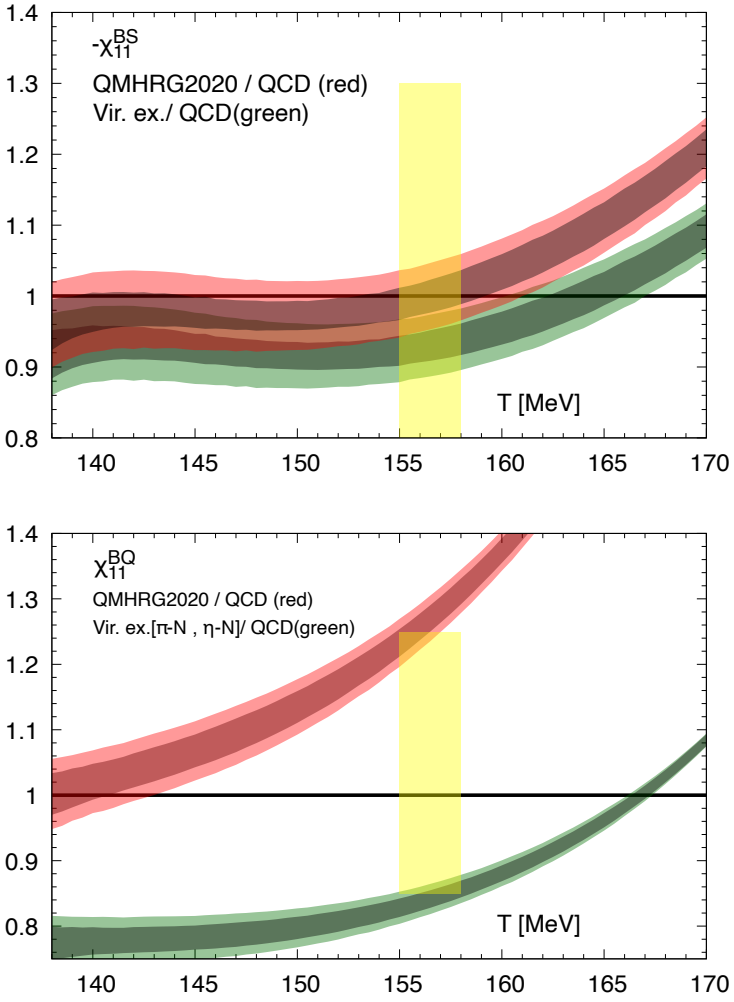

Figure 5.8: Ratios of continuum extrapolated lattice QCD results and QMHRG models (red) as well as results based on calculations of the second virial coefficient (green). The left figure shows χ_{11}^{BQ}, while χ_{11}^{BQ} is shown in the right figure.

Chapter 6

Baryon number fluctuations

Cumulant ratios of net baryon-number fluctuations serve as popular probes to search for the elusive critical endpoint in the QCD phase diagram. As they couple to the order parameter of the chiral transition, they diverge at the critical point and are expected to show remnants of the critical behavior in its vicinity. Such remnants of critical behavior are also expected to be found in fluctuations of net proton-number fluctuations, used as a proxy for net baryon-number fluctuations, which are studied intensively in heavy ion collision experiments at RHIC. In this chapter, we compute lattice QCD predictions for higher order cumulant ratios of baryon-number fluctuations and compare them to corresponding measurements performed by the STAR collaboration. This chapter is based on our publication [58].

6.1 Mean and variance of net baryon-number fluctuations

We have calculated the mean to variance ratio of net baryon-number fluctuations

$$R_{12}^B(T,\mu_B) = \frac{M_B}{\sigma_B^2} = \frac{\chi_1^B(T,\mu_B)}{\chi_2^B(T,\mu_B)}, \tag{6.1.1}$$

using the Taylor expansion method described in section 4 with coefficients up to eight order for strangeness neutral systems $n_S = 0$ and a ratio of electric charge to baryon density $n_Q/n_B = 0.4$ that reflects the conditions found in heavy ion collisions. We have included data from lattices with temporal extents $N_\tau = 8, 12$. Lattices with temporal extent $N_\tau = 16$ were not included in this analysis as baryon number fluctuations are considerably more noisy and thus require significantly larger statistics than currently available to us.

Expansions of $\chi_1^B(T,\mu_B)$ and $\chi_2^B(T,\mu_B)$ are computed according to (4.1.9) up to $\mathcal{O}(\hat{\mu}_B^7)$ and $\mathcal{O}(\hat{\mu}_B^6)$, respectively. In order to properly take into account correlations between all expansion coefficients, we evaluate the full expression (6.1.1) using the jackknife method [59] for chemical potentials in the interval $\mu_B/T \in [0,2]$ with stepsize $\delta_{\mu_B} = 0.01$. We truncate the series for $\chi_1^B(T,\mu_B)$ at order $l_{\max}$ and that for $\chi_2^B(T,\mu_B)$ at order $k_{\max} = l_{\max} - 1$ and show the result of leading order (LO) $[l_{\max} = 1, k_{\max} = 0]$, next-to-leading order (NLO) $[3,2]$, etc. up to NNNLO $[7,6]$ in Figure 6.1. Across the entire temperature range analyzed by us, cutoff effects remain negligible up to chemical potentials of about $\mu_B/T = 1$ and stay comparable to statistical errors of $N_\tau = 12$ results up to $\mu_B/T = 1.2$. In order to obtain a continuum estimate, we fit the data with a polynomial fraction ansatz

$$f(T,\hat{\mu}_B) = \frac{\sum_{n=0}^{n_{\max x}} a_n(\hat{\mu}_B)\bar{T}^n}{\sum_{m=0}^{m_{\max}} b_m(\hat{\mu}_B)\hat{T}^m}, \quad \text{with} \quad \bar{T} = \frac{T}{T_0}, \tag{6.1.2}$$

were T_0 is an arbitrary scale. The chemical potential dependency of the coefficients is parameterized with a simple quadratic polynomial

$$a_n(\hat{\mu}_B) = a_{n,0} + a_{n,2}\hat{\mu}_B^2, \tag{6.1.3}$$

$$b_n(\hat{\mu}_B) = b_{n,0} + b_{n,2}\hat{\mu}_B^2. \tag{6.1.4}$$

The approach towards the continuum is parameterized by including $1/N_\tau^2$ corrections, i.e.

$$f(T,\hat{\mu}_B) = h(T,\hat{\mu}_B) + \frac{1}{N_\tau^2} g(T,\hat{\mu}_B), \tag{6.1.5}$$

where $h(T,\hat{\mu}_B)$ and $g(T,\hat{\mu}_B)$ are polynomial fractions as given in (6.1.2).

For R_{12}^B, we find it sufficient to use polynomial fractions of order [2,3] in both terms of the fit ansatz due to the weak temperature dependence and nearly linear dependence on chemical potential. The resulting continuum extrapolation is shown for various temperatures in Figure 6.2. As is clearly visible from the figure, variations of R_{12}^B with temperature are very small in the considered range. Furthermore, the precision on the continuum estimate is mostly determined by statistical uncertainties as the convergence of the Taylor series, seen in Figure 6.1, is quite good. As we will discuss in more detail in a later section, for chemical potentials $\mu_B < 125$ MeV, the lattice QCD results agree quite well with hadron resonance gas model calculations but beyond 125 MeV, the hadron resonance gas calculation underestimates the QCD result, indicating large deviations of higher order baryon number fluctuations at $\mu_B = 0$ calculated in the HRG model compared to lattice QCD results.

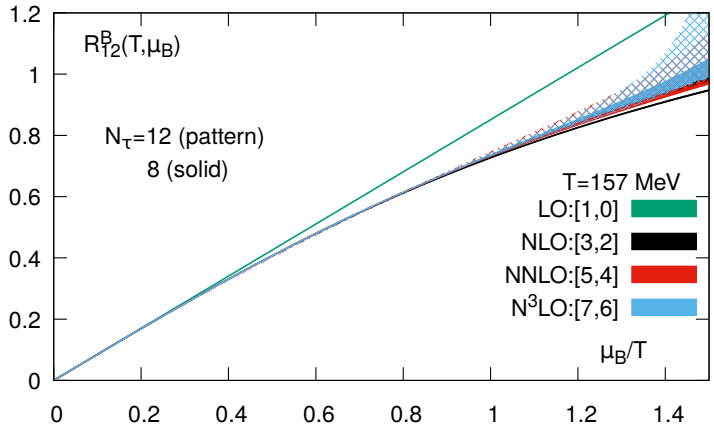

Figure 6.1: Cut-off dependence of the Taylor expansion for $R^B_{12}(T, \mu_B)$ at $T \sim 157$ MeV. Results from lattices with temporal extent $N_\tau = 8$ are shown as solid bands while those from lattices with $N_\tau = 12$ are shown as pattern filled bands.

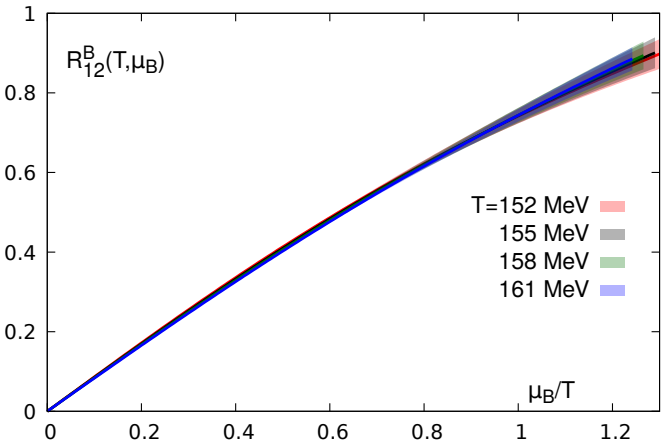

Figure 6.2: Continuum estimate of $R^B_{12}(T, \mu_B)$ based on NNNLO Taylor expansions obtained on lattices with $N_\tau = 8, 12$.

6.2 Skewness and kurtosis of net baryon-number fluctuations

For higher order baryon number fluctuations, the agreement between HRG calculations and lattice QCD results seen in the mean-to-variance ratio no longer

persists. The skewness and kurtosis ratios

$$R^B_{31}(T,\mu_B) = \frac{S_B\sigma^3_B}{M_B} = \frac{\chi^B_3(T,\mu_B)}{\chi^B_1(T,\mu_B)}, \tag{6.2.1}$$

$$R^B_{42}(T,\mu_B) = \kappa_B\sigma^2_B = \frac{\chi^B_4(T,\mu_B)}{\chi^B_2(T,\mu_B)}, \tag{6.2.2}$$

are always unity in HRG calculations as one can see from equation (5.1.4). Since $|B|$ is either 0 or 1, the terms appearing in ratios of two diagonal baryon-number susceptibilities calculated via (5.1.4) always cancel each other. In lattice QCD calculations, however, the skewness and kurtosis ratios are known to deviate significantly from unity. In contrast to the mean-to-variance ratio, R^B_{31} and R^B_{42} show furthermore a significantly stronger temperature dependence but are rather insensitive to changes in chemical potential.

Using our data for generalized susceptibilities of up to eighth order, we constructed NNLO expansions of $\chi^B_3(T,\mu_B)$ and $\chi^B_4(T,\mu_B)$ for strangeness neutral systems with $n_S = 0$ and $n_Q/n_B = 0.4$ and use them together with the expansions of first and second order cumulants to form the two ratios $R^B_{31}(T,\mu_B)$ and $R^B_{42}(T,\mu_B)$. In Figure 6.3, we show the results obtained on lattices with temporal extent $N_\tau = 8$ for different truncations $[l_{\max}, l_{\max}]$ of these expansions. The leading order result, which is a constant in μ_B/T is shown only for $T = 152$ MeV as the NLO and NNLO results of course agree with it at $\mu_B = 0$. The lower three temperature values chosen here reflect the range of temperatures that $T_{pc}(\mu_B)$ assumes across the μ_B/T range displayed. The lowest temperature $T = 152$ MeV corresponds to the value $T_{pc}(\mu_B)$ assumes at $\mu_B/T = 1$, whereas $T = 155$ MeV and $T = 158$ MeV correspond to the lower and upper end of the error band on $T_{pc}(\mu_B = 0)$, respectively. As we can see from the figure, the effect of higher order corrections is more significant for the skewness and kurtosis ratios than they are in the case of the ratio of mean and variance. The difference between NLO and NNLO expansions of χ^B_3 is about 5% at $\mu_B/T = 0.8$ and grows to 10% at $\mu_B/T = 1$. At $\mu_B = 0$, the skewness and kurtosis ratio agree with each other to about 1% to 2%. However, NLO corrections to the kurtosis ratio are about a factor 3 larger than that of R^B_{31}. Similarly, the NNLO corrections to the NLO result are also larger for R^B_{42}.

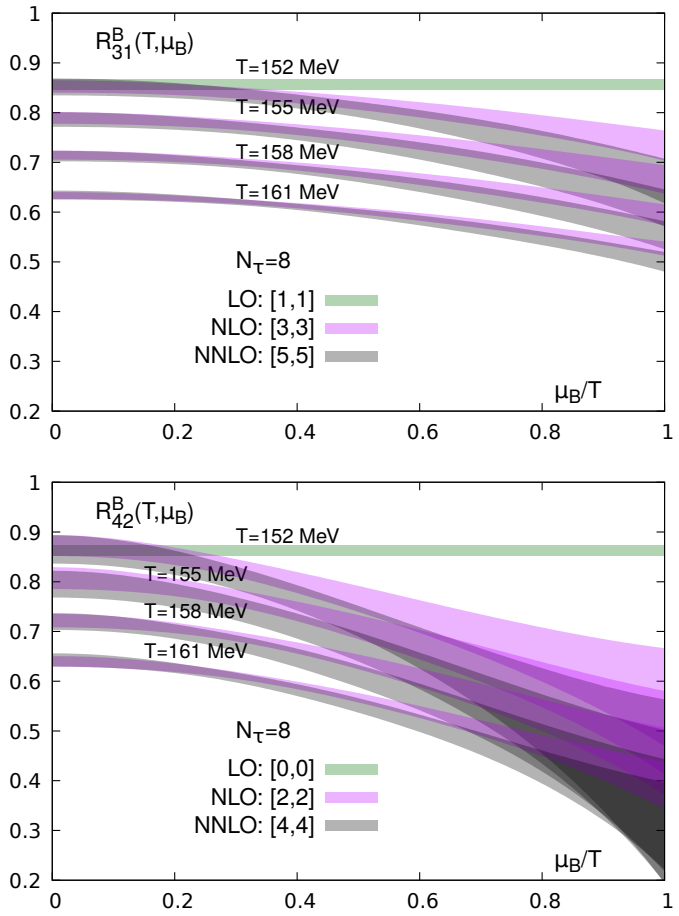

Figure 6.3: The cumulant ratios $R^B_{31}(T,\mu_B) = S_B\sigma^3_B/M_B$ and $R^B_{42}(T,\mu_B) = \kappa_B\sigma^2_B$ calculated to LO, NLO and NNLO in $\hat{\mu}_B$ as functions of μ_B/T for temperatures in the vicinity of $T_{pc,0}$.

These results agree well with earlier studies of higher order cumulants of baryon-number fluctuations [60] that found R^B_{31} and R^B_{42} to be almost identical at leading order while NLO corrections for R^B_{42} were found to be a factor three larger than those for R^B_{31}. In Figure 6.4, we show that this relationship still holds for NNLO corrections of the two ratios. The inset of the figure shows the second derivative of the skewness with respect to μ_B/T as well as one third of the same derivative of the kurtosis ratio. In Figure 6.5, we show the continuum estimate of the two ratios at $\mu_B = 0$ that is obtained from jointly fitting the $N_\tau = 8, 12$ data with the ansatz given in equation (6.1.5). Due to the statistical uncertainties on the $N_\tau = 12$ data set, we are unable to resolve any temperature or chemical potential dependence of cutoff effects and therefore use $g(T,\mu_B) = a_{0,0}$ together with a [3,4] polynomial fraction for $f(T,\mu_B)$. In the inset of the R^B_{42} plot, we also show

the difference $R^B_{42} - R^B_{31}$ at vanishing chemical potential. The chemical potential dependence of the continuum estimates are shown in Figure 6.6.

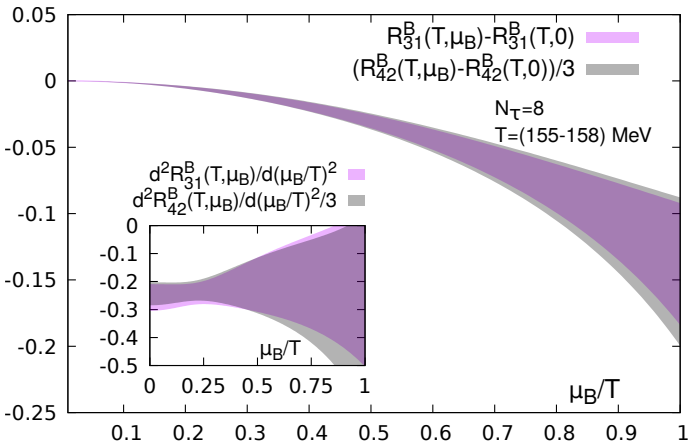

Figure 6.4: Chemical potential dependence of the higher order corrections to R^B_{31} and one third of the corrections to R^B_{42} calculated on lattices with $N_\tau = 8$. The inset shows the second derivative with respect to μ_B/T of these quantities.

6.3 Fifth and sixth order cumulants of net baryon-number fluctuations

In this section, we present results on cumulant ratios including fifth and sixth order cumulants of net baryon-number fluctuations which are related to the so-called hyper-skewness S^H and hyper-kurtosis κ^H

$$R^B_{51}(T,\mu_B) = \frac{S^H_B \sigma^5_B}{M_B} = \frac{\chi^B_5(T,\mu_B)}{\chi^B_1(T,\mu_B)}, \tag{6.3.1}$$

$$R^B_{62}(T,\mu_B) = \kappa^H_B \sigma^4_B = \frac{\chi^B_6(T,\mu_B)}{\chi^B_2(T,\mu_B)}. \tag{6.3.2}$$

With our eighth order Taylor coefficients, we can calculate up to NLO expansions of $\chi^B_5(T,\mu_B)$ and $\chi^B_6(T,\mu_B)$. However, as the orders of the cumulants are increased, the signal-to-noise ratio grows dramatically and for fifth and sixth order cumulants, only the $N_\tau = 8$ data set contains enough configurations to obtain results with reasonable statistical errors. Therefore, we will not perform continuum estimations as we have done for the mean-to-variance and skewness and kurtosis ratios. As before, we show the results of R^B_{51} and R^B_{62} obtained from leading

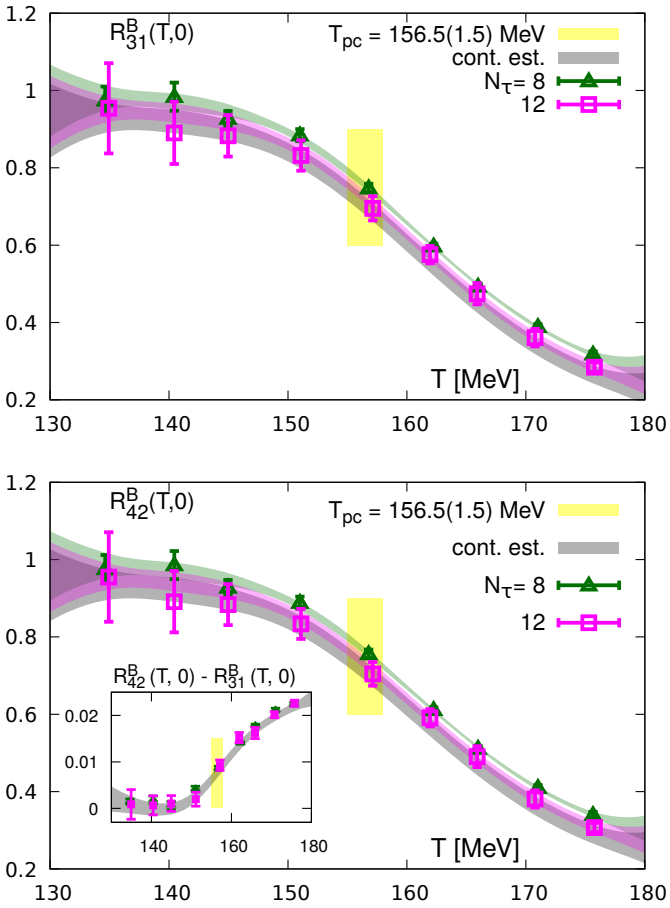

Figure 6.5: Continuum estimates of R^B_{31} (left) and R^B_{42} (right) evaluated at $\mu_B = 0$. The inset on the right shows the difference between both ratios.

order and next-to-leading order calculations in the vicinity of T_{pc} as a function of μ_B/T in Figure 6.7. Similar to the skewness and kurtosis ratios, R^B_{51} and R^B_{62} are in very good agreement with each other at $\mu_B = 0$. Unlike those, however, both fifth and sixth order ratios are negative at $\mu_B = 0$, which is in striking difference to HRG model calculations where this ratio is always very close to unity. Next-to-leading order corrections to both quantities are also negative and the corrections to R^B_{62} are again about a factor 3 larger than those for R^B_{51} which is a consequence of the structure of the Taylor expansion of even and odd order cumulants for $n_Q = n_S = 0$ which are only slightly modified for strangeness neutral systems with $n_Q/n_B = 0.4$.

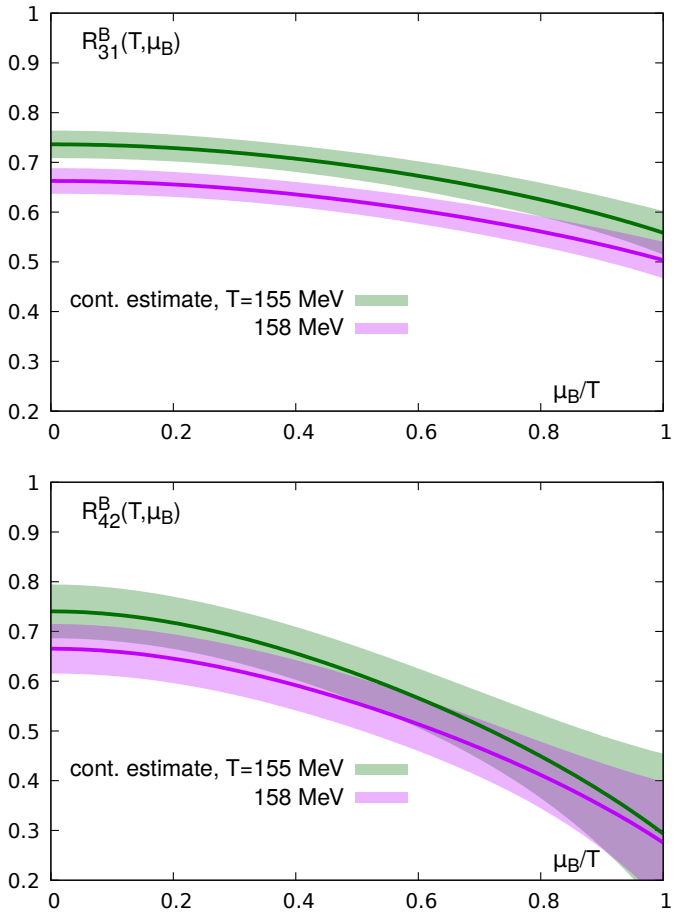

Figure 6.6: μ_B-dependence of the continuum estimate of skewness (left) and kurtosis ratios (right).

6.4 Net proton-number fluctuations and baryon number fluctuations on the pseudo-critical line

Finally, we want to compare our results for net-baryon number fluctuations with results on higher order cumulants of proton number fluctuations measured by the the STAR Collaboration during the first phase of the Beam Energy Scan program at RHIC. For this purpose, we evaluate the cumulant ratios of net baryon-number fluctuations on the pseudo-critical line $T_{pc}(\mu_B)$ parameterized by

$$T_{\rm pc}(\mu_B) = T_{pc,0}\left(1 - \kappa_2^{B,f}\left(\frac{\mu_B}{T_{pc,0}}\right)^2\right), \tag{6.4.1}$$

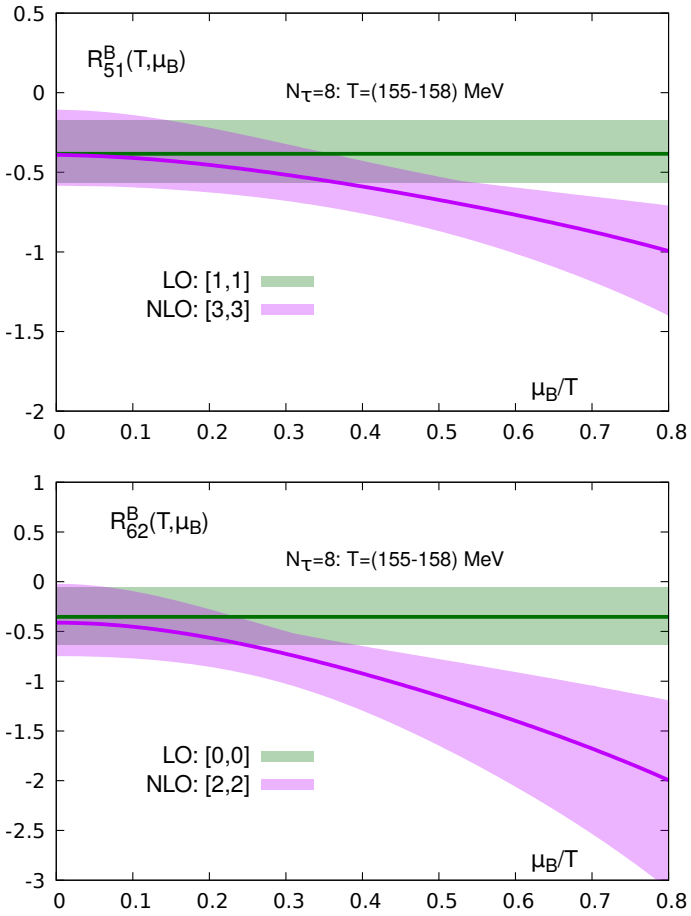

Figure 6.7: Leading order and next-to-leading order calculations of the cumulant ratios $R^B_{51}(T,\mu_B)$ and $R^B_{62}(T,\mu_B)$ as a function of μ_B/T calculated on lattices with temporal extent $N_\tau = 8$.

with $T_{pc,0} = 156.5(1.5)$ MeV and $\kappa_2^{B,f} = 0.012(4)$ as determined in [9]. The fourth order correction $\kappa_4^{B,f}$ vanishes within errors. The result for the mean-to-variance ratio $R^B_{12}(T_{pc}(\mu_B),\mu_B)$ evaluated on the pseudo-critical line is shown in Figure 6.8 together with HRG calculations. As we can see, both agree quite well up to chemical potentials of about $\mu_B = 125$ MeV. Beyond this point, the HRG calculation underestimates the QCD result and the difference between both grows with increasing chemical potential. At $\mu_B = 200$ MeV, it amounts to about 15%. A determination of freeze-out parameters in heavy-ion collision experiments on the basis of low order cumulants obtained in HRG calculations, such as the statistical hadronization model approach [43], may therefore be appropriate for small values of baryon chemical potentials. Based on such parameterizations of the

freeze-out curve, this translates to an applicability of these methods to beam energies $\sqrt{s}_{NN} \gtrsim 27$ GeV. Our results suggest that below this beam energy, HRG based determinations of freeze-out parameters might differ from what would be obtained in QCD by more than 10%. In order to avoid the problems associated with agreeing on certain chemical potentials at given beam energies when discussing results on higher order cumulants, we replace the baryon chemical potential in favor of R^B_{12}. At least in the parameter region explored here, this is valid as R^B_{12} is a monotonically rising function. In the vicinity of the critical point, this will break down as the variance σ^2_B will diverge such that R^B_{12} would approach zero.

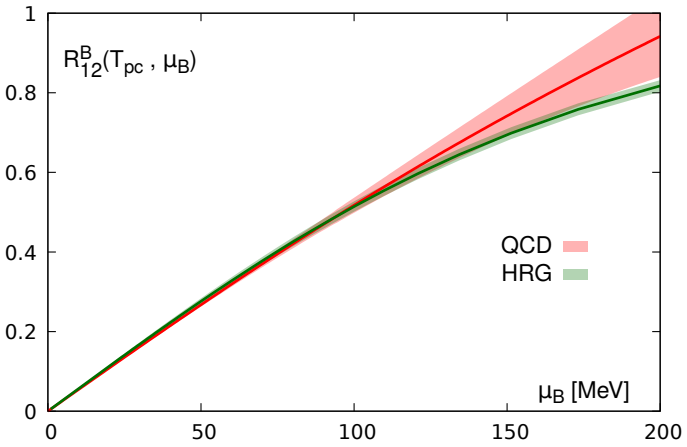

Figure 6.8: The mean-to-variance ratio $R^B_{12}(T, \mu_B)$ evaluated on the pseudo-critical transition line $T_{pc}(\mu_B)$ compared to HRG model calculations. The width of the HRG band reflects the discrepancy between PDG-HRG and QM-HRG results.

In Figure 6.9 we show the results for the skewness and kurtosis ratios R^B_{31} and R^B_{42} evaluated on the pseudo-critical transition line $T_{pc}(\mu_B)$ as a function of the corresponding R^B_{12} value up to $R^B_{12} = 0.75$, which is equivalent to $\mu_B/T = 1$. The error bands include the uncertainty on the determination of the pseudo-critical transition line as well as statistical errors on the NNLO determination of the cumulant ratios and the continuum estimation. Furthermore, the corresponding net-proton number fluctuations, taken as a proxy for net baryon-number fluctuations, obtained by STAR during the BES-I program [61] are shown for beam energies $200 \text{ MeV} \geq \sqrt{s}_{NN} \geq 27 \text{ MeV}$ and plotted as a function of the associated mean-to-variance ratio of net proton-number fluctuations R^P_{12}. Qualitatively, measured net-proton skewness and kurtosis ratios agree with the lattice QCD calculations of R^B_{31} and R^B_{42}. Both decrease mildly with $R^{P/B}_{12}$ and the curvature of the kurtosis ratio is larger than that of the skewness ratio. R^P_{31} is slightly larger than the lat-

tice QCD result evaluated on the pseudo-critical transition line which is consistent with freeze-out occurring slightly below T_{pc}. The kurtosis ratio R^P_{42} is consistent with this finding, however the statistical uncertainties on its experimental determination are much larger.

Note, however, that such direct comparisons of event-by-event fluctuations measured in heavy ion collision experiments and fluctuations of QCD in thermal equilibrium face certain caveats. Unlike the net baryon-number, the net proton-number is not conserved and fluctuations of the latter may change even after chemical freeze-out [62]. Furthermore, the extent to which event-by-event fluctuations measured in a sub-volume of the fireball deviate, due to global conservation laws, from a true grand-canonical ensemble needs to be accounted for [63][64]. Further aspects of such comparisons are discussed in [65]. Therefore, these direct comparisons should be treated only as a rough, first step towards a more sofisticated analysis that takes these issues into consideration.

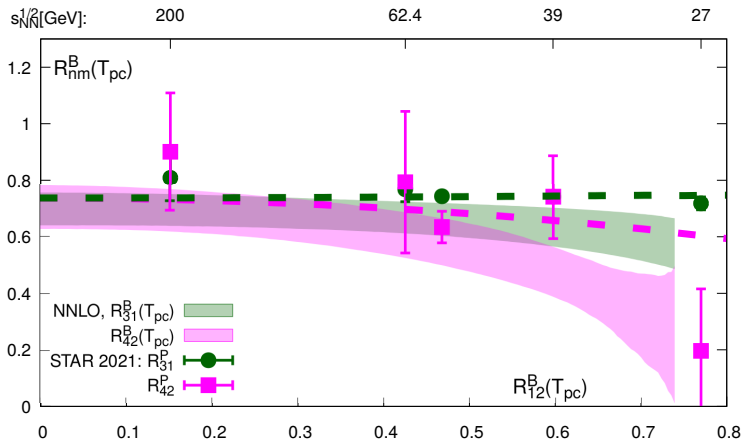

Figure 6.9: Continuum estimations of skewness and kurtosis ratios $R^B_{31} = S_B\sigma^3_B/M_B$ and $R^B_{42} = \kappa_B\sigma^2_B$ evaluated on the pseudo-critical transition line $T_{pc}(\mu_B)$ and shown as a function of the corresponding R^B_{12} value. Colored data points show corresponding results on ratios of net-proton number fluctuations obtained by the STAR collaboration [61]. The dashed lines show joint fits to the STAR data.

In Figure 6.10, we show the NLO calculations of hyper-skewness and hyper-kurtosis ratios R^B_{51} and R^B_{62} evaluated on the pseudo-critical transition line as well as results on sixth order cumulants ratios measured by the STAR collaboration [66]. The data is again shown as a function of $R^{B/P}_{12}$. As we have mentioned earlier when discussing Figure 6.7, both hyper-skewness and hyper-kurtosis ratios are negative already at $\mu_B = 0$ and decrease further as the chemical potential, or equivalently R^B_{12} grows. In an earlier comparison of these quantities based on

preliminary data of the STAR collaboration [58], the experimentally measured R_{62}^P clearly disagreed with lattice QCD calculations on the pseudo-critical transition line and it seemed improbable that one would be able to describe the negative R_{62}^P result at $\sqrt{s}_{NN} = 200$ GeV and positive R_{62}^P result at $\sqrt{s}_{NN} = 54.4$ GeV simultaneously with QCD in thermal equilibrium. Now, updated results on R_{62}^P [66] exhibit statistical uncertainties so large that such a definite statement cannot be made anymore. Furthermore, the results on R_{62}^P now overlap with $R_{62}^P = 0$ within errors. Therefore, more precise experimental results on R_{62}^P as well as lattice QCD calculations of higher order contributions to R_{62}^B are necessary in order to determine whether or not results on hyperkurtosis are thermodynamically consistent.

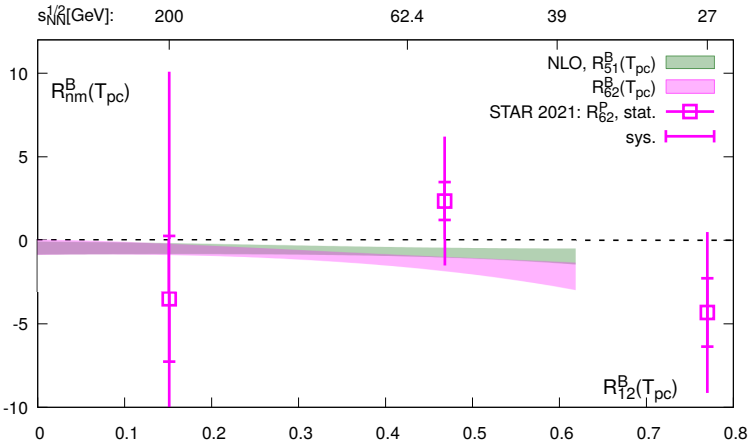

Figure 6.10: Hyper-skewness and hyper-kurtosis ratios R_{51}^B and R_{62}^B evaluated on the pseudo-critical transition line based on calculations on lattices with temporal extent $N_\tau = 8$. Colored data points show results obtained by the STAR collaboration [66].

Chapter 7

Electric charge and strangeness fluctuations

Studies of baryon number and strangeness fluctuations in heavy-ion collisions experiments often rely on measuring fluctuations of associated proxy particle species. Proton number fluctuations, for example, typically serve as a proxy for baryon number fluctuations because neutral baryons are significantly harder to detect in these experiments. This makes comparisons to lattice QCD calculations difficult as proton number fluctuations are not observables of lattice QCD, i.e. they cannot be derived from the lattice QCD partition function. This proxy problem is mostly absent in the case of electric charge fluctuations such that comparisons of heavy-ion collision experiment results with lattice QCD are appealing. In this chapter, we present lattice QCD calculations of higher order cumulant ratios of these electric charge fluctuations and compare them, to the extent that it is possible, to results from heavy-ion collision experiments obtained by the STAR and PHENIX collaborations. Furthermore, we comment on strangeness fluctuations and how they can be used to constrain the strangeness chemical potential $\mu_{S,f}$ at freeze-out.

7.1 Mean-to-variance ratio R_{12}^Q

In order to obtain a continuum extrapolated prediction for the mean to variance ratio $M_Q/\sigma_Q^2 = R_{12}^Q = \chi_1^Q/\chi_2^Q$, we compute jackknife estimates of (4.1.10) in a μ_B interval $\mu_B/T \in [0, 2]$ with a stepsize of $\delta_{\mu_B} = 0.01$ for each of the temperatures and three lattice sizes listed in 3.2. The maximum orders $k_{\max}$ and $l_{\max}$ of the numerator and denominator in (4.1.10) have been chosen such that contributions of generalized susceptibilities $\chi_{ijk}^{BQS}(T)$ up to eighth order $i + j + k \leq 8$ are included which corresponds to NNNLO Taylor expansions in μ_B. This jackknife

analysis produces nine "slices" of data for each lattice size that outline a surface in the (T, μ_B)-plane. Figure 7.1 shows the result of this procedure for the lattice size $32^3 \times 8$ in the T, μ_B-plane.

For most temperatures, the computed mean-to-variance ratio shows a nearly perfect linear μ_B dependence. For temperatures $T > 156$ MeV, the slope of the surface traced out by the data remains mostly constant and then starts to decrease gradually as the temperature is lowered below $T \simeq 156$ MeV. Furthermore, a negative curvature starts to build up and modifies the linear μ_B dependence in the higher baryon chemical potential region for $T < 156$ MeV.

Since the data describes mostly flat, tilted surfaces, we fit the three resulting surfaces jointly with a low order polynomial ansatz where the coefficients carry an additional $1/N_\tau^2$ correction term to parameterize the approach towards the continuum,

$$R^Q_{12,\mathrm{fit}}(T, \mu_B, N_\tau) = f_1(T, N_\tau)\frac{\mu_B}{T} + f_2(T, N_\tau)\frac{\mu_B}{T}^3 + f_3(T, N_\tau)\frac{\mu_B}{T}^5, \quad (7.1.1)$$
$$f_i(T, N_\tau) = \delta_{i,1} f_0^{(i)} + f_1^{(i)} T + f_2^{(i)} T^3, \;\; \text{with} \;\; f_j^i = f_{j,0}^{(i)} + f_{j,1}^{(i)} \frac{1}{N_\tau^2}.$$

Finally, we evaluate the polynomial fit along the crossover line of the chiral transition given in (6.4.1).

In Figure 7.2, the continuum extrapolated lattice QCD prediction of $R_{12}^Q(T_{\mathrm{pc}}(\mu_B), \mu_b)$ is shown as the gray band while the red line denotes the HRG result of R_{12}^Q evaluated on $T_{pc}(\mu_B)$. Since experimental measurements of electric charge fluctuations are not plagued with the proxy problem, we are tempted to compare our lattice QCD predictions with them. Therefore, the STAR collaborations results for R_{12}^Q from the BES-I program [67] are included in Figure 7.2 as horizontal lines. The error bars on the results are too small to be resolved in this figure.

By comparing the intersections of these experimental results with our continuum extrapolation for R_{12}^Q, we can obtain a mapping between baryon chemical potentials μ_B and beam energies $\sqrt{s}_{NN}$. Such comparisons have been proposed in the past [68][69] to obtain model independent determinations of freeze-out chemical potentials. Such a determination, however, crucially depends on the freeze-out temperature T_f which has to be determined from another quantity. As we will see later, an extraction of T_f from experimental results on higher order cumulants of electric charge fluctuations is not possible due to large uncertainties.

Instead of trying to extract $\mu_{B,f}$ ourselves, we can check whether freeze-out at or very close to the pseudo-critical transition line $T_{\mathrm{pc}}(\mu_B)$, as suggested by Figure 1.2, is consistent with our prediction of the mean-to-variance ratio M_Q/σ_Q^2.

Therefore, we summarize the chemical potentials extracted from comparing our prediction for M_Q/σ_Q^2 to the data from [67] in Table 7.1. The table furthermore includes the freeze-out chemical potentials extracted using the statistical hadronization model [43] as well as a previous determination of freeze-out chemical potentials from lattice QCD [69] based on R_{12}^Q and the ratio R_{12}^B/R_{12}^Q. The two

$\sqrt{s}_{NN}$ [GeV]	μ_B [MeV] (this work)	$\mu_{B,SHM}$ [MeV] [43]	$\mu_{B,WB}$ [MeV] [69]
200	21.1(7)	22.3	22(2)
62.4	61(2)	68.9	65(7)
39	95(3)	106.8	100(9)
27	131(4)	148	134(12)

Table 7.1: Chemical potentials extracted from comparing results from [67] at different beam energies with our continuum extrapolated lattice QCD prediction for $R_{12}^Q(T_{pc})$. Also listed are results from the statistical hadronization model (SHM), as well as a previous lattice QCD determination of $\mu_{B,f}$ from the Wuppertal-Budapest Collaboration.

lattice QCD results agree within errors while the freeze-out chemical potential determined from statistical hadronization is consistently larger than the chemical potential we obtain when using $T_{pc}(\mu_B)$. This is partly due to the fact that the HRG result for $R_{12}^Q(T_{pc}(\mu_B))$ is smaller than our lattice QCD prediction across the full chemical potential range depicted in Figure 7.2. This is in accordance with our finding that the second order charge fluctuation χ_2^Q, which gives the dominant contribution to the slope of R_{12}^Q, is consistently larger in HRG calculations without finite-volume corrections.

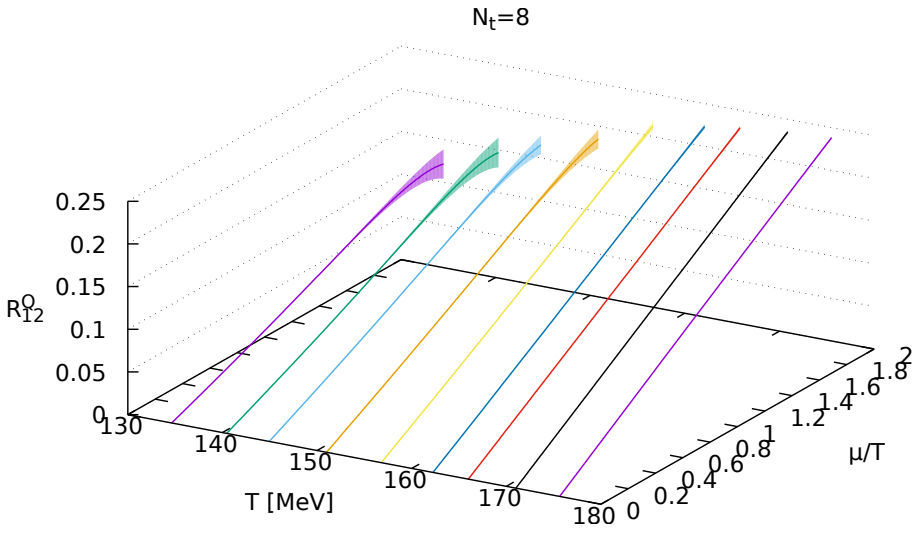

Figure 7.1: The mean-to-variance ratio R_{12}^Q of electric charge fluctuations for lattice with temporal extent $N_t = 8$ in the $(T, \hat{\mu}_B)$-plane.

7.2 Skewness ratio R_{31}^Q

Using the same procedure outlined before, we compute the skewness ratio $R_{31}^Q(T, \mu_B) = \frac{S_Q \sigma_Q^3}{M_Q} = \frac{\chi_3^Q}{\chi_1^Q}$ up to NNLO in μ_B which corresponds to $l_{\max} = k_{\max} = 5$. The results are presented in Figure 7.3 and 7.4 where the former depicts the temperature dependence of R_{31}^Q at vanishing baryon chemical potential while the latter shows the dependence on baryon chemical potential around $T = 156$ MeV. Compared to the mean to variance ratio discussed above, the roles of temperature and baryon chemical potential are reversed for the skewness ratio. There is a pronounced temperature dependence in the form of a (mirrored) sigmoidal curve, while a change in chemical potential only results in a very mild decrease of R_{31}^Q at a level of about 10%. With these properties, R_{31}^Q was proposed as a thermometer for extracting the freeze-out temperature T_f from comparison to experimental measurements [68].

In order to perform the continuum extrapolation, we fit $R_{31}^Q(T, \mu_B = 0)$ with a rational polynomial ansatz (6.1.5) as we have done for the baryon number fluctuations. The cut-off effects are again parameterized by $1/N_\tau^2$ correction terms.

If evaluated on the pseudo-critical crossover line $T_{pc}(\mu_B)$, the small suppression of R_{31}^Q with increasing μ_B is almost exactly compensated by the enhancement

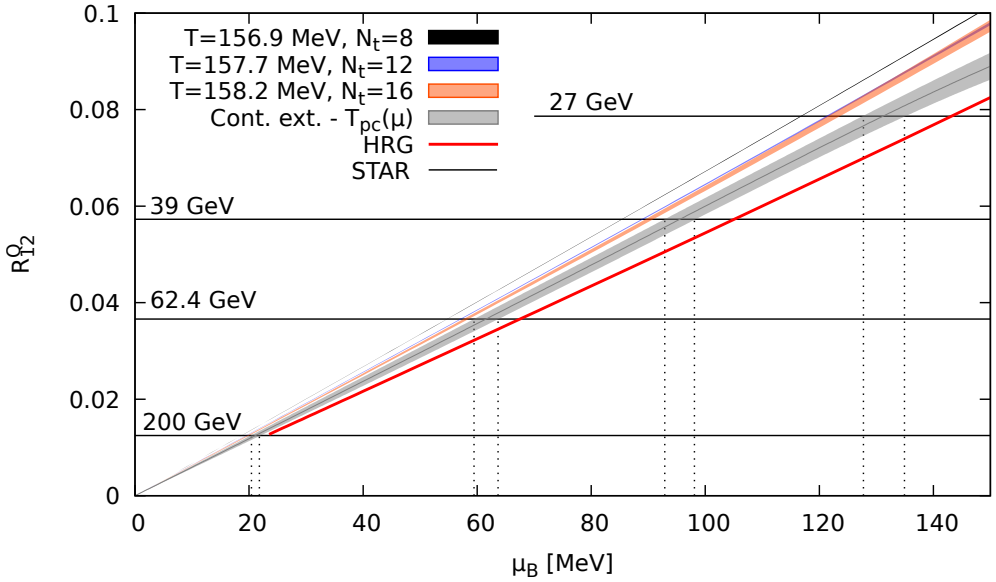

Figure 7.2: Continuum extrapolated mean-to-variance ratio R_{12}^Q of electric charge fluctuations evaluated on the pseudo-critical transition line of the chiral transition. The horizontal lines show corresponding results for R_{12}^Q measured by the STAR collaboration at beam energies $\sqrt{s}_{NN} = 27 - 200$ GeV [67].

of R_{31}^Q with decreasing temperature. $R_{31}^Q(T_{\rm pc}(\mu_B))$ therefore remains constant in the μ_B-region studied here and we find $R_{31}^Q(T_{\rm pc}(\mu_B)) = 1.04(9)$ for $\mu_B < 150$ MeV. The result is shown in Figure 7.5 as a red band with μ_B replaced with R_{12}^B as before. For chemical potentials larger than 150 MeV, the signal-to-noise ratio for the $N_\tau = 12$ and $N_\tau = 16$ data becomes too poor to form robust predictions.

When comparing our result on the pseudo-critical transition line with experimental measurements performed by the PHENIX Collaboration [70], included in Figure 7.5 as blue data points, we find that they are consistent with a freeze out temperature $T_f \sim T_{\rm pc}$. However, the uncertainties on the experimental determination of R_{31}^Q are substantial. Since the lattice QCD results suggest that the skewness ratio is almost independent of $R_{12}^{B/P}$, we may average over the experimental results to reduce the statistical uncertainty. This is included in 7.5 as a black dashed band that is slightly larger but still consistent with the lattice QCD determination within errors. Like the skewness and kurtosis ratios for net-baryon number fluctuations, this suggests a freeze-out temperature slightly below the pseudo-critical transition line.

HRG models only match our lattice QCD predictions at temperatures $T \leq 135$ MeV. The behavior of R_{31}^Q particularly in the region around $T_{\rm pc}$ cannot be

described with them.

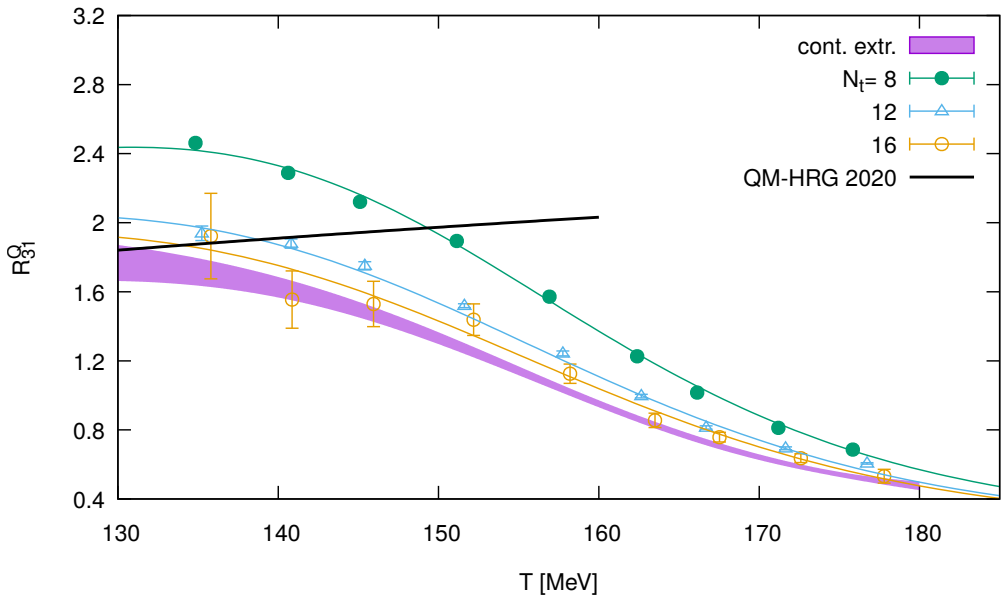

Figure 7.3: The skewness ratio $R^Q_{31} = S_Q\sigma^3_Q/M_Q$ at $\mu_B = 0$ as a function of temperature. Colored data points show the lattice QCD results at finite N_τ while the purple band shows the continuum extrapolation. The colored lines represent the fit function used for the continuum extrapolation evaluated at the corresponding finite N_τ values. The QM-HRG result is shown as a black line.

7.3 Kurtosis ratio R^Q_{42}

Furthermore, we computed the kurtosis ratio R^Q_{42} to NNLO in μ_B. Unlike the skewness ratio, R^Q_{42} does not contain noisy Baryon-electric charge correlations at $\mu_B = 0$ and therefore has significantly smaller errors then R^Q_{31} as shown in Figure 7.6. In the (T, μ_B)-plane, its behavior is very similar to the skewness ratio, i.e. it has a pronounced sigmoidal shape in T direction but hardly varies as a function of μ_B. The μ_B dependence is depicted in Figure 7.7. Therefore, evaluating R^Q_{42} along $T_{pc}(\mu_B)$ results in a nearly constant value and we obtain $R^Q_{42} = 0.71(5)$ for $\mu_B < 150$ MeV.

As the orders increase, the discrepancies between HRG model calculations and lattice QCD results grow. In the case of the kurtosis ratio, HRG results based on calculations without finite-volume corrections differ by more then 50% from our lattice QCD prediction at $T \sim 135$ MeV. This is partly due to finite volume effects in the light meson sector encountered earlier that become more severe

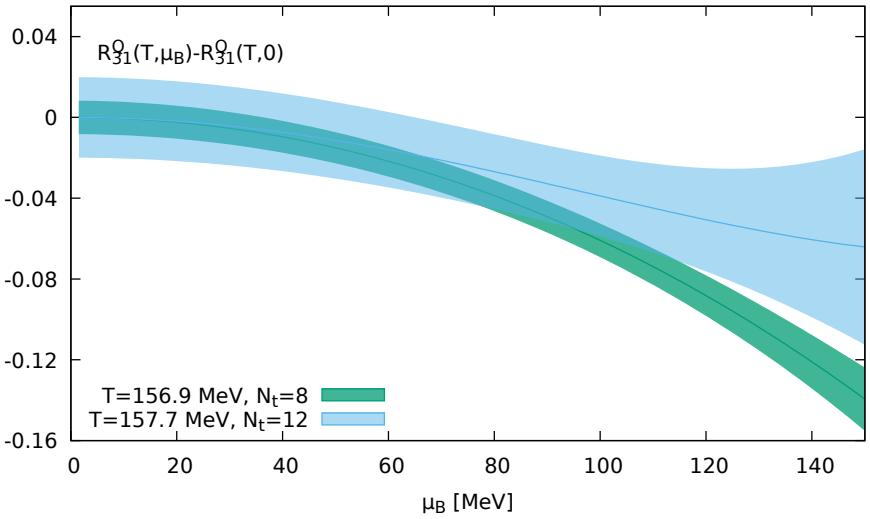

Figure 7.4: The subtracted skewness ratio $R^Q_{31}(T,\mu_B) - R^Q_{31}(T,0)$ around $T = 156$ MeV as a function of μ_B.

with increasing orders. These, however, do not have an influence on the μ_B-dependence of R^Q_{42}, shown in Figure 7.7, as the μ_B correction terms are mostly given by higher order baryon-charge correlations. Furthermore, residual taste changing interactions not fully suppressed by the HISQ formulation as well as a doubly charged resonance, the Δ^{++}, which is unstable well below T_{pc} in our lattice QCD calculations further decrease the value of R^Q_{42}.

7.4 Strangeness fluctuations and the strangeness chemical potential

While cumulant ratios of net strangeness fluctuations are also accessible in lattice QCD calculations, they do not provide much information on the thermal conditions present in heavy ion collisions as the proxy problem is more severe than it is for net baryon-number fluctuations. Results on the fluctuations of single strange particle species, such as kaons [71] and Λ-baryons [72] are available, but the viability of either of them as a proxy for net strangeness fluctuations is not clear as contributions from either the strange baryon or strange meson sector are neglected. However, insight on thermal conditions present in heavy ion collisions might be obtained via a different kind of strangeness observable originating from the strangeness neutrality constraint $n_S = 0$. Simply dividing equation (4.1.4) by

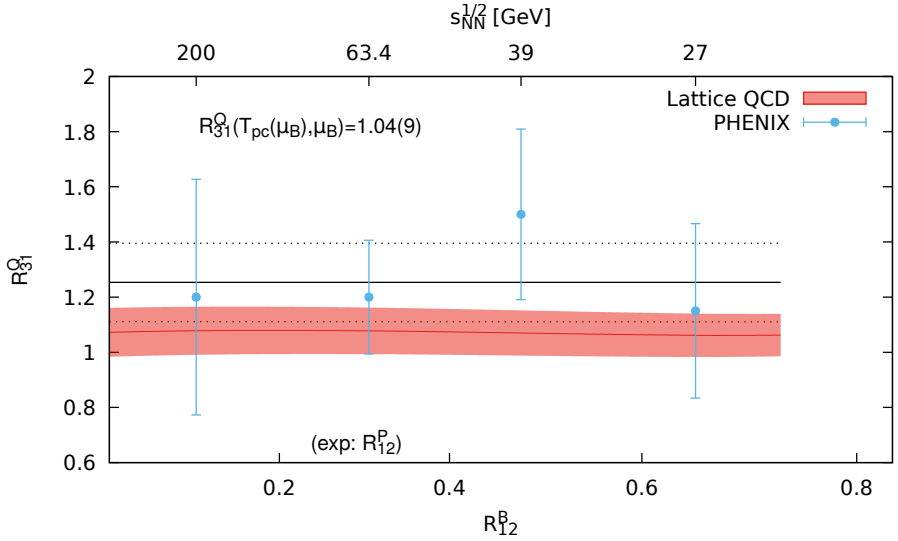

Figure 7.5: The continuum extrapolation of $R_{31}^{Q}(T_{\rm pc}(\mu_B),\mu_B)$ evaluated on the crossover line of the chiral transition shown as a red band. The blue data points show the corresponding measurements of R_{31}^{Q} from [70] whereas the black line corresponds to the average over these values.

$\hat{\mu}_B$ yields the ratio

$$\frac{\mu_S}{\mu_B} = s_1(T) + s_3(T)\left(\frac{\mu_B}{T}\right)^2 + \mathcal{O}\left(\left(\frac{\mu_B}{T}\right)^4\right), \tag{7.4.1}$$

which is, for small chemical potentials, to a large extent determined by $s_1(T) \simeq -\frac{\chi_{11}^{BS}}{\chi_2^S}$. The strangeness chemical potential to baryon chemical potential ratio is furthermore accessible in non-interacting hadron resonance gas models via the ratio of anti-strange baryon to strange baryon yields $\bar{B}/B$ [46] that is given by

$$\frac{\bar{B}}{B}(\sqrt{s}) = \exp\left(-\frac{\mu_B}{T}\left(2 - 2|S|\frac{\mu_S}{\mu_B}\right)\right). \tag{7.4.2}$$

We can fit experimentally measured yields of strange baryons with this expression to obtain the ratio μ_S/μ_B at the time of chemical freeze-out and compare it to lattice QCD calculations of the ratio from (7.4.1). The results of this are shown in Figure 7.8. We used measurements of Λ, Σ, and Ω yields published by STAR in [73] and [74] to fit (7.4.2) with μ_B and μ_S/μ_B as parameters. The lattice QCD curve, shown here in orange, is obtained by evaluating the leading order contribution $s_1(T_{pc}(\mu_B))$ on the pseudo-critical transition line. Also shown is the result for s_1 obtained from HRG calculations using the QMHRG2020 spectrum. Apart from

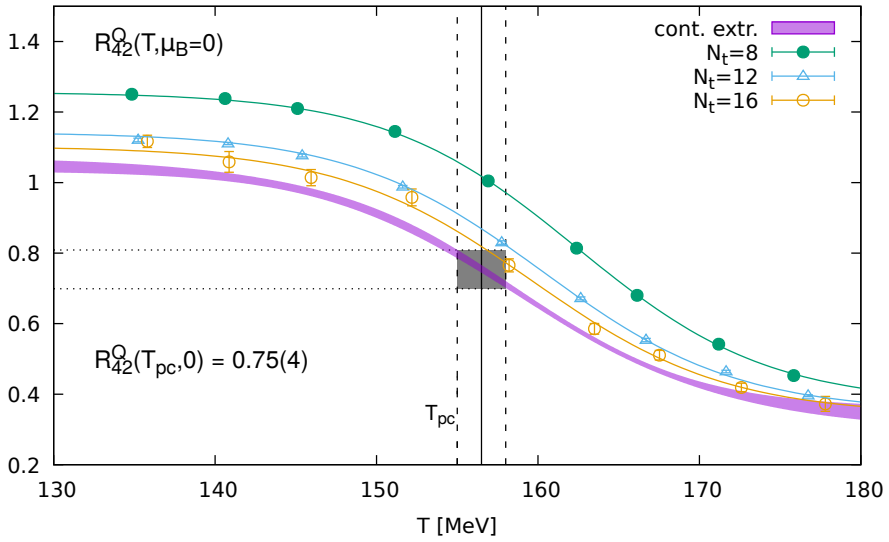

Figure 7.6: The kurtosis ratio $R^Q_{42}(T, \mu_B = 0)$ as a function of temperature. As before, colored data points show the lattice QCD results at finite N_τ while the purple band shows the continuum extrapolation. The colored lines show the continuum extrapolation fit evaluated at the corresponding N_τ values.

the data point at $\sqrt{s}_{NN} = 200$ GeV, the ratio of strangeness and baryon chemical potentials calculated on the pseudo-critical transition line via lattice QCD agrees with corresponding ratios extracted from the yield fit and is also quite close to the QMHRG calculation.

Furthermore, the ratio μ_S/μ_B is particularly sensitive to the strange hadron content of the hadronic spectrum. In Figure 7.9, we show the result of $s_1(T)$ based on the calculations presented in chapter 5 and compare it to QM and PDG HRG model calculations. The difference between the lattice QCD result of μ_S/μ_B and calculations based on the PDG spectrum is about 15%. Calculations based on the QMHRG2020 spectrum, however, compare quite well to the lattice QCD result.

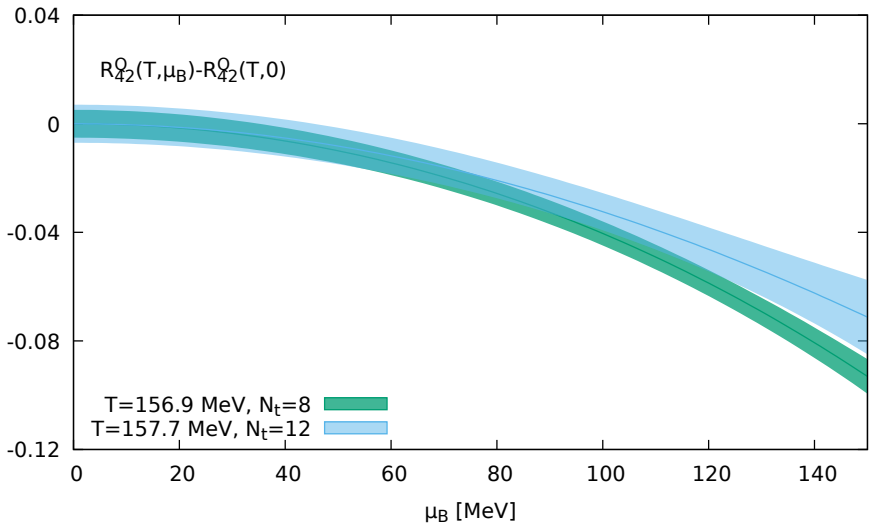

Figure 7.7: The subtracted kurtosis ratio $R^Q_{42}(T,\mu_B) - R^Q_{42}(T,0)$ around $T = 156$ MeV as a function of μ_B.

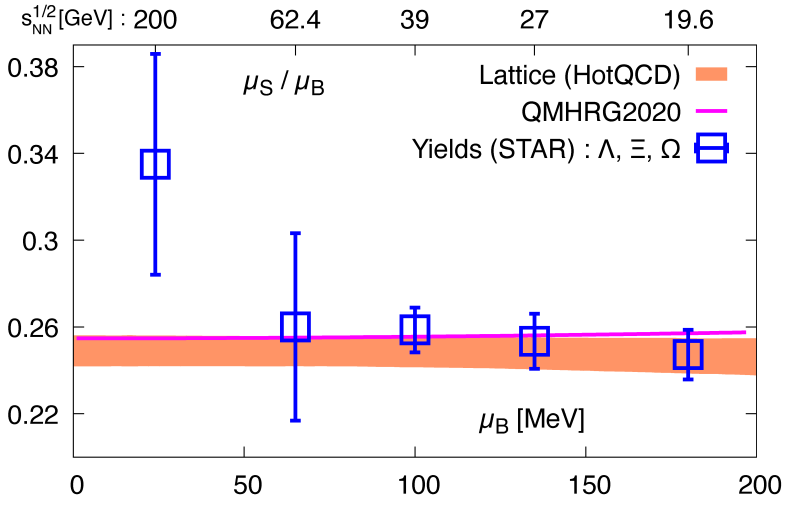

Figure 7.8: Comparison of the ratio of strangeness and baryon chemical potentials from fits to strange baryon yields and lattice QCD calculations on the pseudo-critical transition line.

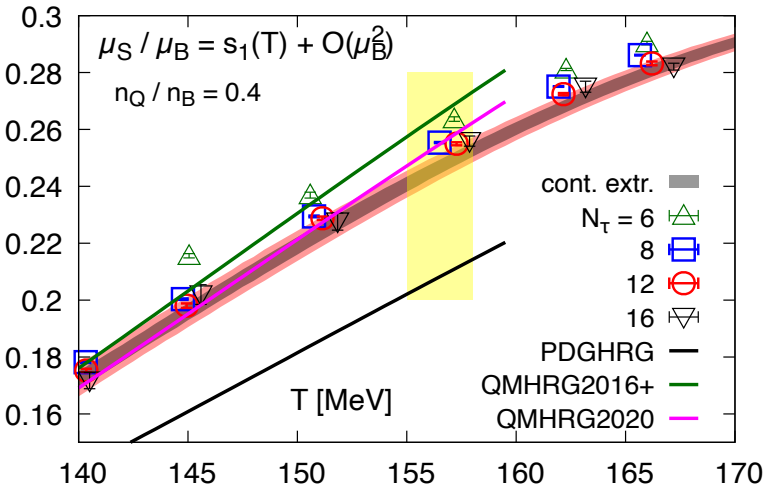

Figure 7.9: Leading order contribution $s_1(T)$ to the ratio of strangeness and baryon chemical potentials plotted as a function of temperature. Also shown are results from HRG calculations using PDG and QM spectra.

Chapter 8

Summary

We have computed all generalized susceptibilities χ_{ijk}^{BQS} up to order $i+j+k=8$ with lattice QCD simulations using the 2+1-flavor HISQ discretization scheme based on the high statistics data set listed in Table 3.2. Using this data, we obtained precise continuum extrapolations of the six second order cumulants of conserved charge fluctuations and their correlations and compared them to non-interacting, point-like hadron resonance gas calculations using different lists of hadron resonances. We found that calculations based on the QMHRG2020 hadron list agree well with lattice QCD results on strangeness fluctuations as well as the baryon-strangeness and electric charge-strangeness correlations for temperatures $135\ \mathrm{MeV}\ \leq T \leq T_{pc,0}$. For the second order electric charge cumulant, we found that the lattice QCD results, obtained on lattices with aspect ratio $LT=4$, are affected by finite volume effects in the pion and kaon sector. By correcting for these in QMHRG2020 calculations, we also found a good agreement with lattice results up to about $T_{pc,0}$. The most significant difference between non-interacting, point-like hadron resonance gases and lattice QCD was found in the baryon-charge correlation χ_{11}^{BQ}. While the discrepancy could be decreased by assigning an excluded volume to hadrons, an excluded volume parameter of $b>1$ fm would be required to describe the temperature dependence of χ_{11}^{BQ} which spoils the good agreement with strangeness correlations.

Calculations based on virial expansions can account for the interplay between repulsive and attractive interactions but their precision is currently limited due to insufficient experimental data on various interaction channels. Nonetheless, they provide an explanation why the $K_0^*(700)$ resonance does not contribute to the thermodynamics of a medium of strongly-interacting matter and should be excluded from non-interacting, point-like hadron resonance gas models.

Furthermore, we computed higher order cumulant ratios of baryon-number and electric charge fluctuations at small values of the baryon chemical potential μ_B for strangeness neutral systems $n_S=0$ and a ratio of electric charge density

to baryon number density $n_Q/n_B = 0.4$. We found the mean-to-variance ratios M_B/σ_B^2 and M_Q/σ_Q^2 to be mostly determined by their leading order contributions, giving them a monotonic, nearly linear dependence on μ_B. The former was found to agree well with HRG calculations up to chemical potentials of about 120 MeV while for the latter, finite volume effects already present in χ_2^Q as well as further deviations from QCD that start to appear close to T_{pc}, lead to a smaller slope of R_{12}^Q in HRG calculations compared to lattice QCD results.

We found the skewness and kurtosis ratios for net baryon-number fluctuations and net electric charge fluctuations to depend only mildly on μ_B and consequently on R_{12}^B and found that effects of truncating the Taylor series are small for chemical potentials $\mu_B/T \leq 1$. We furthermore evaluated these ratios on the pseudo-critical transition line $T_{pc}(\mu_B)$ and compared them, with the caveats of such comparisons in mind, with corresponding measurements performed by STAR and PHENIX. We found a good agreement between skewness and kurtosis ratios of net baryon-number fluctuations with corresponding net proton-number fluctuations measured by STAR which suggest a freeze-out temperature slightly below T_{pc}. Similar comparisons of the skewness ratio for net electric charge fluctuations with data from PHENIX also arrive at this conclusion, however statistical uncertainties on the experimental results are large. A determination of μ_S/μ_B on the pseudo-critical transition line from lattice QCD, and μ_S/μ_B at the time of freeze-out, extracted from strange baryon yield measurements also favors freeze-out occurring in the vicinity of T_{pc}. Furthermore, we presented first estimates of fifth and sixth order cumulant ratios of net baryon-number fluctuations based on NLO calculations on lattices with $N_\tau = 8$ which we found to be negative along $T_{pc}(\mu_B)$. While earlier, preliminary results on corresponding net proton-number fluctuations obtained by STAR, indicated a clear deviation from lattice QCD results, a recent, complete analysis shows that uncertainties on these quantities are currently to large to make statements about the thermodynamic consistenty of them with our other findings.

Appendix A

Expressions for constrained expansion coefficients $\tilde{\chi}_n^{X,k}$

Baryon number

The constrained expansion coefficients $\tilde{\chi}_n^{B,k}$ for odd n are

$$
\begin{aligned}
\tilde{\chi}_n^{B,1} &= s_1\chi_{n01}^{BQS} + q_1\chi_{n10}^{BQS} + \chi_{n+1,00}^{BQS},\\
\tilde{\chi}_n^{B,3} &= (6s_3\chi_{n01}^{BQS} + s_1^3\chi_{n03}^{BQS} + 6q_3\chi_{n10}^{BQS} + 3q_1s_1^2\chi_{n12}^{BQS} + 3q_1^2s_1\chi_{n21}^{BQS} + q_1^3\chi_{n30}^{BQS}\\
&\quad + 3s_1^2\chi_{n+1,02}^{BQS} + 6q_1s_1\chi_{n+1,11}^{BQS} + 3q_1^2\chi_{n+1,20}^{BQS} + 3s_1\chi_{n+2,01}^{BQS} + 3q_1\chi_{n+2,10}^{BQS} + \chi_{n+3,00}^{BQS})/6,\\
\tilde{\chi}_n^{B,5} &= (120s_5\chi_{n01}^{BQS} + 60s_1^2s_3\chi_{n03}^{BQS} + s_1^5\chi_{n05}^{BQS}\\
&\quad + 120q_5\chi_{n10}^{BQS} + 60q_3s_1^2\chi_{n12}^{BQS} + 120q_1s_1s_3\chi_{n12}^{BQS} + 5q_1s_1^4\chi_{n14}^{BQS}\\
&\quad + 120q_1q_3s_1\chi_{n21}^{BQS} + 60q_1^2s_3\chi_{n21}^{BQS} + 10q_1^2s_1^3\chi_{n23}^{BQS} + 60q_1^2q_3\chi_{n30}^{BQS}\\
&\quad + 10q_1^3s_1^2\chi_{n32}^{BQS} + 5q_1^4s_1\chi_{n41}^{BQS} + q_1^5\chi_{n50}^{BQS} + 120s_1s_3\chi_{n+1,02}^{BQS} + 5s_1^4\chi_{n+1,04}^{BQS}\\
&\quad + 120q_3s_1\chi_{n+1,11}^{BQS} + 120q_1s_3\chi_{n+1,11}^{BQS} + 20q_1s_1^3\chi_{n+1,13}^{BQS} + 120q_1q_3\chi_{n+1,20}^{BQS}\\
&\quad + 30q_1^2s_1^2\chi_{n+1,22}^{BQS} + 20q_1^3s_1\chi_{n+1,31}^{BQS} + 5q_1^4\chi_{n+1,40}^{BQS} + 60s_3\chi_{n+2,01}^{BQS} + 10s_1^3\chi_{n+2,03}^{BQS}\\
&\quad + 60q_3\chi_{n+2,10}^{BQS} + 30q_1s_1^2\chi_{n+2,12}^{BQS} + 30q_1^2s_1\chi_{n+2,21}^{BQS} + 10q_1^3\chi_{n+2,30}^{BQS} + 10s_1^2\chi_{n+3,02}^{BQS}\\
&\quad + 20q_1s_1\chi_{n+3,11}^{BQS} + 10q_1^2\chi_{n+3,20}^{BQS} + 5s_1\chi_{n+4,01}^{BQS} + 5q_1\chi_{n+4,10}^{BQS} + \chi_{n+5,00}^{BQS})/120,
\end{aligned}
$$

$$
\begin{aligned}
\tilde{\chi}_n^{B,7} = (&5040 s_7 \chi_{n01}^{BQS} + 2520 s_1 s_3^2 \chi_{n03}^{BQS} \\
&+ 2520 s_1^2 s_5 \chi_{n03}^{BQS} + 210 s_1^4 s_3 \chi_{n05}^{BQS} + s_1^7 \chi_{n07}^{BQS} + 5040 q_7 \chi_{n10}^{BQS} + 2520 q_5 s_1^2 \chi_{n12}^{BQS} \\
&+ 5040 q_3 s_1 s_3 \chi_{n12}^{BQS} + 2520 q_1 s_3^2 \chi_{n12}^{BQS} + 5040 q_1 s_1 s_5 \chi_{n12}^{BQS} + 210 q_3 s_1^4 \chi_{n14}^{BQS} \\
&+ 840 q_1 s_1^3 s_3 \chi_{n14}^{BQS} + 7 q_1 s_1^6 \chi_{n16}^{BQS} + 2520 q_3^2 s_1 \chi_{n21}^{BQS} + 5040 q_1 q_5 s_1 \chi_{n21}^{BQS} \\
&+ 5040 q_1 q_3 s_3 \chi_{n21}^{BQS} + 2520 q_1^2 s_5 \chi_{n21}^{BQS} + 840 q_1 q_3 s_1^3 \chi_{n23}^{BQS} + 1260 q_1^2 s_1^2 s_3 \chi_{n23}^{BQS} \\
&+ 21 q_1^2 s_1^5 \chi_{n25}^{BQS} + 2520 q_1 q_3^2 \chi_{n30}^{BQS} + 2520 q_1^2 q_5 \chi_{n30}^{BQS} + 1260 q_1^2 q_3 s_1^2 \chi_{n32}^{BQS} \\
&+ 840 q_1^3 s_1 s_3 \chi_{n32}^{BQS} + 35 q_1^3 s_1^4 \chi_{n34}^{BQS} + 840 q_1^3 q_3 s_1 \chi_{n41}^{BQS} + 210 q_1^4 s_3 \chi_{n41}^{BQS} \\
&+ 35 q_1^4 s_1^3 \chi_{n43}^{BQS} + 210 q_1^4 q_3 \chi_{n50}^{BQS} + 21 q_1^5 s_1^2 \chi_{n52}^{BQS} + 7 q_1^6 s_1 \chi_{n61}^{BQS} \\
&+ q_1^7 \chi_{n70}^{BQS} + 2520 s_3^2 \chi_{n+1,02}^{BQS} + 5040 s_1 s_5 \chi_{n+1,02}^{BQS} + 840 s_1^3 s_3 \chi_{n+1,04}^{BQS} + 7 s_1^6 \chi_{n+1,06}^{BQS} \\
&+ 5040 q_5 s_1 \chi_{n+1,11}^{BQS} + 5040 q_3 s_3 \chi_{n+1,11}^{BQS} + 5040 q_1 s_5 \chi_{n+1,11}^{BQS} + 840 q_3 s_1^3 \chi_{n+1,13}^{BQS} \\
&+ 2520 q_1 s_1^2 s_3 \chi_{n+1,13}^{BQS} + 42 q_1 s_1^5 \chi_{n+1,15}^{BQS} + 2520 q_3^2 \chi_{n+1,20}^{BQS} + 5040 q_1 q_5 \chi_{n+1,20}^{BQS} \\
&+ 2520 q_1 q_3 s_1^2 \chi_{n+1,22}^{BQS} + 2520 q_1^2 s_1 s_3 \chi_{n+1,22}^{BQS} + 105 q_1^2 s_1^4 \chi_{n+1,24}^{BQS} + 2520 q_1^2 q_3 s_1 \chi_{n+1,31}^{BQS} \\
&+ 840 q_1^3 s_3 \chi_{n+1,31}^{BQS} + 140 q_1^3 s_1^3 \chi_{n+1,33}^{BQS} + 840 q_1^3 q_3 \chi_{n+1,40}^{BQS} + 105 q_1^4 s_1^2 \chi_{n+1,42}^{BQS} + 42 q_1^5 s_1 \chi_{n+1,51}^{BQS} \\
&+ 7 q_1^6 \chi_{n+1,60}^{BQS} + 2520 s_5 \chi_{n+2,01}^{BQS} + 1260 s_1^2 s_3 \chi_{n+2,03}^{BQS} + 21 s_1^5 \chi_{n+2,05}^{BQS} + 2520 q_5 \chi_{n+2,10}^{BQS} \\
&+ 1260 q_3 s_1^2 \chi_{n+2,12}^{BQS} + 2520 q_1 s_1 s_3 \chi_{n+2,12}^{BQS} + 105 q_1 s_1^4 \chi_{n+2,14}^{BQS} + 2520 q_1 q_3 s_1 \chi_{n+2,21}^{BQS} \\
&+ 1260 q_1^2 s_3 \chi_{n+2,21}^{BQS} + 210 q_1^2 s_1^3 \chi_{n+2,23}^{BQS} + 1260 q_1^2 q_3 \chi_{n+2,30}^{BQS} + 210 q_1^3 s_1^2 \chi_{n+2,32}^{BQS} \\
&+ 105 q_1^4 s_1 \chi_{n+2,41}^{BQS} + 21 q_1^5 \chi_{n+2,50}^{BQS} + 840 s_1 s_3 \chi_{n+3,02}^{BQS} + 35 s_1^4 \chi_{n+3,04}^{BQS} \\
&+ 840 q_3 s_1 \chi_{n+3,11}^{BQS} + 840 q_1 s_3 \chi_{n+3,11}^{BQS} + 140 q_1 s_1^3 \chi_{n+3,13}^{BQS} + 840 q_1 q_3 \chi_{n+3,20}^{BQS} \\
&+ 210 q_1^2 s_1^2 \chi_{n+3,22}^{BQS} + 140 q_1^3 s_1 \chi_{n+3,31}^{BQS} + 35 q_1^4 \chi_{n+3,40}^{BQS} + 210 s_3 \chi_{n+4,01}^{BQS} + 35 s_1^3 \chi_{n+4,03}^{BQS} \\
&+ 210 q_3 \chi_{n+4,10}^{BQS} + 105 q_1 s_1^2 \chi_{n+4,12}^{BQS} + 105 q_1^2 s_1 \chi_{n+4,21}^{BQS} + 35 q_1^3 \chi_{n+4,30}^{BQS} + 21 s_1^2 \chi_{n+5,02}^{BQS} \\
&+ 42 q_1 s_1 \chi_{n+5,11}^{BQS} + 21 q_1^2 \chi_{n+5,20}^{BQS} + 7 s_1 \chi_{n+6,01}^{BQS} + 7 q_1 \chi_{n+6,10}^{BQS} + \chi_{n+7,00}^{BQS}) / 5040.
\end{aligned}
$$

APPENDIX A. EXPRESSIONS FOR CONSTRAINED EXPANSION COEFFICIENTS $\tilde{\chi}_N^{X,K}$

The constrained expansion coefficients $\tilde{\chi}_n^{B,k}$ for even n are

$$
\begin{aligned}
\tilde{\chi}_n^{B} &= \chi_{n00}^{BQS}, \\
\tilde{\chi}_n^{B,2} &= (\chi_{n+2,00}^{BQS} + s_1^2\chi_{n02}^{BQS} + q_1^2\chi_{n20}^{BQS} + 2s_1\chi_{n+1,01}^{BQS} + 2q_1\chi_{n+1,10}^{BQS} + 2q_1s_1\chi_{n11}^{BQS})/2, \\
\tilde{\chi}_n^{B,4} &= (24s_1s_3\chi_{n02}^{BQS} + s_1^4\chi_{n04}^{BQS} + 24q_3s_1\chi_{n11}^{BQS} + 24q_1s_3\chi_{n11}^{BQS} + 4q_1s_1^3\chi_{n13}^{BQS} \\
&\quad + 24q_1q_3\chi_{n20}^{BQS} + 6q_1^2s_1^2\chi_{n22}^{BQS} + 4q_1^3s_1\chi_{n31}^{BQS} + q_1^4\chi_{n40}^{BQS} + 24s_3\chi_{n+1,01}^{BQS} + 4s_1^3\chi_{n+1,03}^{BQS} \\
&\quad + 24q_3\chi_{n+1,10}^{BQS} + 12q_1s_1^2\chi_{n+1,12}^{BQS} + 12q_1^2s_1\chi_{n+1,21}^{BQS} + 4q_1^3\chi_{n+1,30}^{BQS} + 6s_1^2\chi_{n+2,02}^{BQS} + 12q_1s_1\chi_{n+2,11}^{BQS} \\
&\quad + 6q_1^2\chi_{n+2,20}^{BQS} + 4s_1\chi_{n+3,01}^{BQS} + 4q_1\chi_{n+3,10}^{BQS} + \chi_{n+4,00}^{BQS})/24, \\
\tilde{\chi}_n^{B,6} &= (360s_3^2\chi_{n02}^{BQS} + 720s_1s_5\chi_{n02}^{BQS} + 120s_1^3s_3\chi_{n04}^{BQS} + s_1^6\chi_{n06}^{BQS} + 720q_5s_1\chi_{n11}^{BQS} \\
&\quad + 720q_3s_3\chi_{n11}^{BQS} + 720q_1s_5\chi_{n11}^{BQS} + 120q_3s_1^3\chi_{n13}^{BQS} + 360q_1s_1^2s_3\chi_{n13}^{BQS} + 6q_1s_1^5\chi_{n15}^{BQS} \\
&\quad + 360q_3^2\chi_{n20}^{BQS} + 720q_1q_5\chi_{n20}^{BQS} + 360q_1q_3s_1^2\chi_{n22}^{BQS} + 360q_1^2s_1s_3\chi_{n22}^{BQS} + 15q_1^2s_1^4\chi_{n24}^{BQS} \\
&\quad + 360q_1^2q_3s_1\chi_{n31}^{BQS} + 120q_1^3s_3\chi_{n31}^{BQS} + 20q_1^3s_1^3\chi_{n33}^{BQS} + 120q_1^3q_3\chi_{n40}^{BQS} + 15q_1^4s_1^2\chi_{n42}^{BQS} \\
&\quad + 6q_1^5s_1\chi_{n51}^{BQS} + q_1^6\chi_{n60}^{BQS} + 720s_5\chi_{n+1,01}^{BQS} + 360s_1^2s_3\chi_{n+1,03}^{BQS} + 6s_1^5\chi_{n+1,05}^{BQS} + 720q_5\chi_{n+1,10}^{BQS} \\
&\quad + 360q_3s_1^2\chi_{n+1,12}^{BQS} + 720q_1s_1s_3\chi_{n+1,12}^{BQS} + 30q_1s_1^4\chi_{n+1,14}^{BQS} + 720q_1q_3s_1\chi_{n+1,21}^{BQS} + 360q_1^2s_3\chi_{n+1,21}^{BQS} \\
&\quad + 60q_1^2s_1^3\chi_{n+1,23}^{BQS} + 360q_1^2q_3\chi_{n+1,30}^{BQS} + 60q_1^3s_1^2\chi_{n+1,32}^{BQS} + 30q_1^4s_1\chi_{n+1,41}^{BQS} + 6q_1^5\chi_{n+1,50}^{BQS} \\
&\quad + 360s_1s_3\chi_{n+2,02}^{BQS} + 15s_1^4\chi_{n+2,04}^{BQS} + 360q_3s_1\chi_{n+2,11}^{BQS} + 360q_1s_3\chi_{n+2,11}^{BQS} + 60q_1s_1^3\chi_{n+2,13}^{BQS} \\
&\quad + 360q_1q_3\chi_{n+2,20}^{BQS} + 90q_1^2s_1^2\chi_{n+2,22}^{BQS} + 60q_1^3s_1\chi_{n+2,31}^{BQS} + 15q_1^4\chi_{n+2,40}^{BQS} + 120s_3\chi_{n+3,01}^{BQS} + 20s_1^3\chi_{n+3,03}^{BQS} \\
&\quad + 120q_3\chi_{n+3,10}^{BQS} + 60q_1s_1^2\chi_{n+3,12}^{BQS} + 60q_1^2s_1\chi_{n+3,21}^{BQS} + 20q_1^3\chi_{n+3,30}^{BQS} + 15s_1^2\chi_{n+4,02}^{BQS} + 30q_1s_1\chi_{n+4,11}^{BQS} \\
&\quad + 15q_1^2\chi_{n+4,20}^{BQS} + 6s_1\chi_{n+5,01}^{BQS} + 6q_1\chi_{n+5,10}^{BQS} + \chi_{n+6,00}^{BQS})/720,
\end{aligned}
$$

Electric charge

The constrained expansion coefficients for $\tilde{\chi}_n^{Q,k}$ for odd n are

$$
\begin{aligned}
\tilde{\chi}_n^{Q,1} &= \chi^{BQS}_{1,n,0} + s_1\chi^{BQS}_{0,n,1} + q_1\chi^{BQS}_{0,n+1,0},\\
\tilde{\chi}_n^{Q,3} &= (3q_1^2 s_1\chi^{BQS}_{0,n+2,1} + 3q_1 s_1^2\chi^{BQS}_{0,n+1,2} + 6q_1 s_1\chi^{BQS}_{1,n+1,1} + q_1^3\chi^{BQS}_{0,n+3,0}\\
&\quad + 3q_1^2\chi^{BQS}_{1,n+2,0} + 3q_1\chi^{BQS}_{2,n+1,0} + s_1^3\chi^{BQS}_{0,n,3} + 3s_1^2\chi^{BQS}_{1,n,2}\\
&\quad + 3s_1\chi^{BQS}_{2,n,1} + \chi^{BQS}_{3,n,0} + 6s_3\chi^{BQS}_{0,n,1} + 6q_3\chi^{BQS}_{0,n+1,0})/6\\
\tilde{\chi}_n^{Q,5} &= (5q_1^4 s_1\chi^{BQS}_{0,n+4,1} + 10q_1^3 s_1^2\chi^{BQS}_{0,n+3,2} + 20q_1^3 s_1\chi^{BQS}_{1,n+3,1} + 60q_1^2 s_3\chi^{BQS}_{0,n+2,1}\\
&\quad + 10q_1^2 s_1^3\chi^{BQS}_{0,n+2,3} + 30q_1^2 s_1^2\chi^{BQS}_{1,n+2,2} + 30q_1^2 s_1\chi^{BQS}_{2,n+2,1}\\
&\quad + 120q_1 s_1 s_3\chi^{BQS}_{0,n+1,2} + 5q_1 s_1^4\chi^{BQS}_{0,n+1,4} + 120q_3 q_1 s_1\chi^{BQS}_{0,n+2,1}\\
&\quad + 120q_1 s_3\chi^{BQS}_{1,n+1,1} + 20q_1 s_1^3\chi^{BQS}_{1,n+1,3} + 30q_1 s_1^2\chi^{BQS}_{2,n+1,2} + 20q_1 s_1\chi^{BQS}_{3,n+1,1}\\
&\quad + 60q_3 s_1^2\chi^{BQS}_{0,n+1,2} + 120q_3 s_1\chi^{BQS}_{1,n+1,1} + q_1^5\chi^{BQS}_{0,n+5,0} + 5q_1^4\chi^{BQS}_{1,n+4,0}\\
&\quad + 10q_1^3\chi^{BQS}_{2,n+3,0} + 60q_3 q_1^2\chi^{BQS}_{0,n+3,0} + 10q_1^2\chi^{BQS}_{3,n+2,0} + 120q_3 q_1\chi^{BQS}_{1,n+2,0}\\
&\quad + 5q_1\chi^{BQS}_{4,n+1,0} + 60q_3\chi^{BQS}_{2,n+1,0} + 60s_1^2 s_3\chi^{BQS}_{0,n,3} + s_1^5\chi^{BQS}_{0,n,5} + 120s_1 s_3\chi^{BQS}_{1,n,2}\\
&\quad + 5s_1^4\chi^{BQS}_{1,n,4} + 60s_3\chi^{BQS}_{2,n,1} + 10s_1^3\chi^{BQS}_{2,n,3} + 10s_1^2\chi^{BQS}_{3,n,2} + 5s_1\chi^{BQS}_{4,n,1}\\
&\quad + \chi^{BQS}_{5,n,0} + 120s_5\chi^{BQS}_{0,n,1} + 120q_5\chi^{BQS}_{0,n+1,0})/120,
\end{aligned}
$$

APPENDIX A. EXPRESSIONS FOR CONSTRAINED EXPANSION COEFFICIENTS $\tilde{\chi}_N^{X,K}$

$$
\begin{aligned}
\tilde{\chi}_n^{Q,7} = (&2520 s_1 s_3^2 \chi_{0,n,3}^{BQS} + 2520 s_1^2 s_5 \chi_{0,n,3}^{BQS} + 210 s_1^4 s_3 \chi_{0,n,5}^{BQS} + s_1^7 \chi_{0,n,7}^{BQS} + 2520 q_5 s_1^2 \chi_{0,n+1,2}^{BQS} \\
&+ 5040 q_3 s_1 s_3 \chi_{0,n+1,2}^{BQS} + 2520 q_1 s_3^2 \chi_{0,n+1,2}^{BQS} + 5040 q_1 s_1 s_5 \chi_{0,n+1,2}^{BQS} + 210 q_3 s_1^4 \chi_{0,n+1,4}^{BQS} \\
&+ 840 q_1 s_1^3 s_3 \chi_{0,n+1,4}^{BQS} + 7 q_1 s_1^6 \chi_{0,n+1,6}^{BQS} + 2520 q_3^2 s_1 \chi_{0,n+2,1}^{BQS} + 5040 q_1 q_5 s_1 \chi_{0,n+2,1}^{BQS} \\
&+ 5040 q_1 q_3 s_3 \chi_{0,n+2,1}^{BQS} + 2520 q_1^2 s_5 \chi_{0,n+2,1}^{BQS} + 840 q_1 q_3 s_1^3 \chi_{0,n+2,3}^{BQS} + 1260 q_1^2 s_1^2 s_3 \chi_{0,n+2,3}^{BQS} \\
&+ 21 q_1^2 s_1^5 \chi_{0,n+2,5}^{BQS} + 2520 q_1 q_3^2 \chi_{0,n+3,0}^{BQS} + 2520 q_1^2 q_5 \chi_{0,n+3,0}^{BQS} + 1260 q_1^2 q_3 s_1^2 \chi_{0,n+3,2}^{BQS} \\
&+ 840 q_1^3 s_1 s_3 \chi_{0,n+3,2}^{BQS} + 35 q_1^3 s_1^4 \chi_{0,n+3,4}^{BQS} + 840 q_1^3 q_3 s_1 \chi_{0,n+4,1}^{BQS} \\
&+ 210 q_1^4 s_3 \chi_{0,n+4,1}^{BQS} + 35 q_1^4 s_1^3 \chi_{0,n+4,3}^{BQS} + 210 q_1^4 q_3 \chi_{0,n+5,0}^{BQS} + 21 q_1^5 s_1^2 \chi_{0,n+5,2}^{BQS} + 7 q_1^6 s_1 \chi_{0,n+6,1}^{BQS} \\
&+ q_1^7 \chi_{0,n+7,0}^{BQS} + 2520 s_3^2 \chi_{1,n,2}^{BQS} + 5040 s_1 s_5 \chi_{1,n,2}^{BQS} + 840 s_1^3 s_3 \chi_{1,n,4}^{BQS} + 7 s_1^6 \chi_{1,n,6}^{BQS} + 5040 q_5 s_1 \chi_{1,n+1,1}^{BQS} \\
&+ 5040 q_3 s_3 \chi_{1,n+1,1}^{BQS} + 5040 q_1 s_5 \chi_{1,n+1,1}^{BQS} + 840 q_3 s_1^3 \chi_{1,n+1,3}^{BQS} + 2520 q_1 s_1^2 s_3 \chi_{1,n+1,3}^{BQS} \\
&+ 42 q_1 s_1^5 \chi_{1,n+1,5}^{BQS} + 2520 q_3^2 \chi_{1,n+2,0}^{BQS} + 5040 q_1 q_5 \chi_{1,n+2,0}^{BQS} + 2520 q_1 q_3 s_1^2 \chi_{1,n+2,2}^{BQS} \\
&+ 2520 q_1^2 s_1 s_3 \chi_{1,n+2,2}^{BQS} + 105 q_1^2 s_1^4 \chi_{1,n+2,4}^{BQS} + 2520 q_1^2 q_3 s_1 \chi_{1,n+3,1}^{BQS} \\
&+ 840 q_1^3 s_3 \chi_{1,n+3,1}^{BQS} + 140 q_1^3 s_1^3 \chi_{1,n+3,3}^{BQS} + 840 q_1^3 q_3 \chi_{1,n+4,0}^{BQS} + 105 q_1^4 s_1^2 \chi_{1,n+4,2}^{BQS} \\
&+ 42 q_1^5 s_1 \chi_{1,n+5,1}^{BQS} + 7 q_1^6 \chi_{1,n+6,0}^{BQS} + 2520 s_5 \chi_{2,n,1}^{BQS} + 1260 s_1^2 s_3 \chi_{2,n,3}^{BQS} + 21 s_1^5 \chi_{2,n,5}^{BQS} + 2520 q_5 \chi_{2,n+1,0}^{BQS} \\
&+ 1260 q_3 s_1^2 \chi_{2,n+1,2}^{BQS} + 2520 q_1 s_1 s_3 \chi_{2,n+1,2}^{BQS} + 105 q_1 s_1^4 \chi_{2,n+1,4}^{BQS} \\
&+ 2520 q_1 q_3 s_1 \chi_{2,n+2,1}^{BQS} + 1260 q_1^2 s_3 \chi_{2,n+2,1}^{BQS} + 210 q_1^2 s_1^3 \chi_{2,n+2,3}^{BQS} + 1260 q_1^2 q_3 \chi_{2,n+3,0}^{BQS} \\
&+ 210 q_1^3 s_1^2 \chi_{2,n+3,2}^{BQS} + 105 q_1^4 s_1 \chi_{2,n+4,1}^{BQS} + 21 q_1^5 \chi_{2,n+5,0}^{BQS} + 840 s_1 s_3 \chi_{3,n,2}^{BQS} + 35 s_1^4 \chi_{3,n,4}^{BQS} \\
&+ 840 q_3 s_1 \chi_{3,n+1,1}^{BQS} + 840 q_1 s_3 \chi_{3,n+1,1}^{BQS} + 140 q_1 s_1^3 \chi_{3,n+1,3}^{BQS} + 840 q_1 q_3 \chi_{3,n+2,0}^{BQS} + 210 q_1^2 s_1^2 \chi_{3,n+2,2}^{BQS} \\
&+ 140 q_1^3 s_1 \chi_{3,n+3,1}^{BQS} + 35 q_1^4 \chi_{3,n+4,0}^{BQS} + 210 s_3 \chi_{4,n,1}^{BQS} + 35 s_1^3 \chi_{4,n,3}^{BQS} \\
&+ 210 q_3 \chi_{4,n+1,0}^{BQS} + 105 q_1 s_1^2 \chi_{4,n+1,2}^{BQS} + 105 q_1^2 s_1 \chi_{4,n+2,1}^{BQS} + 35 q_1^3 \chi_{4,n+3,0}^{BQS} \\
&+ 21 s_1^2 \chi_{5,n,2}^{BQS} + 42 q_1 s_1 \chi_{5,n+1,1}^{BQS} + 21 q_1^2 \chi_{5,n+2,0}^{BQS} + 7 s_1 \chi_{6,n,1}^{BQS} + 7 q_1 \chi_{6,n+1,0}^{BQS} \\
&+ \chi_{7,n,0}^{BQS} + 5040 s_7 \chi_{0,n,1}^{BQS} + 5040 q_7 \chi_{0,n+1,0}^{BQS}) / 5040.
\end{aligned}
$$

The constrained expansion coefficients $\tilde{\chi}_n^{Q,k}$ for odd n are

$$
\begin{aligned}
\tilde{\chi}_n^{Q} &= \chi_{0,n,0}^{BQS},\\
\tilde{\chi}_n^{Q,2} &= (\chi_{2,n,0}^{BQS} + 2s_1\chi_{1,n,1}^{BQS} + 2q_1\chi_{1,n+1,0}^{BQS} + 2s_1q_1\chi_{0,n+1,1}^{BQS} + s_1^2\chi_{0,n,2}^{BQS} + q_1^2\chi_{0,n+2,0}^{BQS})/2,\\
\tilde{\chi}_n^{Q,4} &= (24s_1s_3\chi_{0,n,2}^{BQS} + s_1^4\chi_{0,n,4}^{BQS} + 24q_3s_1\chi_{0,n+1,1}^{BQS} + 24q_1s_3\chi_{0,n+1,1}^{BQS} + 4q_1s_1^3\chi_{0,n+1,3}^{BQS}\\
&\quad + 24q_1q_3\chi_{0,n+2,0}^{BQS} + 6q_1^2s_1^2\chi_{0,n+2,2}^{BQS} + 4q_1^3s_1\chi_{0,n+3,1}^{BQS} + q_1^4\chi_{0,n+4,0}^{BQS} + 24s_3\chi_{1,n,1}^{BQS}\\
&\quad + 4s_1^3\chi_{1,n,3}^{BQS} + 24q_3\chi_{1,n+1,0}^{BQS} + 12q_1s_1^2\chi_{1,n+1,2}^{BQS} + 12q_1^2s_1\chi_{1,n+2,1}^{BQS} + 4q_1^3\chi_{1,n+3,0}^{BQS}\\
&\quad + 6s_1^2\chi_{2,n,2}^{BQS} + 12q_1s_1\chi_{2,n+1,1}^{BQS} + 6q_1^2\chi_{2,n+2,0}^{BQS} + 4s_1\chi_{3,n,1}^{BQS} + 4q_1\chi_{3,n+1,0}^{BQS} + \chi_{4,n,0}^{BQS})/24,\\
\tilde{\chi}_n^{Q,6} &= (360s_3^2\chi_{0,n,2}^{BQS} + 720s_1s_5\chi_{0,n,2}^{BQS} + 120s_1^3s_3\chi_{0,n,4}^{BQS} + s_1^6\chi_{0,n,6}^{BQS} + 720q_5s_1\chi_{0,n+1,1}^{BQS}\\
&\quad + 720q_3s_3\chi_{0,n+1,1}^{BQS} + 720q_1s_5\chi_{0,n+1,1}^{BQS} + 120q_3s_1^3\chi_{0,n+1,3}^{BQS} + 360q_1s_1^2s_3\chi_{0,n+1,3}^{BQS}\\
&\quad + 6q_1s_1^5\chi_{0,n+1,5}^{BQS} + 360q_3^2\chi_{0,n+2,0}^{BQS} + 720q_1q_5\chi_{0,n+2,0}^{BQS} + 360q_1q_3s_1^2\chi_{0,n+2,2}^{BQS}\\
&\quad + 360q_1^2s_1s_3\chi_{0,n+2,2}^{BQS} + 15q_1^2s_1^4\chi_{0,n+2,4}^{BQS} + 360q_1^2q_3s_1\chi_{0,n+3,1}^{BQS} + 120q_1^3s_3\chi_{0,n+3,1}^{BQS}\\
&\quad + 20q_1^3s_1^3\chi_{0,n+3,3}^{BQS} + 120q_1^3q_3\chi_{0,n+4,0}^{BQS} + 15q_1^4s_1^2\chi_{0,n+4,2}^{BQS} + 6q_1^5s_1\chi_{0,n+5,1}^{BQS}\\
&\quad + q_1^6\chi_{0,n+6,0}^{BQS} + 720s_5\chi_{1,n,1}^{BQS} + 360s_1^2s_3\chi_{1,n,3}^{BQS} + 6s_1^5\chi_{1,n,5}^{BQS} + 720q_5\chi_{1,n+1,0}^{BQS}\\
&\quad + 360q_3s_1^2\chi_{1,n+1,2}^{BQS} + 720q_1s_1s_3\chi_{1,n+1,2}^{BQS} + 30q_1s_1^4\chi_{1,n+1,4}^{BQS} + 720q_1q_3s_1\chi_{1,n+2,1}^{BQS}\\
&\quad + 360q_1^2s_3\chi_{1,n+2,1}^{BQS} + 60q_1^2s_1^3\chi_{1,n+2,3}^{BQS} + 360q_1^2q_3\chi_{1,n+3,0}^{BQS} + 60q_1^3s_1^2\chi_{1,n+3,2}^{BQS}\\
&\quad + 30q_1^4s_1\chi_{1,n+4,1}^{BQS} + 6q_1^5\chi_{1,n+5,0}^{BQS} + 360s_1s_3\chi_{2,n,2}^{BQS} + 15s_1^4\chi_{2,n,4}^{BQS} + 360q_3s_1\chi_{2,n+1,1}^{BQS}\\
&\quad + 360q_1s_3\chi_{2,n+1,1}^{BQS} + 60q_1s_1^3\chi_{2,n+1,3}^{BQS} + 360q_1q_3\chi_{2,n+2,0}^{BQS} + 90q_1^2s_1^2\chi_{2,n+2,2}^{BQS}\\
&\quad + 60q_1^3s_1\chi_{2,n+3,1}^{BQS} + 15q_1^4\chi_{2,n+4,0}^{BQS} + 120s_3\chi_{3,n,1}^{BQS} + 20s_1^3\chi_{3,n,3}^{BQS} + 120q_3\chi_{3,n+1,0}^{BQS}\\
&\quad + 60q_1s_1^2\chi_{3,n+1,2}^{BQS} + 60q_1^2s_1\chi_{3,n+2,1}^{BQS} + 20q_1^3\chi_{3,n+3,0}^{BQS} + 15s_1^2\chi_{4,n,2}^{BQS}\\
&\quad + 30q_1s_1\chi_{4,n+1,1}^{BQS} + 15q_1^2\chi_{4,n+2,0}^{BQS} + 6s_1\chi_{5,n,1}^{BQS} + 6q_1\chi_{5,n+1,0}^{BQS} + \chi_{6,n,0}^{BQS})/720.
\end{aligned}
$$

Bibliography

[1] K. G. Wilson, *Confinement of quarks*, *Phys. Rev. D* **10** (1974) 2445.

[2] D. J. Gross and F. Wilczek, *Ultraviolet behavior of non-abelian gauge theories*, *Phys. Rev. Lett.* **30** (1973) 1343.

[3] PHENIX collaboration, *Suppression of hadrons with large transverse momentum in central $au + au$ collisions at $\sqrt{s_{\rm NN}} = 130{\rm GeV}$*, *Phys. Rev. Lett.* **88** (2001) 022301.

[4] STAR collaboration, *Disappearance of back-to-back high-p_T hadron correlations in central ${\rm Au} + {\rm Au}$ collisions at $\sqrt{s_{NN}} = 200\ {\rm GeV}$*, *Phys. Rev. Lett.* **90** (2003) 082302.

[5] U. W. Heinz and M. Jacob, *Evidence for a new state of matter: An Assessment of the results from the CERN lead beam program*, nucl-th/0002042.

[6] A. M. Polyakov, *Thermal Properties of Gauge Fields and Quark Liberation*, *Phys. Lett. B* **72** (1978) 477.

[7] HotQCD collaboration, *Universal Scaling Properties of QCD Close to the Chiral Limit*, *Acta Phys. Pol. B Proc. Suppl.* **14** (2021) 291 [2010.15593].

[8] HotQCD collaboration, *Chiral Phase Transition Temperature in (2+1)-Flavor QCD*, *Phys. Rev. Lett.* **123** (2019) 062002 [1903.04801].

[9] HotQCD collaboration, *Chiral crossover in QCD at zero and non-zero chemical potentials*, *Phys. Lett.* **B795** (2019) 15 [1812.08235].

[10] S. Borsanyi, Z. Fodor, J. N. Guenther, R. Kara, S. D. Katz, P. Parotto et al., *QCD Crossover at Finite Chemical Potential from Lattice Simulations*, *Phys. Rev. Lett.* **125** (2020) 052001 [2002.02821].

[11] G. Aarts, K. Boguslavski, M. Scherzer, E. Seiler, D. Sexty and I.-O. Stamatescu, *Getting even with CLE*, *EPJ Web Conf.* **175** (2018) 14007 [1710.05699].

[12] AURORASCIENCE collaboration, *New approach to the sign problem in quantum field theories: High density QCD on a Lefschetz thimble*, *Phys. Rev. D* **86** (2012) 074506 [1205.3996].

[13] G. Gagliardi and W. Unger, *New dual representation for staggered lattice QCD*, *Phys. Rev. D* **101** (2020) 034509 [1911.08389].

[14] P. de Forcrand and O. Philipsen, *The QCD phase diagram for small densities from imaginary chemical potential*, *Nucl. Phys. B* **642** (2002) 290 [hep-lat/0205016].

[15] R. V. Gavai and S. Gupta, *Pressure and nonlinear susceptibilities in QCD at finite chemical potentials*, *Phys. Rev. D* **68** (2003) 034506 [hep-lat/0303013].

[16] W. Busza, K. Rajagopal and W. van der Schee, *Heavy Ion Collisions: The Big Picture, and the Big Questions*, *Ann. Rev. Nucl. Part. Sci.* **68** (2018) 339 [1802.04801].

[17] M. A. Stephanov, *Non-gaussian fluctuations near the qcd critical point*, *Phys. Rev. Lett.* **102** (2009) 032301.

[18] M. A. Stephanov, *On the sign of kurtosis near the QCD critical point*, *Phys. Rev. Lett.* **107** (2011) 052301 [1104.1627].

[19] K. Symanzik, *Continuum Limit and Improved Action in Lattice Theories. 1. Principles and phi**4 Theory*, *Nucl. Phys. B* **226** (1983) 187.

[20] K. Symanzik, *Continuum Limit and Improved Action in Lattice Theories. 2. O(N) Nonlinear Sigma Model in Perturbation Theory*, *Nucl. Phys. B* **226** (1983) 205.

[21] C. Gattringer and C. B. Lang, *Quantum chromodynamics on the lattice*, vol. 788 of *Lecture notes in physics ; 788*. Springer, Berlin [u.a.], 2010.

[22] J. B. Kogut and L. Susskind, *Hamiltonian Formulation of Wilson's Lattice Gauge Theories*, *Phys. Rev. D* **11** (1975) 395.

[23] MILC collaboration, *Nonperturbative QCD Simulations with 2+1 Flavors of Improved Staggered Quarks*, *Rev. Mod. Phys.* **82** (2010) 1349 [0903.3598].

[24] HPQCD, UKQCD collaboration, *Highly improved staggered quarks on the lattice, with applications to charm physics*, *Phys. Rev. D* **75** (2007) 054502 [hep-lat/0610092].

[25] S. Naik, *On-shell Improved Lattice Action for QCD With Susskind Fermions and Asymptotic Freedom Scale*, *Nucl. Phys. B* **316** (1989) 238.

[26] A. D. Kennedy, I. Horvath and S. Sint, *A New exact method for dynamical fermion computations with nonlocal actions*, *Nucl. Phys. B Proc. Suppl.* **73** (1999) 834 [hep-lat/9809092].

[27] M. A. Clark, *The Rational Hybrid Monte Carlo Algorithm*, *PoS* **LAT2006** (2006) 004 [hep-lat/0610048].

[28] B. Jegerlehner, *Krylov space solvers for shifted linear systems*, hep-lat/9612014.

[29] K. Wu and H. Simon, *Thick-Restart Lanczos Method for Large Symmetric Eigenvalue Problems*, *SIAM J. Matrix Anal. Appl.* **22(2)** (2000) 602.

[30] R. Li, Y. Xi, E. Vecharynski, C. Yang and Y. Saad, *A Thick-Restart Lanczos Algorithm with Polynomial Filtering for Hermitian Eigenvalue Problems*, *SIAM J. Sci. Comput.* **38(4)** (2016) A2512.

[31] MILC collaboration, *Results for light pseudoscalar mesons*, *PoS* **LATTICE2010** (2010) 074 [1012.0868].

[32] FLAVOUR LATTICE AVERAGING GROUP collaboration, *FLAG Review 2019: Flavour Lattice Averaging Group (FLAG)*, *Eur. Phys. J. C* **80** (2020) 113 [1902.08191].

[33] D. Bollweg, J. Goswami, O. Kaczmarek, F. Karsch, S. Mukherjee, P. Petreczky et al., *Second order cumulants of conserved charge fluctuations revisited I. Vanishing chemical potentials*, 2107.10011.

[34] C. R. Allton, M. Doring, S. Ejiri, S. J. Hands, O. Kaczmarek, F. Karsch et al., *Thermodynamics of two flavor QCD to sixth order in quark chemical potential*, *Phys. Rev. D* **71** (2005) 054508 [hep-lat/0501030].

[35] A. Bazavov et al., *QCD equation of state to $\mathcal{O}(\mu_B^6)$ from lattice QCD*, *Phys. Rev. D* **95** (2017) 054504.

[36] P. Hasenfratz and F. Karsch, *Chemical Potential on the Lattice*, *Phys. Lett.* **125B** (1983) 308.

[37] R. V. Gavai and S. Sharma, *A faster method of computation of lattice quark number susceptibilities*, *Phys. Rev. D* **85** (2012) 054508 [1112.5428].

[38] R. V. Gavai and S. Sharma, *Divergences in the quark number susceptibility: The origin and a cure*, *Phys. Lett. B* **749** (2015) 8 [1406.0474].

[39] R. Hagedorn, *Statistical thermodynamics of strong interactions at high-energies*, *Nuovo Cim. Suppl.* **3** (1965) 147.

[40] K. Redlich and H. Satz, *The Legacy of Rolf Hagedorn: Statistical Bootstrap and Ultimate Temperature*, pp. 49–68. Springer International Publishing, Cham, 2016. 10.1007/978-3-319-17545-4_7.

[41] P. D. Group, *Review of Particle Physics*, *Progress of Theoretical and Experimental Physics* **2020** (2020) .

[42] R. Dashen, S.-k. Ma and H. J. Bernstein, *s-matrix formulation of statistical mechanics*, *Phys. Rev.* **187** (1969) 345.

[43] A. Andronic, P. Braun-Munzinger, K. Redlich and J. Stachel, *Decoding the phase structure of qcd via particle production at high energy*, *Nature* **561** (2018) 321.

[44] STAR collaboration, *Bulk Properties of the Medium Produced in Relativistic Heavy-Ion Collisions from the Beam Energy Scan Program*, *Phys. Rev. C* **96** (2017) 044904 [1701.07065].

[45] R. Bellwied, S. Borsányi, Z. Fodor, J. N. Guenther, J. Noronha-Hostler, P. Parotto et al., *Off-diagonal correlators of conserved charges from lattice qcd and how to relate them to experiment*, *Phys. Rev. D* **101** (2020) 034506.

[46] A. Bazavov et al., *Additional Strange Hadrons from QCD Thermodynamics and Strangeness Freezeout in Heavy Ion Collisions*, *Phys. Rev. Lett.* **113** (2014) 072001 [1404.6511].

[47] B. Friman, P. M. Lo, M. Marczenko, K. Redlich and C. Sasaki, *Strangeness fluctuations from $k-\pi$ interactions*, *Phys. Rev. D* **92** (2015) 074003.

[48] D. Bollweg, J. Goswami, O. Kaczmarek, F. Karsch, S. Mukherjee, P. Petreczky et al., *Dataset for Second order cumulants of conserved charge fluctuations revisited I. Vanishing chemical potentials*, https://doi.org/10.4119/unibi/2957724.

[49] F. Karsch, K. Morita and K. Redlich, *Effects of kinematic cuts on net-electric charge fluctuations*, *Phys. Rev. C* **93** (2016) 034907 [1508.02614].

[50] J. Engels, F. Karsch and H. Satz, *Finite size effects in euclidean lattice thermodynamics for non-interacting bose and fermi systems*, *Nuclear Physics B* **205** (1982) 239.

[51] M. Gorenstein, V. Petrov and G. Zinovjev, *Phase transition in the hadron gas model*, *Physics Letters B* **106** (1981) 327.

[52] V. Vovchenko, M. I. Gorenstein and H. Stoecker, *van der Waals Interactions in Hadron Resonance Gas: From Nuclear Matter to Lattice QCD*, *Phys. Rev. Lett.* **118** (2017) 182301 [1609.03975].

[53] K. Taradiy, A. Motornenko, V. Vovchenko, M. I. Gorenstein and H. Stoecker, *The analytic structure of thermodynamic systems with repulsive interactions*, *Phys. Rev. C* **100** (2019) 065202 [1904.08259].

[54] P. M. Lo, B. Friman, M. Marczenko, K. Redlich and C. Sasaki, *Repulsive interactions and their effects on the thermodynamics of a hadron gas*, *Phys. Rev. C* **96** (2017) 015207 [1703.00306].

[55] C. Fernández-Ramírez, P. M. Lo and P. Petreczky, *Thermodynamics of the strange baryon system from a coupled-channels analysis and missing states*, *Phys. Rev. C* **98** (2018) 044910 [1806.02177].

[56] S. Capstick and W. Roberts, *Quasi two-body decays of nonstrange baryons*, *Phys. Rev. D* **49** (1994) 4570 [nucl-th/9310030].

[57] B. C. Hunt and D. M. Manley, *Updated determination of N^* resonance parameters using a unitary, multichannel formalism*, *Phys. Rev. C* **99** (2019) 055205 [1810.13086].

[58] HotQCD collaboration, *Skewness, kurtosis, and the fifth and sixth order cumulants of net baryon-number distributions from lattice QCD confront high-statistics STAR data*, *Phys. Rev. D* **101** (2020) 074502.

[59] M. H. Quenouille, *Notes on bias in estimation*, *Biometrika* **43** (1956) 353.

[60] HotQCD collaboration, *Skewness and kurtosis of net baryon-number distributions at small values of the baryon chemical potential*, *Phys. Rev.* **D96** (2017) 074510 [1708.04897].

[61] STAR collaboration, *Cumulants and correlation functions of net-proton, proton, and antiproton multiplicity distributions in Au+Au collisions at energies available at the BNL Relativistic Heavy Ion Collider*, *Phys. Rev. C* **104** (2021) 024902 [2101.12413].

[62] M. Kitazawa and M. Asakawa, *Revealing baryon number fluctuations from proton number fluctuations in relativistic heavy ion collisions*, *Phys. Rev. C* **85** (2012) 021901 [1107.2755].

[63] V. Vovchenko, *Correcting event-by-event fluctuations in heavy-ion collisions for exact global conservation laws with the generalized subensemble acceptance method*, 2106.13775.

[64] V. Vovchenko, O. Savchuk, R. V. Poberezhnyuk, M. I. Gorenstein and V. Koch, *Connecting fluctuation measurements in heavy-ion collisions with the grand-canonical susceptibilities*, *Phys. Lett. B* **811** (2020) 135868 [2003.13905].

[65] A. Bzdak, S. Esumi, V. Koch, J. Liao, M. Stephanov and N. Xu, *Mapping the Phases of Quantum Chromodynamics with Beam Energy Scan*, *Phys. Rept.* **853** (2020) 1 [1906.00936].

[66] STAR collaboration, *Measurement of the sixth-order cumulant of net-proton multiplicity distributions in Au+Au collisions at* $\sqrt{s_{\rm NN}} = 27$, *54.4, and 200 GeV at RHIC*, 2105.14698.

[67] STAR collaboration, *Beam energy dependence of moments of the net-charge multiplicity distributions in* $\mathrm{Au} + \mathrm{Au}$ *collisions at RHIC*, *Phys. Rev. Lett.* **113** (2014) 092301.

[68] F. Karsch, *Determination of Freeze-out Conditions from Lattice QCD Calculations*, *Central Eur. J. Phys.* **10** (2012) 1234 [1202.4173].

[69] S. Borsanyi, Z. Fodor, S. D. Katz, S. Krieg, C. Ratti and K. K. Szabo, *Freeze-out parameters from electric charge and baryon number fluctuations: is there consistency?*, *Phys. Rev. Lett.* **113** (2014) 052301 [1403.4576].

[70] PHENIX collaboration, *Measurement of higher cumulants of net-charge multiplicity distributions in* $\mathrm{Au} + \mathrm{Au}$ *collisions at* $\sqrt{s_{NN}} = 7.7 - -200$ GeV, *Phys. Rev. C* **93** (2016) 011901.

[71] L. Adamczyk et al., *Collision energy dependence of moments of net-kaon multiplicity distributions at rhic*, *Physics Letters B* **785** (2018) 551.

[72] STAR collaboration, *Beam energy dependence of net- Λ fluctuations measured by the STAR experiment at the BNL Relativistic Heavy Ion Collider*, *Phys. Rev. C* **102** (2020) 024903 [2001.06419].

[73] STAR collaboration, *Strange and multistrange particle production in Au + Au collisions at $\sqrt{s_{NN}} = 62.4$ GeV*, *Phys. Rev. C* **83** (2011) 024901.

[74] STAR collaboration, *Strange hadron production in Au+Au collisions at $\sqrt{s_{\rm NN}}$ = 7.7, 11.5, 19.6, 27, and 39 GeV*, *Phys. Rev. C* **102** (2020) 034909.

[75] P. Braun-Munzinger et al., *Confronting fluctuations of conserved charges in central nuclear collisions at the LHC with predictions from Lattice QCD*, *Physics Letters B* **747** (2015) 292 .

[76] G. Hooft, *Naturalness, Chiral Symmetry, and Spontaneous Chiral Symmetry Breaking*, pp. 135–157. Springer US, Boston, MA, 1980. 10.1007/978-1-4684-7571-5_9.

[77] A. Casher, *Chiral symmetry breaking in quark confining theories*, *Physics Letters B* **83** (1979) 395.

[78] J. Kogut, M. Stone, H. W. Wyld, J. Shigemitsu, S. H. Shenker and D. K. Sinclair, *Scales of chiral symmetry breaking in quantum chromodynamics*, *Phys. Rev. Lett.* **48** (1982) 1140.

[79] A. Bazavov et al., *Meson screening masses in (2+1)-flavor QCD*, *Phys. Rev. D* **100** (2019) 094510 [1908.09552].

[80] P. M. Lo, B. Friman, K. Redlich and C. Sasaki, *S-matrix analysis of the baryon electric charge correlation*, *Phys. Lett. B* **778** (2018) 454 [1710.02711].

List of Figures

List of Tables

Acknowledgments

First of all, I would like to thank Frithjof Karsch for his guidance and support throughout the last three years. He was always open to questions and always helped me when I found myself heading towards a dead end in my work. He granted me a great amount of freedom to pursue my research interests and enabled me to work on exciting computing projects which kindled my passion for high performance computing. For this, I am incredibly grateful.

Furthermore, I would like to thank Swagato Mukherjee for his support throughout these years and his kind hospitality during my stays at Brookhaven National Laboratory. His unique approach towards science inspired me a lot and I am very grateful for the guidance and advice he provided.

I want to thank Christian Schmidt for agreeing to be the second referee for this work and for his help explaining the various scientific codes and analysis methods to me. Anirban Lahiri deserves special thanks for all the extensive and entertaining discussions about physics and his great explanations to all my questions about QCD and heavy ion collisions. I greatly appreciate the help I received from Jishnu Goswami with various data analyses and hadron resonance gas models.

Furthermore, I want to thank Lukas Mazur, Hauke Sandmeyer, Philipp Scior, Hai-Tao Shu, David Clarke, Luis Altenkort and Rasmus Larsen for all their work on our GPU code, all the discussions about programming and for making the countless hours of developing, debugging and profiling so enjoyable.

Lastly, I wish to thank my friends and colleagues from Bielefelds high energy physics group, specifically, Simon Dentinger, Lorenzo Dini, Giuseppe Gagliardi, Guido Nicotra, Marc Borell, Marius Neumann and Hendrick Roch for the great times we had working and traveling together.

Disclaimer

I hereby declare that the work done in this thesis is that of the author alone with the help of no more than the mentioned literature and auxiliary means.

Bielefeld, October 13, 2021

_____

Dennis Bollweg

Gedruckt auf alterungsbeständigem Papier gemäß DIN ISO 9706.